Dipl.-Ing. Peter Opriessnig

Cardiovascular magnetic resonance imaging of the vessel wall

DOCTORAL THESIS

to achieve the university degree of

Doktor der technischen Wissenschaften

submitted to

Graz University of Technology

Supervisor

Univ.-Prof. Dipl.-Ing. Dr.techn. Rudolf Stollberger

Institute of Medical Engineering

Evaluator

Assoz.-Prof. Univ.-Doz. Dipl.-Ing. Dr. Stefan Ropele

Division of General Neurology
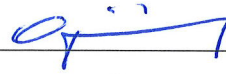
Medical University of Graz

Graz, October 2017

Affidavit

I declare that I have authored this thesis independently, that I have not used other than the declared sources/resources, and that I have explicitly indicated all material which has been quoted either literally or by content from the sources used. The text document uploaded to TUGRAZonline is identical to the present doctoral thesis.

08.11.2017
_____
Date

_____
Signature

Eidesstattliche Erklärung

Ich erkläre an Eides statt, dass ich die vorliegende Arbeit selbstständig verfasst, andere als die angegebenen Quellen/Hilfsmittel nicht benutzt, und die den benutzten Quellen wörtlich und inhaltlich entnommenen Stellen als solche kenntlich gemacht habe. Das in TUGRAZonline hochgeladene Textdokument ist mit der vorliegenden Dissertation identisch.

08.11.2017
_____
Datum

_____
Unterschrift

Acknowledgements

First of all, I would like to thank my partner Vera and daughter Paula. I am really proud to have such a great toddler. I am thankful for my sweetheart, for her patience and support especially throughout the last decade. I also want to thank my family, especially thanks to my mum for her support.

Special thanks to my supervisor Prof. Rudolf Stollberger for his support, patience and discussions. A couple of lucky events and his support in the past made it possible to get in touch with this exciting and challenging field. Many thanks for that.

Furthermore, I would like to thank all colleagues and people I met and cooperated for all these years. Thanks to people from my alma mater the Institute of Medical Engineering (TUG). Thanks to people from the Institute of Medical and Chemical Laboratory Diagnostics, Institute of Physiological Chemistry, Institute of Biophysics and Institute of Molecular Biology and Biochemistry (MUG).

Special thanks to Dr. Gernot Reishofer (Division of Neuroradiology, Vascular and Interventional Radiology, MUG), Gerd Hoerl (Institute of Physiological Chemistry, MUG), Gunter Almer (Institute of Medical and Chemical Laboratory Diagnostics, MUG) and the EU project NanoAthero for the fruitful last years.

In memoriam of my father

Abstract

Atherosclerosis (AS) is a chronic immune-mediated inflammatory state and multifactorial disease of large and medium sized arteries leading to cardiovascular diseases such as stroke and myocardial infarction. Atherogenesis is studied by the use of animal models (mouse, rabbit, swine) and the most popular strategy to induce lesion development in a rabbit model of atherosclerosis (New Zealand White rabbit) is the combination of a dietary trigger and balloon catheter denudation (mechanical intervention). Because the aorta is narrowing from proximal to distal a constant balloon volume introduces significant pressure variations when retracted. Consequently, a not well-defined, heterogeneous plaque development can be expected, which represents a major drawback of this technique. Moreover, catheter induced injury may also vary between operator's as the handling of syringe and balloon filling requires training and adjusting a prescribed pressure to vessel diameter variations seems to be challenging. To compensate for that operator driven errors a new technique (patent application number GB 1614500.5) is proposed for the generation of more well-defined and reproducible aortic atherosclerotic plaques by a pressure controlled mechanical balloon injury device. Balloon inflation pressure recordings support the superiority of the proposed method compared to the conventional technique. Multicontrast magnetic resonance imaging (MRI) has become a well-recognized tool to study the complexity of an atherosclerotic plaque in order to predict lesion vulnerability. Diffusion tensor imaging (DTI) could be an additional measure that provides information on the microstructural changes of the vessel wall due to tissue remodeling and plaque burden, which may help to understand the formation of a complex disease. In this work, the feasibility to investigate the orientation of diffusion anisotropy in healthy human carotids in vivo is demonstrated. Tangential and radial diffusion were measured by the combination of a read-out segmented EPI (rs-EPI) with a 2D special gradient direction scheme. A significant linear relationship between age and fractional anisotropy (FA) was found which may indicate a possible alteration of tissue's microstructural integrity. Moreover, this finding point FA being a sensitive metric able to uncover changes in the wall architecture with age. Beside the use of multispectral protocols or all-in-one solutions to identify plaque morphology and composition a complementary method to study lesion progression is molecular imaging. A technique presented in this work allows the simultaneous measurement of endothelial barrier function (interendothelial junction integrity) and nitric oxide induced endothelium-independent (smooth-muscle cell dependent) vasomotor response of the abdominal aorta in rabbits.

The infusion of the nanoparticle caused a prominent relaxation of the vessel wall and a decrease in vascular endothelial permeability of the control animal. The AS induced rabbit with comparable wall appearance (similar normalized wall index) showed an impaired vasodilation as well as loss of the interendothelial junction integrity (endothelial damage). The rabbit with a marked wall thickening showed a paradoxical vasoconstriction and a reconstituted delayed endothelial function. These data assume specific patterns depending on the degree of plaque burden. The use of dynamic nanoparticle enhanced plaque MR imaging for assessing vasomotion and permeability seems to be a potential strategy for risk stratification of the vascular fitness.

Kurzfassung

Atherosklerose ist eine chronische immunvermittelte und multifaktorielle Erkrankung der mittleren und großen Blutgefäße welche zu kardiovaskulären Ereignissen wie Schlaganfall und Herzinfarkt führen kann. Grundsätzlich wird die Atherogenese in Tiermodellen studiert. Am häufigsten werden dazu Kaninchen eingesetzt die bei entsprechender Diät und zusätzlicher mechanischer Intervention (Ballon Katheter Denudation) Gefäßwandläsionen sog. Plaques ausbilden. Traditionell wird diese mechanische Schädigung manuell durchgeführt. Da die Aorta von proximal nach distal im Durchmesser abnimmt ergeben sich bei konstanter bzw. unzureichender Anpassung der Ballonfüllung (Operator abhängig) Druckschwankungen die das Gefäß unterschiedlich stark schädigen. In dieser Arbeit wird eine neue Technik (Patent-Prioritätsanmeldung) vorgestellt die die Schwächen des manuellen Operator abhängigen Manövers kompensiert indem eine maschinelle druckgeregelte Füllung des Ballons vorgenommen wird. Der Regelkreis erlaubt einen konstanten Ballondruck durch füllen/entleeren des Ballons abhängig vom Querschnitt des Gefäßes. Die erhobenen Druckdaten deuten auf einen eindeutigen Vorteil dieser Technik gegenüber der konventionellen Methode hin. Zur Messung von atherosklerotischen Gefäßwandveränderungen sowie zur Abzuschätzung deren Schweregrades werden sogenannte Multikontrast-Magnetresonanztomographie (MRT) Protokolle eingesetzt. Die Diffusions-Tensor-Bildgebung ist eine ergänzende Methode die mögliche Änderungen in der Wasserdiffusion auf Grund von pathologischen Wandveränderungen aufspüren und einen tieferen Einblick in die Formierung dieser Erkrankung liefern kann. In dieser Arbeit wird eine Methode präsentiert die es erlaubt die anisotrope Wasserdiffusion in der Gefäßwand zu messen. Mit einer speziellen MRT-Sequenz sowie einem speziellen zwei-dimensionalen Gradientenschema ist es möglich sowohl radiale als auch tangentiale Wanddiffusionskomponenten zu bestimmen. Es konnte ein signifikanter linearer Zusammenhang zwischen fraktioneller Anisotropie (FA) und Probandenalter gefunden werden. Dieses Ergebnis lässt auf eine Modifizierung der Wandgewebeintegrität schließen und weist den FA Wert als sensitiven Marker aus der Änderungen in der Wandarchitektur aufspüren kann. Eine Erweiterung zum Multikontrast-Ansatz ist die sog. molekulare Bildgebung die es ermöglicht Gefäßläsionen bzw. pathologische Prozesse auf zellulärer Ebene sichtbar zu machen. In dieser Arbeit wird eine Nanopartikel basierte Methode vorgestellt die es erlaubt gleichzeitig vaskuläre Permeabilität der Gefäßwand und Stickoxid vermittelte Endothelium unabhängige Vasomotorfunktion (Gefäßrelaxation oder Konstriktion) im Tiermodell zu untersuchen. Die Infusion des

Nanopartikels führte beim gesunden Kontrolltier zu einer ausgeprägten Relaxation der Gefäßwand sowie zu einer reduzierten Permeabilität. Das Versuchstier mit induzierter Läsion und ähnlicher Wandstärke (früher Plaque) zeigte eine beeinträchtigte Relaxation sowie erhöhte Permeabilität. Jenes Versuchstier mit ausgeprägter Plaquebildung wies eine paradoxe Gefäßkonstriktion und Wiederherstellung der reduzierten Permeabilität auf. Die Ergebnisse zeigen spezifische Muster je nach Schweregrad der Gefäßwandveränderung. Diese eindeutigen Muster stellen einen potentiellen Marker dar um eine mögliche Risikoabschätzung der kardiovaskulären Fitness zu erlauben.

List of Abbreviations and Symbols

Acronyms

(i)MSDE	(improved) motion-sensitized driven-equilibrium
2D	Two-dimensional
3D	Three-dimensional
AHA	American Heart Association
ApoE	Apolipoprotein-E
AS	Atherosclerosis
BPA	Blood pool agent
CA	Calcification or Contrast Agent
CE	Contrast enhancement
CE-MRI	Contrast enhanced magnetic resonance imaging
CNR	Contrast to noise ratio
CVDs	Cardiovascular diseases
DANTE	Delay alternating with nutation for tailored excitation
DIR	Double inversion recovery
DP-TSE	Diffusion prepared TSE
DTI	Diffusion tensor imaging
DWI	Diffusion weighted imaging
EPI	Echo Planar Imaging
FC	Fibrous cap
FDA	Food and Drug Administration
FLASH	Fast low-angle shot
FOV	Field of view
FRE	Flow-related enhancement
FSD	Flow-sensitive dephasing

FSE	Fast spin echo
Gd	Gadolinium
Gd-PS	Phosphatidylserine enriched paramagnetic gadolinium liposomes
GRAPPA	GeneRalized Autocalibrating Partial Parallel Acquisition
GRE	Gradient-recalled echo
IPH	Intra plaque hemorrhage
LRNC	Lipid rich necrotic core
MATCH	Multicontrast atherosclerosis characterization
meGRE	Multiecho gradient echo
MERGE	MSDE rapid black-blood gradient echo sequence
MIP	Maximum intensity projection
MOTSA	Multiple overlapping thin-slab acquisition
MP-RAGE	Magnetization-prepared rapid acquisition gradient echo
MR-DWI	Magnetic resonance diffusion weighted imaging
MR-HIFU	MRI guided high intensity focused ultrasound
MRI	Magnetic resonance imaging
MT	Magnetization transfer
MTR	Magnetization transfer ratio
NZW	New Zealand White rabbit
PDw	Proton-density-weighted
QIR	Quadruple inversion recovery
RES	Reticuloendothelial system
RESOLVE	Read-out segmentation with navigator-echo correction
RF	Radiofrequency
rFOV	Reduced field of view
rs-EPI	Read-out segmented EPI
SE	Spin echo
SLIP	Spatially separated lipid presaturation
SNAP	Simultaneous noncontrast angiography and intraplaque hemorrhage

SNR	Signal to noise ratio
SPACE	Variable-flip-angle turbo spin-echo
SPI	Phase-sensitive inversion-recovery
SPIO	Superparamagnetic iron oxides
ss-IMIV-DWEPI	Single-Shot Interleaved Multislice Inner Volume Diffusion-Weighted Echo Planar Imaging
SWI	Susceptibility-weighted imaging
T1w	T1-weighted
T2w	T2-weighted
TCFA	Thin cap fibroatheroma
TOF	Time of flight
TONE	Tilted optimized nonsaturating excitation
TSE	Turbo spin echo
USPIO	Ultrasmall superparamagnetic iron oxides
WHHL	Watanabe-heritable hyperlipidemic rabbit
WHO	World health organization

Symbols in general

α	Flip angle (rad or degree)
ABIP	Actual balloon inflation pressure (bar)
AD	Axial diffusivity (mm^2/s)
ADC	Apparent diffusion coefficient (mm^2/s)
CL	Linear anisotropy coefficient (mm^2/s)
CP	Planar anisotropy coefficient (mm^2/s)
CS	Spherical anisotropy coefficient (mm^2/s)
CV	Control variable
FA	Fractional anisotropy
M_0, S_0	Equilibrium magnetization

M_x, M_y, M_z	Magnetization components
MD	Mean diffusivity (mm^2/s)
NEX	Number of excitation
NWI	Normalized wall index
PE	Plaque enhancement
RD	Radial diffusivity (mm^2/s)
RR	R-wave to R-wave interval (ms)
SI, S	Signal
T_1, T_2, T_2^*	Relaxation times (ms)
T_E	Echo time (ms)
T_I	Inversion time (ms)
T_R	Repetition time (ms)
TA	Acquisition time (ms)
THK	Slice thickness (mm)
U(L)BIPL	Upper(lower) balloon inflation pressure limit (bar)

Symbols of Chapter 3

Δf	RF bandwidth (Hz)
Δz	Slice thickness (mm or cm)
$\Delta z_{exc.slice}$	Excitation slice (mm or cm)
$\Delta z_{pres.slab}$	Presaturation slab (mm or cm)
$\delta_{ppm_{fat}} f_0$	Chemical-shift (Hz)
gap_{max}	Maximum gap (mm or cm)
$M_{z_{ss}}$	Steady-state Mz
$T_{E_{eff}}$	Effective echo time (ms)
t_{esp}	Echo spacing (ms)

Symbols of Chapter 4

Δ	Gradient separation time (ms)
δ	Duration of the gradient pulses (ms)
γ	Gyromagnetic ratio (MHz/T)
b	b-value (s/mm^2)
G	Gradient strength (mT/m)

Symbols of Chapter 5

$\dfrac{1}{T_{1,2}^0}$	Native relaxation rate (s^{-1})
$\dfrac{1}{T_{1,2}^{CA}} = r_{1,2}[CA]$	Relaxivity concentration product (s^{-1})
$\dfrac{1}{T_{1,2}^n}$	New relaxation rate (s^{-1})
$r_{1,2}$	Relaxivity $(mM^{-1}s^{-1})$
[CA]	Contrast agent concentration (mM)

List of Tables

List of Figures

xv

Contents

1 Atherosclerosis

Cardiovascular diseases (CVDs) are the number one killer globally. Estimations from the world health organization (WHO) revealed that about one third of annually deaths were attributed to this life threatening disease in 2012 [1]. Of these events, three quarters are associated with stroke and coronary heart disease. The most severe pathological condition is atherosclerosis (AS), a chronic immune-mediated inflammatory state and multifactorial disease of large and medium sized arteries. It manifests in the first decades of life, with silent progression until a clinical event takes place [2]. Factors involved in lesion initiation and progression are dysfunction of endothelium, smooth muscle cell (SMC) proliferation, thrombogenicity, inflammation, macrophage infiltration, extracellular matrix (ECM) digestion, calcification, cell apoptosis and thrombosis. As an early event, endothelial dysfunction as a consequence of cardiovascular risk factors (smoking, hypercholesterolemia, Type I diabetes) is involved in remodeling processes of the arterial wall and progression of AS [3, 4, 5, 6]. As outlined in *Chapter 5.2*, a functional vascular endothelium supports the beneficial effects of antioxidant, antiinflammatory, anticoagulant and profibrinolytic actions and nitric oxide (NO) release [7]. NO inhibits the adhesion and migration of leukocytes, the migration and proliferation of SMCs, the aggregation and adhesion of platelets, promotes re-endothelialization and is essential for maintaining vascular tone. Moreover, NO controls vasoreactivity, regulates endothelial cell and tight junction morphology and vascular permeability [8, 9]. Endothelial NO synthase (eNOS) synthesizes NO in the endothelium and is a protective factor maintaining vascular integrity [10]. A reduction of NO activity therefore leads to endothelial dysfunction and precedes the development of AS. Therefore, pathological activated endothelium characterized by upregulated proinflammatory endothelial surface markers (Vascular Cell Adhesion Molecule 1 (VCAM-1), E-selectin and P-selectin etc.) initiates recruitment of leukocytes (monocytes, T-lymphocytes) into the wall [11, 12]. Activation of vascular endothelium in turn is promoted by proinflammatory cytokines, lipopolysaccharides and accumulation of minimal oxidized low density lipoprotein (LDL) [2]. In addition, oxidized LDL is able to inhibit the synthesis of NO. Cytocines are inflammatory mediators and can be subdivided into atheroprotective and proinflammatory ones [13]. Antiinflammatory cytokines (e.g. major antiinflammatory cytokine: interleukin-10, IL-10) within the lesion balance the inflammatory response and prevent from cell death whereas proinflammatory components cause ECM degradation, cell proliferation / death and promote lesion formation and progression. IL-10 expression within macrophages

was detected in advanced human plaques and was found to be more frequently expressed in human unstable vs stable lesions [14, 15]. Another atheroprotective factor is high density lipoprotein (HDL) which removes excess cholesterol from peripheral tissues and acts as an antioxidant. However, beside the migration of monocyte-derived macrophages, LDL accumulates in the arterial wall (intima) undergoes modification to oxidized LDL (oxLDL) and is finally taken up by macrophages which generate the so called foam cells (lipid filled macrophages). This lesion type is called **intimal xanthoma** (fatty streak or initial lesion) and is the first detectable macroscopic wall modification [16, 17]. A second type of a preatherosclerotic lesion is **intimal thickening** originated from an existing intimal mass which lacks macrophage-derived foam cells but consists mainly of SMCs. However, persistent migration of inflammatory cells (monocytes, T-lymphocytes, SMCs, myofibroblasts) causes the development of the **pathological intimal thickening** also referred to as intermediate lesion. Lesion progression is further triggered by migration and proliferation of SMCs and production of derived ECM which are stimulated by macrophage and T cell secretion of cytokines and growth factors [2]. These events lead to the formation of a fibrous cap that overlies the atherosclerotic plaque. Whereas the intermediate type (preatheroma) consists of a fibrous cap made up of SMCs and proteoglycans overlying the lipid rich area (no necrosis or cellular debris) the **fibrous cap atheroma** classified as advanced lesion consists of a necrotic core (cholesterol ester, free cholesterol, phospholipids, triglycerides, extracellular lipids, calcification) and a thin/thick cap with additional varying amounts of macrophages and lymphocytes [16, 18]. A necrotic core is the result of necrosis, apoptosis, proteolysis, lipid accumulation and hypoxia of the transformed wall [19, 17]. Hypoxia as a consequence of hindered diffusion of oxygen from the lumen due to intimal thickening is bypassed by the vasa vasorum a network of vessels in the outer adventitial layer of arterial vessels and vasa vasorum neovascularization [20]. Moreover, neoangiogenesis arising from vasa vasorum has a major impact on lesion progression (early remodeling process) and destabilization as permeable microvessels leak lipoproteins into the intima [21, 22, 20, 23]. Kumamoto and colleagues found that intimal neovessels from vasa vasorum highly correlated with the degree of luminal stenosis, inflammation, lipid core size whereas neovessels originated from the lumen side were frequently found in plaques with 40-50% stenosis and were associated with fresh/old intraplaque hemorrhage [24, 20]. Moreover, intimal neovessel density was decreased in calcified lesions. However, they found the frequency of neovessels from vasa vasorum were 28 times that of the luminal origin. In addition, apoptosis of vascular SMCs seem to be the major factor involved in the formation of vascular

calcification [18]. Beside luminal encroaching, lesion formation is also accompanied by outward remodeling (increase of vessel diameter) a process that more or less preserves the luminal geometry [25, 17, 26]. Therefore, risk stratification of atherosclerotic lesions by traditional angiographic techniques alone may mask the true impact on future cardiovascular events. The complexity of an atherosclerotic plaque, rather than the degree of luminal narrowing, is thought to be a valuable predictor of lesion vulnerability and magnetic resonance imaging (MRI) because of its inherent soft tissue contrast most suitable to delineate key factors of plaque vulnerability [27]. Saam et al analyzed the prevalence of American Heart Association (AHA) lesion type VI (complex plaque with possible surface defect, hemorrhage, thrombus) in carotid arteries by multicontrast MRI and found this type frequently in arteries with a low degree of stenosis ($< 50\%$). Hemorrhage was detected in more than 80% of the type VI lesions and fibrous cap rupture in about half of them. Intraplaque hemorrhage is another important plaque feature in atherosclerosis progression and destabilization. High risk *'vulnerable'* plaques show thin fibrous cap (thin fibrous cap atheroma) and increased inflammation [2]. In addition, this type of lesion also shows loss of SMCs and ECM in the cap and contains a large lipid rich necrotic core, hemorrhage, intraplaque vasa vasorum and/or calcification [16]. Rupture frequently occurs at lesion edges which consists mainly of foam cells and manifests in thrombi formation and a possible clinical event [2]. In detail, upon cap rupture thrombogenic components of the lesion get in contact with blood and finally form a thrombus that may occlude the artery and results in myocardial infarction or stroke [17]. Moreover, an alternative fate is plaque rupture plus mural thrombus generation (nonocclusive) followed by re-endothelialization and accelerated lesion growth [17]. In contrast to rupture prone lesions, a *stable* plaque consists of a thick fibrous cap and a small fatty core. In addition, fibrocalcific lesions are also made up of a thick fibrous cap overlying a small fatty necrotic core plus high amounts of intimal calcium accumulations (possible final stage of the alternative fate lesion) [20]. Figure 1 is a graphical representation of the different stages of plaque development and was reprinted from Leiner et al with permission of Springer [17].

3
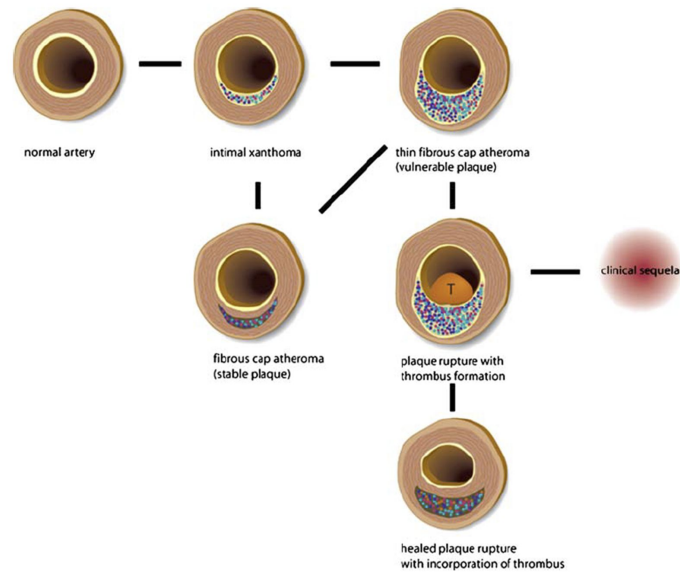
Figure 1: Different stages of plaque development (description see text). *Black lines* denote transitions between different stages. T, thrombus. Reprinted from Leiner et al with permission of Springer [17].

In the following, *Chapter 2* outlines animal models of atherosclerosis as well as strategies how to induce lesion generation. In addition, a new technique (patent application number GB 1614500.5) is proposed for the generation of more well-defined and reproducible aortic atherosclerotic plaques by a pressure controlled mechanical balloon injury device. In *Chapter 3* dark blood imaging (magnetization preparation) techniques are presented for effective nulling of flowing blood spins to reduce/diminish plaque-mimicking artifacts and improve image quality and delineation of wall architecture. Moreover, sequences and further developments for dedicated imaging of aortic atherosclerosis are outlined. *Chapter 4* includes a paper that demonstrates the feasibility to investigate the orientation of diffusion anisotropy in healthy human carotids in vivo by the combination of a read-out segmented EPI (rs-EPI) with a 2D special gradient direction scheme. In addition, consequences of a hyperhomocysteinemia (HHcy) and hypercholesterolemia (HCL) diet on aortic lesion development in a rabbit model of atherosclerosis are investigated. *Chapter 5* describes molecular imaging / nanoparticle enhanced plaque MR imaging strategies of atherosclerotic lesions in animals and men. In addition a technique is presented that allows the simultaneous measurement of endothelial barrier function and nitric oxide induced endothelium-independent (smooth-muscle cell dependent) vasomotor response of the abdominal aorta in rabbits. Finally aortic plaque imaging is demonstrated by (super)paramagnetic blood pool agents.

2 Atherosclerotic plaque generation by mechanical intervention

2.1 Introduction

Atherogenesis is studied by the use of animal models (swine, rabbit, mouse) and the development of an atherosclerotic lesion is induced by dietary (cholesterol diet & normal chow), mechanical (balloon denudation, angioplasty), pharmacological intervention (Russell's viper venom and histamine to induce thrombosis), can be spontaneously or is triggered by genetically modified organisms (ApoE-/- mouse) [28, 29]. Research activities are diverse but include for example progression-regression studies, response to treatment analysis, biomechanical investigations all aimed to uncover mechanisms responsible for remodeling processes of the arterial wall [30, 31, 32]. An example of a model organism generating lesions spontaneously is the male Japanese white rabbit which was found by Dr. Watanabe in the seventies [33]. This mutant showed hyperlipidemia despite feeding a normal chow diet due to a reduced low density lipoprotein (LDL) receptor function (impaired LDL catabolism). A strain named Watanabe-heritable hyperlipidemic (WHHL) rabbit was generated by inbreeding the found mutant [34, 35]. Characteristics of the strain are high serum cholesterol and triglyceride levels and derived age-related severe aortic atherosclerosis. A transgenic model of atherosclerosis is the apolipoprotein-E (ApoE) deficient mouse that develops severe hypercholesterolemia and atherosclerotic lesions of all progression stages throughout the arterial tree [36, 37, 38]. Spontaneous atherosclerosis is induced by elevated plasma levels of very low density lipoproteines and challenging with a Western-type diet lead to even higher levels and causes generation of atherosclerotic lesions in a shorter period. Another popular model to study atherosclerosis is the New Zealand White (NZW) rabbit. The type of stimulus or their combinatorial regimen causes formation of fatty streaks (short-term high-fat diet), generation of more advanced plaques (alternating high-fat and normal chow diet) which are formed in a shorter period of time when mechanical injury (balloon denudation, angioplasty) is added as a treatment or atherothrombosis when chemical triggering (Russell's viper venom) is used [39, 40, 41, 42, 43, 44, 45]. Figure 2 shows an example of an aortic dissection of a WHHL (age, 13months) and NZW rabbit (age, 21months) fed a high fat Western-type diet. Challenging the WHHL rabbit with an additional dietary stimulus causes accelerated formation of aortic lesions and eventually a full coverage of

the vessel's surface. As NZW rabbits do not spontaneously develop aortic atherosclerosis the dietary stimulus is required to trigger plaque generation. Compared to the WHHL, even at more advanced age the aortic surface of the NZW shows unaffected intact wall areas at the descending part.
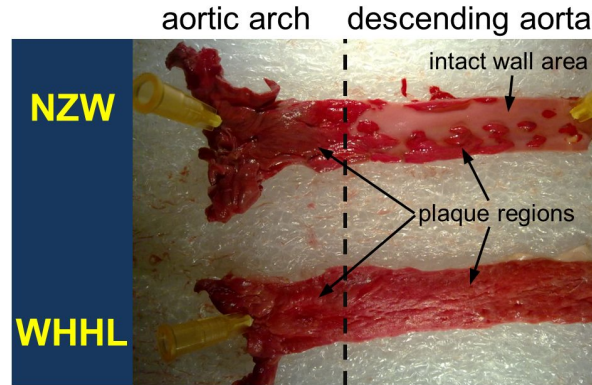
Figure 2: Gross inspection of the aortic dissection (aortic arch and descending aorta) of a WHHL (age, 13months) and NZW (age, 21months) rabbit fed a high fat Western-type diet. Both strains show a different extend of lesion coverage of the aortic surface. The Western-type diet lead to accelerated development of aortic atherosclerosis of the WHHL strain. The NZW rabbit requires a dietary stimulus to trigger plaque development.

For the NZW model, balloon catheter denudation, as a part of the preparatory regimen, is most extensively used to mechanically induce an arterial injury. It triggers a series of events comprising de-endothelialization, damage of medial smooth muscle cells, disruption of elastic lamina, intimal hyperplasia and a altered vasomotor response. Asada et al could show that the extent of vascular damage is dependent on the degree of the applied balloon inflation pressure [46]. In detail, medial injuries, disruption of elastic lamina (internal, medial) and alterations in endothelial-independent vasomotor response to norepinephrine (vascular constriction) were found to be pressure-dependent.

2.2 Mechanical arterial injury

In principle, balloon injury is performed from the iliac bifurcation to the renal artery (aortic arch) or vice versa, introducing a balloon catheter through the carotid artery or femoral artery, using a liquid or gas filled syringe to fill the balloon. During the passage

of the catheter, the abdominal aorta is markedly narrowing from proximal to distal (5 → 3mm ∅). Hence, a constant balloon volume introduces significant pressure variations (1-3bar, Figure 4) when retracted. Consequently, a not well-defined, heterogeneous plaque development can be expected, which represents a major drawback of this model. Moreover, catheter induced injury may also vary between operator as the handling of syringe and balloon filling requires training and adjusting a prescribed pressure to vessel diameter variations seems to be challenging. Figure 3A-D shows an example of a manual mechanical injury of ex vivo swine femoral arteries using a Fogarty 4F embolectomy balloon catheter (Edwards Lifesciences). Two operator performed balloon denudation's of femoral arteries by one to three passages of the catheter (x1 inj, x2 inj, x3 inj). In addition, a section of each artery was left uninjured and used as a *ground truth* measure (ctr). Endothelium dependent and independent vasomotor response (vascular relaxation) to acetylcholine (Ach) and sodium nitroprusside (SNP) were measured using the (un)injured arterial rings (two rings for each condition) by myograph experiments (Danish Myo Technology, DMT) [47]. In short, before vascular relaxation curves are measured, norepinephrine is used to precontract vessels to a level of 80% of maximum contraction response. After a stable contractile response is reached, increasing concentrations of Ach or SNP are used to relax the vessel. Recordings are change in contractile force in % (% of norepinephrine induced contraction) as a function of increasing Ach/SNP concentrations. Ach causes a endothelium-dependent dilation of vascular smooth muscle cells by releasing nitric oxide (NO) from endothelial cells. As the balloon injury leads to removal/damage of the endothelial layer, SNP is used as a control experiment to show endothelium-independent relaxation of smooth muscle cells. SNP is a nitric oxide donor and causes a direct relaxation of vascular smooth muscle cells. Figure 3A-B shows relaxation readings (% contractil force upon norepinephrine induction) as function of Ach concentration for two operators. It can clearly be seen from both graphs that a balloon retraction causes a removal of the endothelial layer (x1/x2/x3 inj) compared to the control rings (ctr) and that the extend of damage is in parallel with the number of passages. In detail, due to the lack of endothelial cells the release of NO is reduced and therefore the degree of relaxation. Figure 3B shows for the maximal injured rings (x3 inj) a trend to a paradoxical NO induced vasoconstriction. Similar behaviour to Ach in an in vivo study of ApoE(-/-) mice was reported by Phinikaridou et al [32]. Figure 3C shows the control experiment for *Operator #2* using SNP to trigger a endothelium-independent vasomotor response. For all (un)injured rings a relaxation of vascular smooth muscle cells is induced to the same extent. Figure 3D shows the re-

lative relaxation values as a function of Ach concentration normalized to the uninjured experiments for *Operator # 1 and 2*. This graph clearly reveals an operator dependent influence on the extent of vascular damage.
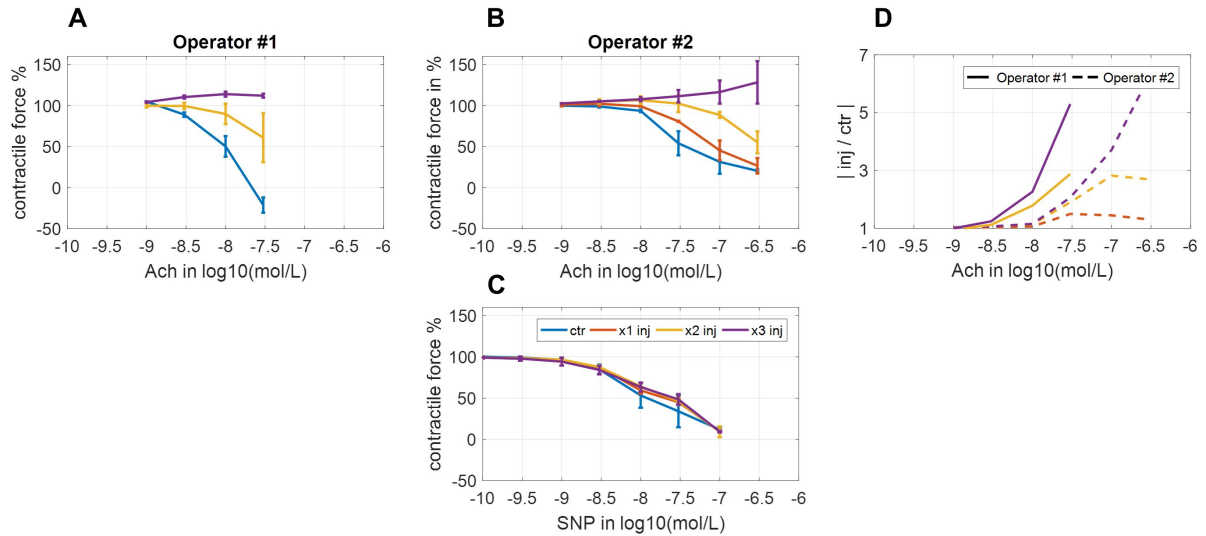
Figure 3: Myograph experiments on manual mechanical injured ex vivo swine femoral arteries using a Fogarty 4F embolectomy balloon catheter (Edwards Lifesciences). Balloon denudation of femoral arteries by one, two and three passages of the catheter (x1 inj, x2 inj, x3 inj). A section of each artery was left uninjured and used as control measure (ctr). **A-B** Operator #1 and 2: Relaxation readings as % of norepinephrine induced contraction as a function of increasing Ach concentrations. **C** Operator #2: Control experiment, relaxation readings as % of norepinephrine induced contraction as a function of increasing SNP concentrations. **D** Relative relaxation values as a function of increasing Ach concentration normalized to the uninjured experiments. Two rings were used for each condition. Measurements were done in collaboration with Rao Shailaja Prabhakar and Sasa Frank, Institute of Molecular Biology and Biochemistry, Medical University of Graz.

These findings support the demand for a technique generating more well-defined and reproducible lesions. The development of a standardized balloon injury device for the generation of reproducible minimal-invasive lesions in rabbits is proposed in the following.

2.3 Pressure controlled balloon injury

The JURY device, a pressure controlled balloon injury device is invented. It allows controlling the balloon volume (balloon inflation pressure) via a control circuit and therefore compensating for operator driven errors. Figure 4A-B shows an example of a manual and pressure controlled (JURY device) balloon denudation intervention. Recordings are the balloon inflation pressure (plus balloon volume in μl for the pressure controlled device) as a function of balloon retraction time. Figure 4A shows the traditional manual injury by a surgeon and the obvious difficulty to appropriate adjust the balloon filling to vessel diameter variations along the passage of the catheter. As a result, inconstant balloon inflation pressures are introduced. Figure 4B uses a control circuit to adjust the balloon volume (red curve) to vessel diameter variations. It can clearly be seen that the inflation pressure (blue curve) sticks with the predefined pressure value over the whole retraction distance. The device is a joint development of the Clinical Institute of Medical and Chemical Laboratory Diagnostics (Peter Opriessnig, Gunter Almer, Harald Mangge), Institute of Physiological Chemistry (Gerd Hoerl) and Institute of Biophysics (Wolfgang Sax), Medical University of Graz and is supported by the EU grant NanoAthero (grant agreement N° 30982). Moreover, the NanoAthero EU committee decided to prolong a work package (preclinical validation of nanosystems) for a year (March 2017 to February 2018) to evaluate the device in rabbits (n=28) with a volume of 70.000€.
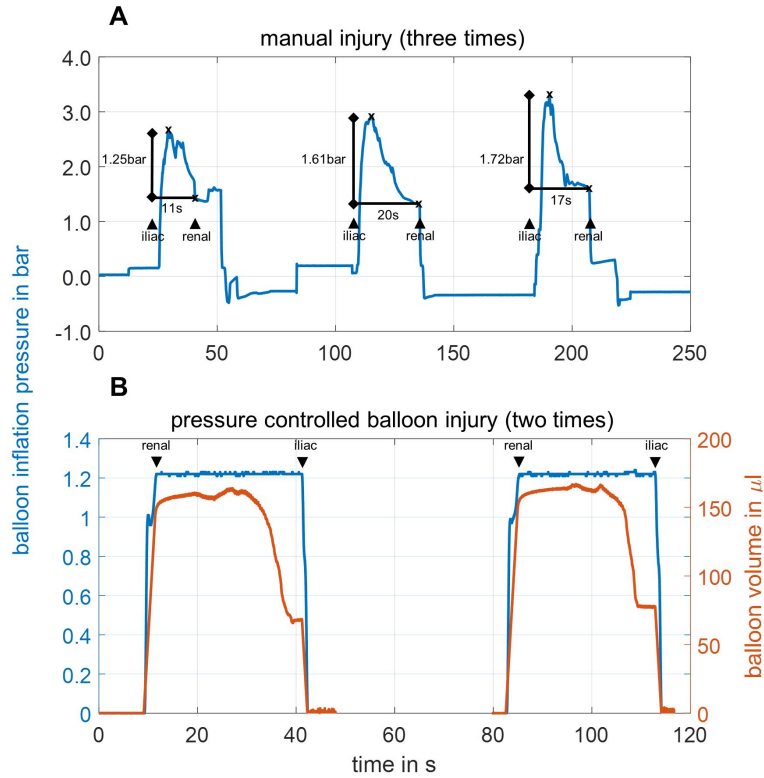
Figure 4: Manual vs pressure controlled balloon denudation. **A** Recordings of balloon inflation pressure in bar as a function of balloon retraction time. Surgery was done using the traditional manual injury. Inconstant balloon inflation pressures are visible. **B** Recordings of balloon inflation pressure in bar (blue curve) and balloon volume in μl (red curve) as a function of balloon retraction time. Surgery was done using the pressure controlled balloon device. Balloon volume adjusts to vessel diameter variations and therefore a prescribed pressure is kept constant.

A patent application (Balloon catheter device for use in an aorta of a rabbit or a human being; patent application number: GB 1614500.5) was requested for the device at the *Intellectual Property Office, Great Britain (www.ipo.gov.uk)* and the grant for the patent application was the 25th of August, 2017. The application text and drawings were elaborated in collaboration with *Maiwald Patentanwaltsgesellschaft mgH (Munich, German, www.maiwald.eu)* and the *Research Promotion and Technology Transfer (Michaela Semlitsch, Heidi Schmitt), Medical University of Graz*. A combined search and examination report on the patent act was composed by the *Intellectual Property Office, GB* with the 14th of February, 2017. The report just lists documents of category A (document indicating technological background and/or state of the art). In addition to the preclinical part of the application text it also includes the use in a human being to

cover a possible pressure controlled balloon thrombectomy. This translational application was discussed in collaboration with Prof. Cohnert (Division of Vascular Surgery, Medical University of Graz). In short, the implementation (August 2009) of the European Working Time Directive (2003/88/EC) caused widespread concern in surgery as it introduced a substantial reduction in duty-hours for doctors-in-training [48]. As a consequence, this European regulation leads to detrimental effects on patient care, reduced availability of medical staff and a reduction in time for training junior doctors. Furthermore, a questionnaire survey addressing day case surgery of modern day surgical trainees revealed a low and inconsistent exposure due to rota issues and lack of encouragement of seniors despite being aware of the importance of the training [49]. Such detrimental conditions require tailored training procedures for junior doctors compensating for the lack of training time. The further development of the frequently used balloon thromboembolectomy in acute arterial occlusion to a pressure-controlled technique would permit junior doctors to manage such a surgery in less training time and more important would improve patient safety and potentially lower catheter induced arterial injury [50]. This is very important as the procedure is the most frequently required emergency procedure in vascular surgery, for example with more than 20.000 operations/year in Germany [51]. To verify the efficiency of such a device first steps include the implementation of a pressure sensor to the balloon catheter for monitoring pressure behavior during surgery between professionals and doctors-in-training. In a second step, pressure-controlled thromboembolectomy can be applied to compare the outcome of the standard surgery with the improved technique.

2.4 Component description

In the following, the pressure controlled balloon injury device and its components are listed and important parts explained in short. A detailed description of the components and their interactions as well as several embodiments of the invention can be found in the patent application text attached in *Chapter 9.1*. Again, the patent application text of the **patent** *Balloon catheter device for use in an aorta of a rabbit or a human being* with the **patent application number** (GB 1614500.5) was elaborated with the **patent attorney's office** *Maiwald Patentanwaltsgesellschaft mgH (Munich, German, www.maiwald.eu)*. Figure 5 shows the setup of the device and its components.
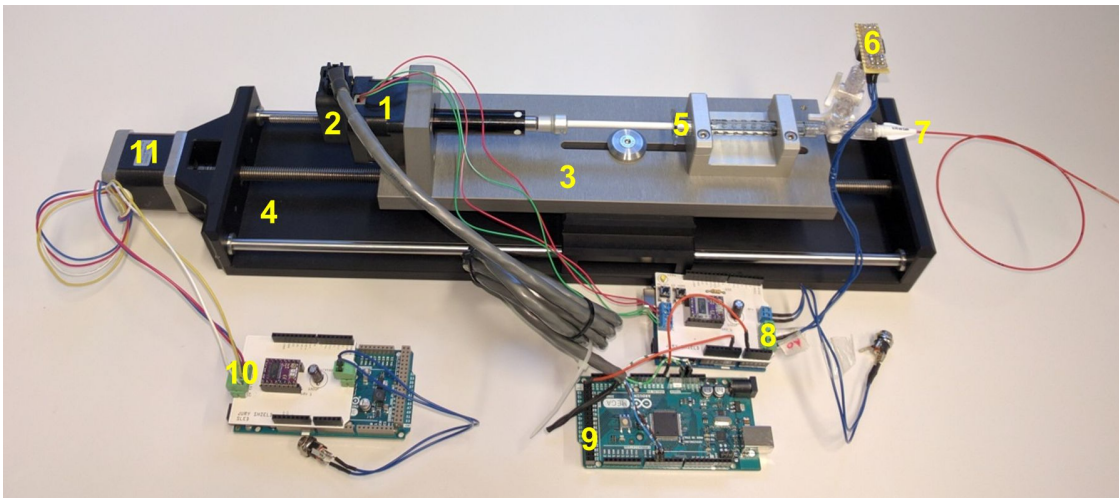
Figure 5: Pressure controlled balloon injury device (The JURY device). **1** linear actuator (controlled by *JURY shield*) **2** quadrature (rotary) encoder (to measure balloon volume) **3** holder **4** sled **5** syringe **6** pressure sensor (e.g. signal conditioned; 4V span; 0-100psi or luer fitting sensor) **7** balloon catheter **8** *JURY shield:* stepper driver + control circuit unit **9** quadrature encoder signal and pressure data recording unit **10** *JURY sled shield:* stepper driver (DRV8825, Pololu) + sled motion direction control **11** rotative stepper (controlled by *JURY sled shield*). **Addendum to (8)** Components: stepper driver (DRV8825, Pololu) to operate the linear actuator; On/Standby Button; Go-Home Button; Cal Button; pressure sensor connector; linear actuator connector.

In a future refinement, the control units 8, 9 and 10 of the prototype can be integrated into one single control unit which fulfills all the functions of the listed units. Moreover, the wire-based solution for encoder signal and pressure data recording to a computer unit can be refined into a wireless communication. Theses steps will help to further

improve usability.

Function of main components:

JURY shield (8):

Job of the shield in combination with a *Arduino Uno* (8) is to hold a stable predefined balloon inflation pressure over the whole retraction distance. The balloon inflation pressure is measured by a pressure sensor (6). The linear actuator (1) coupled to a syringe (5) adjusts the volume of the balloon (7) (filling/emptying) depending on the actual balloon inflation pressure. The whole system is filled with a fluid (e.g. NaCl). The predefined balloon inflation pressure is hold by a bang-bang control without hysteresis (Figure 6).

Job of the sketch uploaded to the microprocessor:
Cal Button: Offset of pressure sensor readings caused by insufficient venting of the catheter tubing is measured and corrected (4VDC span).
On/Standby Button: Balloon is filled to the predefined balloon inflation pressure and pressure is hold by the bang-bang control without hysteresis. Another button acknowledgement causes a freezing of the system.
Go-Home Button: Linear actuator goes to home position (fully emptying of the balloon).

Variables: upper(lower) balloon inflation pressure limit (U(L)BIPL) in bar; actual balloon inflation pressure (ABIP); control variable (CV, 0: balloon emptying, 1: balloon filling);

Figure 6 shows the implemented bang-bang control without hysteresis to adjust the balloon volume (balloon inflation pressure) to vessel diameter variations while keeping a predefined pressure. The top graph shows the effect of the afore mentioned 'code-part' and principle behaviour of the system. In detail, if the On button is pressed CV is set to 1 and the balloon is filled til UBIPL is reached. This holds true even if ABIP is between LBIPL and UBIPL because the sketch is processed sequentially and the second IF condition overwrites the value for CV from the first IF condition. Now ABIP overshoots UBIPL, CV is set to 0 and the balloon volume is decreased. Next, ABIP undershoots

UBIPL, CV is set to 1 and the balloon is filled again. The last two steps are repeated continuously and the balloon volume oscillates at the level of the predefined pressure driven by the value of the control variable (bottom graph, 1: balloon filling; 0: balloon emptying). The procedure is terminated by pressing the Go-Home button and finally the balloon is emptied. Again, Figure 4B shows the resulting practical behaviour of the control circuit. From the 'code-part' it can also be seen that exchanging LBIPL with UBIPL and UBIPL with LBIPL produces a bang-bang control with hysteresis. This kind of implementation would lead to a oscillation of the balloon volume between the lower and upper BIPL.
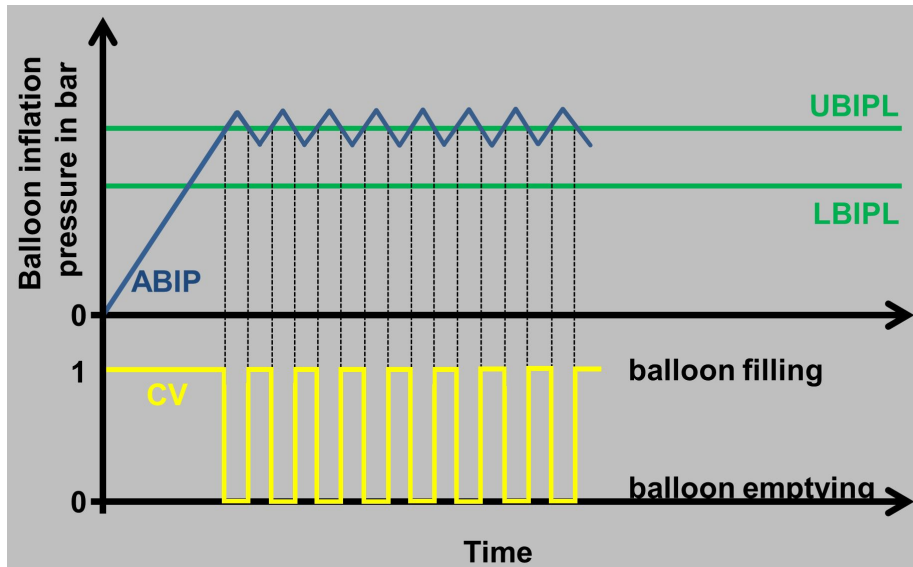
Figure 6: Bang-bang control without hysteresis to adjust balloon volume (balloon inflation pressure) to vessel diameter variations while keeping a predefined pressure. **Top graph** Balloon inflation pressure as function of balloon retraction time. **Bottom graph** Control variable switching between 0 (balloon emptying) and 1 (balloon filling). ABIP, actual balloon inflation pressure; U(L)BIPL upper(lower) balloon inflation pressure limit; CV, control variable.

Quadrature encoder signal and pressure data recording unit (9):

A *Arduino Mega 2560* is used to record pressure and quadrature encoder signals and to send the data via COM port to MATLAB for final recording and 'real-time' visualization of the balloon retraction task. The rotary encoder (2) counts the steps of the linear actuator (1) which in turn can be translated into balloon volume values (see Figure 4). For example, the linear actuator with a resolution of 0.0121 mm/step together with the used

syringe with an inner diameter of 4.7mm results in a volume resolution of $0.2\mu l$/step. Hence, the volume resolution multiplied with the counts of the rotary encoder gives the final balloon volume.

JURY sled shield (10):

A *Arduino Due* in combination with the sled shield, consisting of a stepper driver (DRV8825, Pololu), is used to generate a linear movement of the sled by a rotative stepper (11) at a predefined constant speed (mm/sec) and finally to retract the balloon catheter (7) from the renal to the iliac artery position (or vice versa). For example, the spindle drive (M10) with a resolution of 1.5mm/revolution in combination with the rotative stepper results in a final resolution of 1.5mm/200steps. Hence, the total amount of steps for a predefined retraction distance as well as the steps/sec for a predefined constant speed (mm/sec) can be calculated.

MATLAB GUI:

To improve the usability of the device a Matlab (The MathWorks, Inc.) graphical user interface (GUI) is used to initialize the JURY shield (8) and data recording (9) units and to send commands for linear movements to the JURY sled unit (10). Communication to the boards is established via serial COM ports. Figure 7 shows the implementation of the GUI using MATLAB.
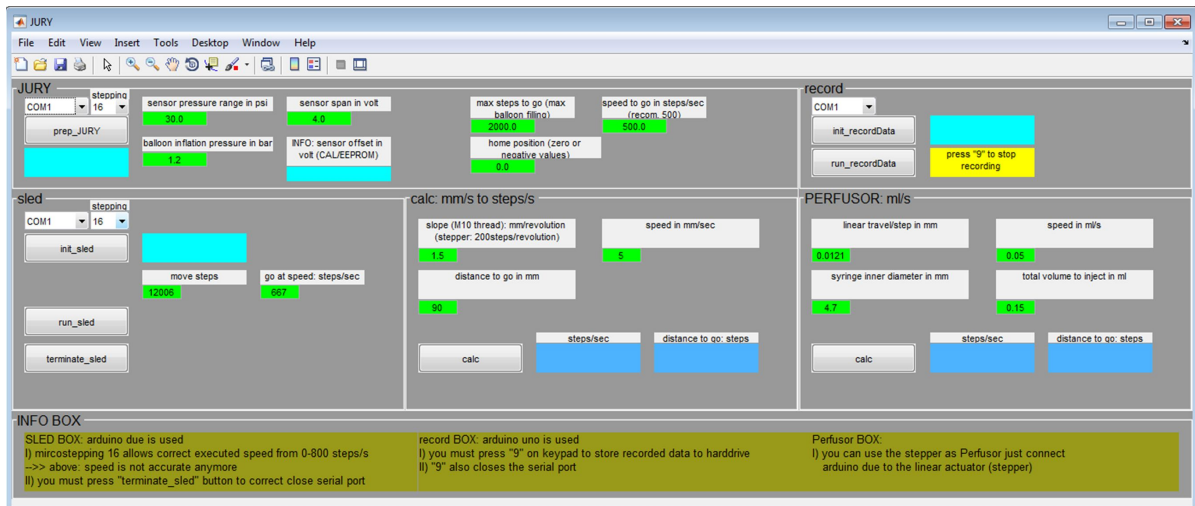
Figure 7: JURY MARLAB GUI for a user-friendly interaction with the JURY device. GUI is used to initialize the JURY shield (8) and data recording (9) units and to send commands for linear movements to the JURY sled unit (10). Parameter initialization: **JURY** COM port; *microstepping*: 1,4,16,32-fold; *sensor pressure range* in psi; *sensor span* in volt; *balloon inflation pressure* in bar; *max steps to go* (safety precaution to prevent for balloon burst); *home position*: zero or negative value; *speed to go* in steps/sec. **record** COM port **sled** COM port; *microstepping*: 1,4,16,32-fold; *move steps* in steps and *go at speed* in steps/sec **calc** This part is used to convert *distance to go* in mm to *move steps* in steps and *speed* in mm/sec to *go at speed* in steps/sec. **Perfusor** Replacing the rotative stepper (11) by the linear actuator (1) to the sled shield unit (10) enables a perfusor device. *linear travel/step* in mm; *speed* in ml/s; *syringe inner diameter* in mm; *total volume to inject* in ml.

3 Vessel wall MRI: imaging techniques

3.1 Introduction

Risk stratification of atherosclerosis by traditional angiographic techniques alone may obscure the true impact on future cardiovascular events. The complexity of an atherosclerotic plaque, rather than the degree of luminal narrowing, is thought to be a valuable predictor of lesion vulnerability [27]. Magnetic resonance imaging (MRI) is a non-invasive technique without the use of ionizing radiation and its inherent soft tissue contrast allows the determination of anatomical and functional structures. The ability to acquire high resolution images makes MRI a well suited tool to delineate key factors of plaque vulnerability. Such key determinants can be subdivided into morphological (area/volume: wall, lumen, plaque) and compositional features (size: lipid rich necrotic core (LRNC), intra plaque hemorrhage (IPH), fibrous cap (FC), calcification (CA)). MR techniques applied for feature detection are commonly based on so called multicontrast-weighted sequences. Moreover, contrast enhanced MRI (CE-MRI) further extends the scope of multicontrast weightings. Signal alterations induced by the administration of a non-specific gadolinium chelate lead to an improved discrimination between plaque tissues [52]. To face the limitation of these techniques in revealing information on the cellular level, biomarker targeted nanoparticles provide an encouraging complement in CE-MRI. Molecular imaging aims to monitor processes on the cellular level using functionalized probes by targeting biomarkers of apoptosis, necrosis, angiogenesis, thrombosis and inflammation (see *Chapter 5*). In the following section vessel wall imaging techniques are presented along with strategies to minimize image corruption introduced by flowing blood spins and sequences used to delineate certain plaque components.

3.2 Washout and spatial presaturation (inflow saturation)

Dark blood angiography with conventional RF spin echo or TSE (turbo spin echo) is intrinsically achieved by the outflow of excited blood from the slice of interest between the 90° RF excitation and 180° RF refocusing pulse as can be seen from Figure 8. The minimum required velocity for a complete washout of excited flowing spins perpendicular to the imaging slice can be expressed by Eq.(1) and Eq.(2), respectively [53]. From these equations it is obvious that a reduction in slice thickness and/or an increase in echo time

17

lowers the minimum velocity. The latter property clearly depicts T_2-weighted RF spin echo or TSE sequences to be superior in generating dark blood effects compared to the T_1-weighted counterpart.
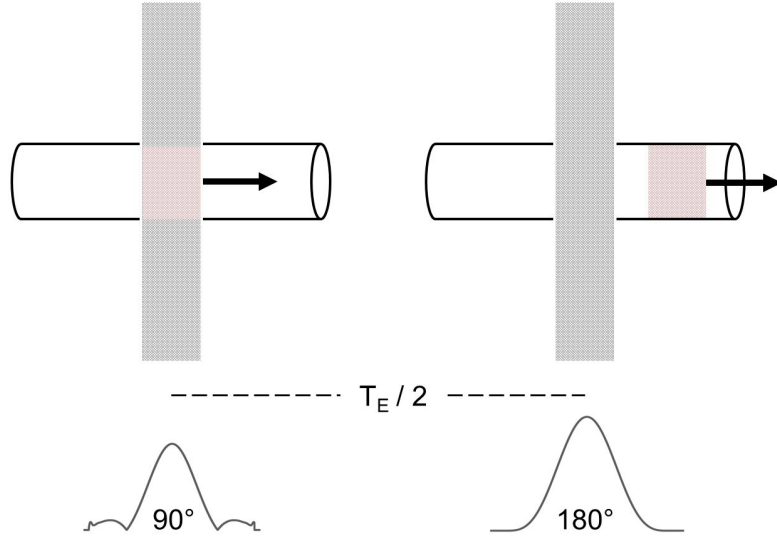
Figure 8: Dark blood angiography with RF spin echo / TSE sequences. Both, the 90° RF excitation and the 180° refocusing RF pulse are experienced by the static (gray pattern) tissue. As the flowing spins (red pattern) leave the imaging plane before the 2nd RF pulse, their is no signal contribution to the formed spin echo.

$$v_\perp = \frac{\Delta z}{T_E/2} \tag{1}$$

$$v_\perp = \frac{\Delta z}{T_{E_{eff}} - t_{esp}/2} \tag{2}$$

An additional method to improve the contrast between vessel lumen and wall are spatial presaturation bands positioned up- and downstream from the imaging slice [54]. Cancelation of the zipper like artifacts (ghosting) propagating along the phase-encoding direction are realized by dephasing of spins across the saturation bands just before image excitation. To avoid chemical shift artifacts caused by periadventitial fat, a spectral fat saturation pulse is commonly applied in addition. However, an appropriate configuration of the slice of interest and the spatial presaturation band (thickness Δz and

18

RF bandwidth Δf) allows suppression of unwanted fat signals in the imaging slice *for free*. The technique is called spatially separated lipid presaturation (SLIP) and uses the chemical-shift ($\delta_{ppm_{fat}} f_0$) effect [55]. As can be seen from Eq.(3) the maximum gap (gap_{max}) between excitation slice ($\Delta z_{exc.slice}$) and presaturation slab ($\Delta z_{pres.slab}$) is field dependent and of course a certain presaturation band thickness is required.

$$gap_{max} = \delta_{ppm_{fat}} f_0 \left(\frac{1}{\Delta f_{pres.pulse}} \Delta z_{pres.slab} - \frac{1}{\Delta f_{exc.pulse}} \Delta z_{exc.slice} \right) - \Delta z_{exc.slice} \quad (3)$$

Figure 9A-B shows dark blood imaging examples of a New Zealand White (NZW) rabbit abdominal aorta using a 2D T_2 and T_1-weighted TSE sequence with spatial presaturation bands positioned up- and downstream of the multislice package. It can clearly be seen that compared to the T_2-weighted sequence the T_1-weighted shows a prominent contribution of the flowing spins due to the shortened time for the blood to leave the imaging slice.
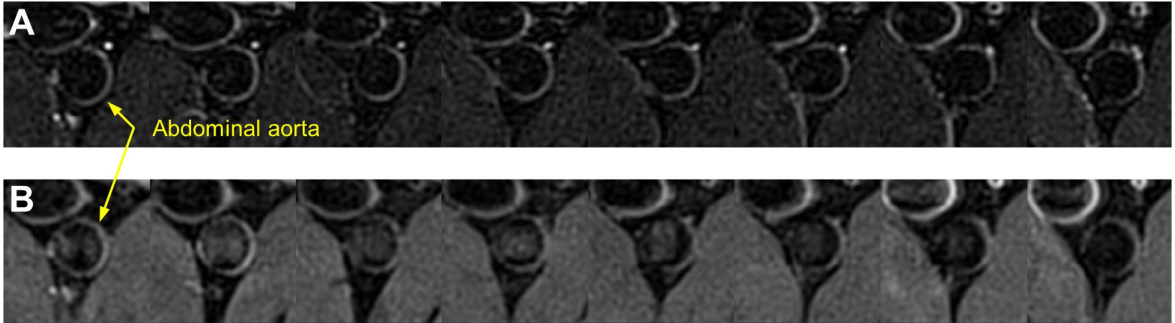
Figure 9: Dark blood imaging of a New Zealand White (NZW) rabbit abdominal aorta using a 2D multislice T_2 and T_1-weighted TSE sequence with spatial presaturation bands positioned up- and downstream measured @3T Siemens Prisma and 15CH TxRx knee coil. **A** 2D T_2w TSE with T_R=2500ms, T_E=64ms, turbofactor=7, FOV=120x98mm^2, matrix=384x312, bandwidth=265Hz/pixel, resolution=312x312μm^2, slice thickness=3mm, NEX=4, 8 slices, spectral fat suppression, 8min acquisition time **B** 2D T_1w TSE with T_R=600ms, T_E=13ms, NEX=6, 5.5min acquisition time and all other parameters held constant.

These techniques permit an improved delineation of the wall architecture which would be otherwise obscured by the blood flow artifacts. Plaque mimicking artifacts introduced by residual signals created by slow flowing blood as well as complex flow patterns restrict their effectiveness but nevertheless do not prolong imaging time and improves anatomical quality.

3.3 Double inversion recovery (DIR)

As already mentioned, the minimum velocity of excited flowing spins to be washed out from the image section in a SE or TSE sequence can be effectively reduced by increasing the (effective) echo time (T_E) or decreasing the slice thickness (see Eq.(1) and Eq.(2)). In addition, deviation from a perpendicular orientation of the image section to the vessel increases the minimum velocity but the effect can be partly compensated by reducing the section thickness. In contrast to the TE dependent wash out effect and the spatial saturation method which perform well for fast through plane flow, the much longer inversion time T_I defining the elapsed time between the DIR and host module (Figure 10) enables a better suppression of slow flowing intravascular signal [56]. As can be seen from Figure 10 the DIR module is made up of a non-selective 180° RF pulse (e.g. hard pulse, adiabatic hyperbolic-secant) to invert the spins of the whole body and is immediately followed by a spatial selective 180° RF pulse (e.g. adiabatic hyperbolic-secant) to reinvert the spins of the imaging slice.
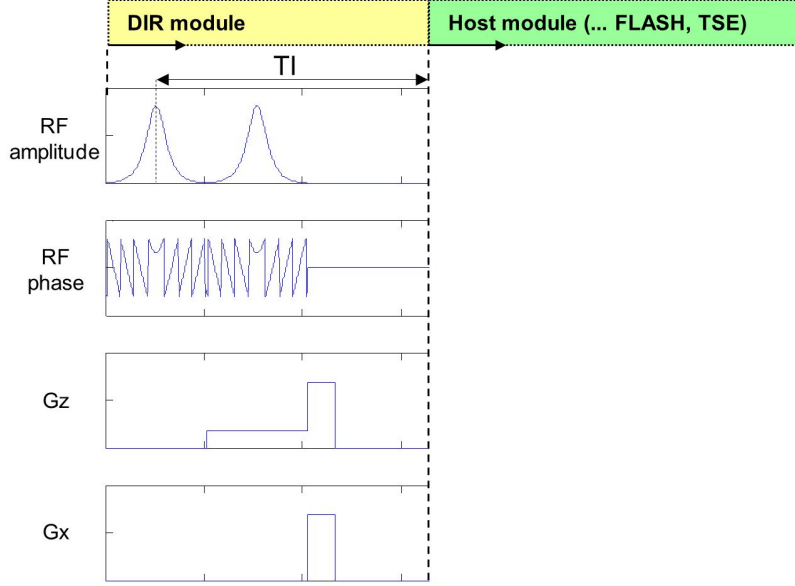
Figure 10: Pulse diagram of the DIR preparation module. The DIR module consists of a non-selective 180° RF pulse which is immediately followed by a spatial selective 180° RF pulse (in this case both are adiabatic hyperbolic-secant RF pulses). The DIR preparation and host module are separated by T_I which is determined by crossing zero magnetization of the inflowing blood spins.

Figure 11A shows examples of *Bloch equation* simulations of the longitudinal magnetization (M_z of replacing blood spins) as a function of time for a set of repetition times T_R.

The magnetization is calculated based on time-domain simulations of Bloch equations $(\frac{dM_z}{dt} = -\frac{M_z - M_0}{T_1}; \frac{dM_x}{dt} = -\frac{M_x}{T_2}; \frac{dM_y}{dt} = -\frac{M_y}{T_2})$ using Matlab (The MathWorks). Longitudinal and transverse relaxations are exponential decay processes and modeled using $M_{z(t)} = M_{z(t=0)}e^{-t/T_1} + M_0(1 - e^{-t/T_1})$, $M_{x(t)} = M_{x(t=0)}e^{-t/T_2}$ and $M_{y(t)} = M_{y(t=0)}e^{-t/T_2}$. Together with the three dimensional rotation matrices $\mathbf{Rx}(\theta)$, $\mathbf{Ry}(\theta)$ and $\mathbf{Rz}(\theta)$ precession and excitation can be realized. The whole process can be rewritten in matrix form as $\mathbf{M_{t,n}} = \mathbf{AM} + \mathbf{B}$ where $\mathbf{A} = diag(E2, E2, E1)\mathbf{Rz}(\theta), \mathbf{M} = \mathbf{Rx,y}(\theta)[0, 0, M_0]'$ for the first or $\mathbf{Rx,y}(\theta)\mathbf{M_{t=T_R,n-1}}$ for the n-th excitation and $\mathbf{B} = M_0[0, 0, 1 - E1]'$ with $E1 = e^{-t/T_1}$ and $E2 = e^{-t/T_2}$ describing the exponential decay processes and M_0 the equilibrium magnetization.

The inverted M_z (Figure 11A) of the blood outside the image section recovers along the z axis and replaces the non-inverted blood of the imaging slice. The T_I is determined so that the inflowing spins cross zero magnetization when the host sequence is played.

21

The appropriate inversion time as can be seen from Figure 11A (M_z crossing zero magnetization) can be calculated from Eq.(4) (steady state) and is based on repetition time T_R and relaxation time T_1 of the blood.

$$T_I = T_{1_{blood}} \, ln \left(\frac{2}{1 + e^{-T_R/T_{1_{blood}}}} \right) \tag{4}$$

It can also be seen from Figure 11A that the amount of *dummy scans* to reach a *steady state* condition for the replacing blood spins increases with decreasing T_R.
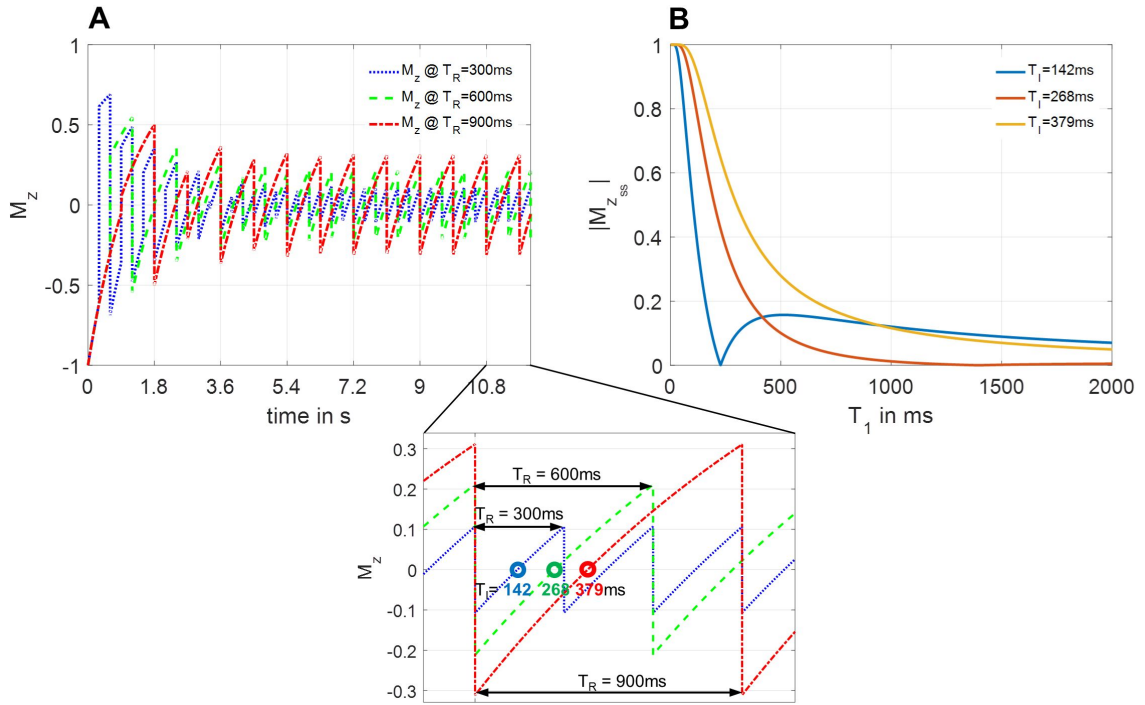
Figure 11: Simulations on the longitudinal magnetization M_z of replacing blood spins for a DIR preparation. **A** Bloch equation simulation of M_z (replacing blood spins) as a function of time for T_R=300/600/900ms and a $T_{1_{blood}}$ of 1400ms. M_z crosses zero magnetization at T_I=142/268/379ms as visualized on the zoomed-in view. **B** Simulation of $M_{z_{ss}}$ by Eq.(5) for T_I=142/268/379ms, T_R=600ms and a $T_{1_{blood}}$ of 1400ms. The combination with the optimum T_I of 268ms results in a perfect nulling of blood spins with a T_1 relaxation time of 1400ms. Simulations are realized for tissue relaxation times @3T.

The *steady state* M_z ($M_{z_{ss}}$) for the replacing blood spins can be expressed by Eq.(5) (reprinted from Yarnykh et al [57]).

$$M_{z_{ss}} = 1 - \frac{2e^{-T_I/T_1}}{1 + e^{-T_R/T_1}} \tag{5}$$

Figure 11B shows examples of simulations by Eq.(5) for a set of T_I and a certain T_R. It is obvious that this method is sensitive to changes in relaxation time T_1 of the blood. In addition, the use of a T_I below or above the optimum value will augment the contribution of the inflowing spins to the final signal of the imaging slice.

Figure 12 shows examples of Bloch equation simulations for $M_{xy}(T_E)$ on different static tissues and the consequent saturation effect introduced by the use of a DIR preparation module. The extend of reduction in static tissue signal (M_{xy} ratio of a DIR-GRE and GRE) depends on T_R. The shorter T_R the stronger the saturation effect which is obvious as a decrease in T_R shortens T_I and consequently the recovery time M_z for the static tissue between subsequent repetitions.
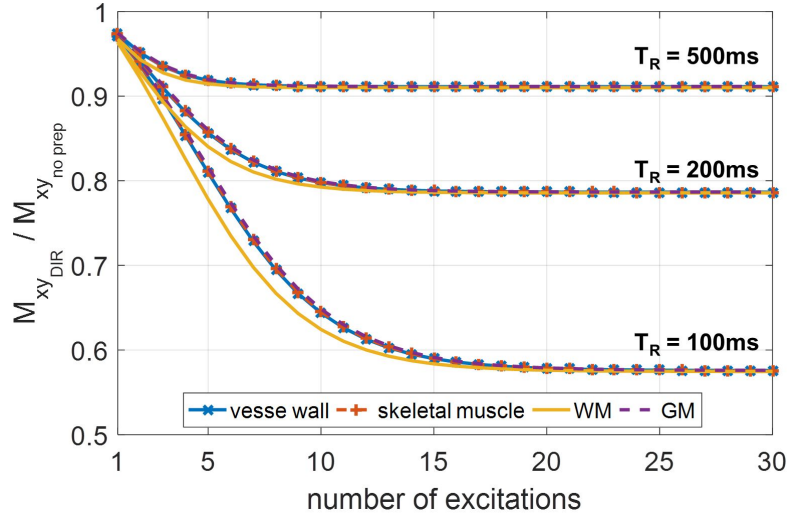
Figure 12: Bloch equation simulation on the transverse magnetization M_{xy} of static tissues with and without a DIR preparation module and a GRE as host sequence for T_R=100/200/500ms and T_I=49/96/228ms, respectively. GRE parameters are T_E=5.3ms, $\alpha = 40°$; DIR module time between non- and spatial-selective 180° RF pulse is 21ms; T_1/T_2 relaxation times: vessel wall = 1400/120ms; skeletal muscle = 1420/32ms; WM = 1110/56ms; GM = 1470/71ms corresponding to [58]. The ratio between M_{xy} of a DIR-GRE and GRE is plotted as a function of excitations (number of repetitions, approach to steady state). Static tissue is saturated by the DIR preparation and the extend depends on T_R. M_{xy} was taken at T_E. Simulations are realized for tissue relaxation times @3T.

Figure 13A-C compares dark blood imaging of a New Zealand White (NZW) rabbit common carotid artery using a 2D T_1-weighted DIR-TSE and a 2D T_1-weighted TSE sequence with spatial presaturation bands positioned up- and downstream of the imaging slice. The carotid wall of the DIR preparation shows a isointense pattern compared to the surrounding muscle tissue (Figure 13A) whereas the wall is hyperintense (plaque mimicking artifact) on the sequence with the presaturation bands (Figure 13B) due to an insufficient suppression of slow flowing blood. Figure 13C is the reconstructed difference image and clearly depicts the intrinsic slow flow related vessel wall artifact introduced by unsaturated blood spins in the imaging slice (red arrowhead).

Figure 14A-C shows dark blood imaging of a Watanabe heritable hyperlipidemic (WHHL) rabbit abdominal aorta (rabbit model to study atherosclerosis) using a 2D T_1w/T_2w/PDw DIR-TSE. It can be seen for all three cases that the lumen signal is completely nulled and do not contribute to the final wall signal.
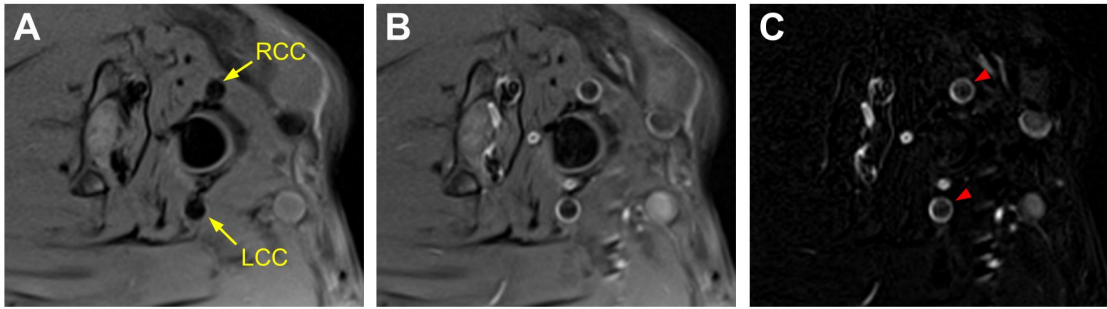
Figure 13: Dark blood imaging of a New Zealand White (NZW) rabbit common carotid artery *(single-slice)* using a 2D T_1-weighted DIR-TSE and a 2D T_1-weighted TSE sequence with spatial presaturation bands positioned up- and downstream measured @3T Siemens TimTrio and 2x4CH CPC coil. **A** 2D T_1w DIR-TSE with T_R=600ms, T_E=11ms, T_I=268ms, turbofactor=7, FOV=120x101mm^2, matrix=384x324, bandwidth=240Hz/pixel, resolution=312x312μm^2, slice thickness=2mm, NEX=8, spectral fat suppression, ~4min acquisition time; **B** 2D T_1w TSE with all parameters held constant except for spatial presaturation bands instead of the DIR preparation. **C** Difference image reconstructed from *(B)* minus *(A)*; red arrowhead shows plaque mimicking artifact.
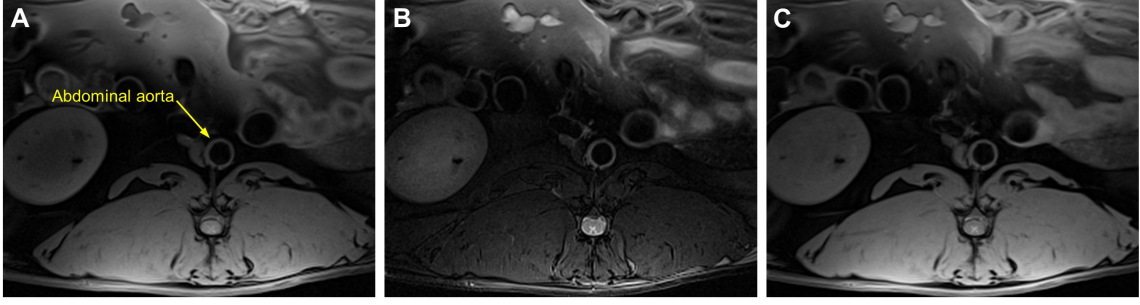
Figure 14: Dark blood imaging of a Watanabe heritable hyperlipidemic (WHHL) rabbit abdominal aorta (rabbit model to study atherosclerosis) using a 2D $T_1w/T_2w/PDw$ DIR-TSE measured @3T Siemens TimTrio and 2x4CH CPC coil. **A** 2D T_1w DIR-TSE with T_R=600ms, T_E=9.7ms, T_I=268ms, turbofactor=7, FOV=120x120mm^2, matrix=384x384, bandwidth=266Hz/pixel, resolution=312x312μm^2, slice thickness=2mm, NEX=8, spectral fat suppression, $\sim$4min acquisition time; **B** 2D T_2w DIR-TSE with T_R=2400ms, T_E=68ms, T_I=738ms, NEX=3, $\sim$7min acquisition time and all other parameters held constant. **C** 2D PDw DIR-TSE with T_R=2400ms, T_E=9.7ms, T_I=738ms, NEX=3, $\sim$7min acquisition time and all other parameters held constant.

Typical T_I values for a DIR-TSE range from 300 to 700ms (T_R: 600 to 2500ms), therefore DIR performs superior to the wash out and spatial saturation method to suppress signals from slowly flowing or recirculating blood as can be seen from Figure 13 and Figure 14. The major drawback of this technique is its single slice nature, the dependence on a certain T_1 blood value for a given T_R and the consequent extended imaging time to acquire a set of slices. The T_R dependent saturation effect of static tissue is more pronounced for a GRE sequence as T_R is usually shorter compared to TSE sequences.

Multislice double inversion recovery (mDIR):
The sequential acquisition of a 2D imaging volume in conjunction with multiple weightings makes the DIR technique susceptible to prolonged examination times. To counteract this drawback multislice DIR (mDIR) represents an interleaved approach to reduce the overall scan time [59, 60, 61].
The *dual-slice DIR-FSE* approach is defined by a non-selective 180° RF pulse and two consecutive slice-selective 180° RF pulses with an inversion time prescribed to the first slice [59]. This technique halves the scan time of the conventional DIR without sacrificing the image contrast of the second slice which acquisition window immediately follows the first echo train. From Eq.(5) it can be derived that a T_I window of about 100 to 200ms preserves an adequate suppression of the inflowing blood spins following the zero crossing point (7 to 15% recovery of the longitudinal blood magnetization). In addition,

the dual-slice method uses long echo trains to collect data which in principle introduces T_2 blurring but shortening of the echo spacing by modifying the refocusing RF pulses helps to narrow the acquisition windows of a slice. Hence, a good tradeoff between an adequate scan time and minimal vascular signal can be achieved. Time efficiency is further improved using an mDIR-FSE approach in which consecutive slice-selective 180° reinversion RF pulses are replaced by a slab-selective (slice-pack) one [61]. The sequence plays N preparative DIR modules for N slices per TR. As can be seen from Eq.(6) the inversion time is determined by the number of slices and spacing between the non-selective 180° RF pulses is controlled by TR/N (reprinted from Yarnykh et al [61]).

$$T_I(N) = T_{1_{blood}} ln \left(\frac{2}{1 + e^{-T_R/(NT_{1_{blood}})}} \right) \tag{6}$$

This kind of regime provides nulling of flowing spins for each slice when the read out part is applied. In comparison to a spatial presaturation setup, Yarnykh et al showed that the multislice approach performs superior in nulling blood for the tested slice packs whereas similar flow suppression is observed for up to six slices when compared to the single-slice DIR method. One major drawback is the saturation of stationary tissue with increasing N (decreasing T_I). At a slice pack size of eight (N=8) the DIR preparation accounts for already one half of the saturation effect when compared to the single-slice (N=1) DIR setup (signal measured in muscle). Nonetheless, at comparable signal loss level of stationary tissue to a TSE sequence with inflow saturation, the four slice mDIR shows obvious better flow suppression and a four-fold reduction in examination time when compared to the single-slice DIR. In a preceding mDIR-FSE implementation by Parker et al consecutive slice-selective reinversion RF pulses are played following the non-selective one each time a slice is acquired. The sequence therefore requires N non-selective and N^2 slice-selective RF pulses for N slices per T_R. It is obvious that compared to the mDIR approach of Yarnykh et al. this implementation suffers from specific absorption rate (SAR) and therefore restricts the number of slices acquired per T_R.

26

3.4 Quadruple inversion recovery (QIR)

MR techniques applied for feature detection are commonly based on multicontrast-weighted sequences and are often extended by contrast enhanced MRI (CE-MRI). The administration of a non-specific gadolinium chelate improves the discrimination between plaque tissues [52]. The shortening of blood T_1 introduced by the injected agent in turn requires an adjustment of the inversion time T_I in (m)DIR techniques to preserve the dark blood contrast. Unfortunately this kind of modification directly influences the saturation of stationary tissue and consequently the quantitative analysis of CE values [57]. To overcome this limitation a quadruple IR (QIR, Figure 15) with T_1 insensitive blood pool suppression was introduced by Yarnykh et al [57]. As can be seen from Figure 15 the QIR (single-slice technique) plays two consecutive DIR preparation modules followed by a host sequence (e.g. TSE read out etc). Two inversion times prescribe the time between the two DIR modules and the host sequence. After reaching the steady state, nulling of flowing spins over a broad range of shortened T_1's is achieved. That implies no modification of the two inversion times for the post contrast measurement. Especially designed for T_1-weighted imaging and CE, the dark blood contrast between pre- and post-infusion imaging can be fully preserved.
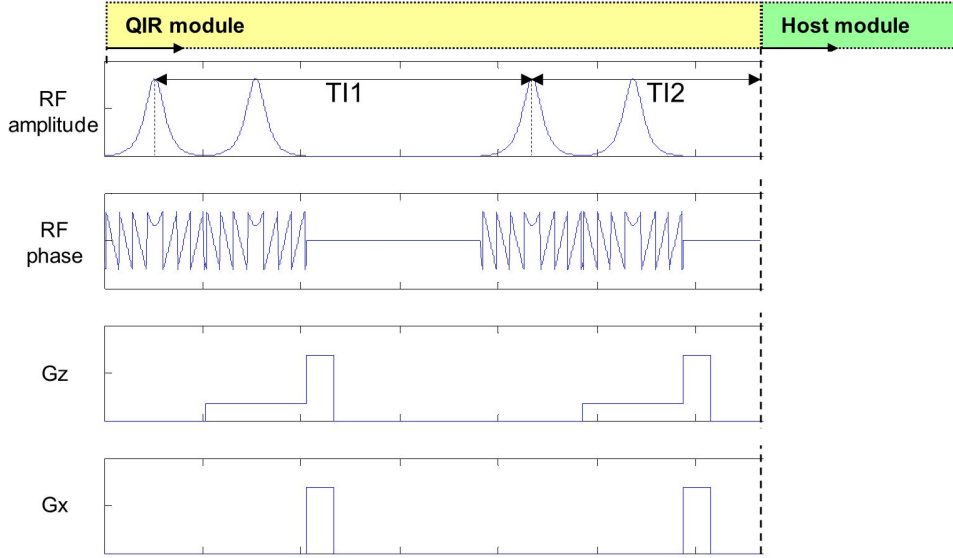
Figure 15: Pulse diagram of the QIR preparation module. The QIR module consists of two consecutive DIR preparation modules followed by a host sequence. In this case the DIR modules consist of an adiabatic hyperbolic-secant non-selective 180° and spatial selective 180° RF pulse. The QIR preparation and host module are separated by two T_I's for minimizing a range of blood T_1 values and consequently their contribution to the imaging slice.

Figure 16A shows examples of *Bloch equation* simulations on the longitudinal magnetization M_z of replacing blood spins as a function of time for a set of repetition times T_R. The inverted M_z of the blood outside the imaging section recovers along the z-axis, overshoots the zero magnetization to T_{I_1} and is again inverted by the second DIR module. M_z recovers again to a region close to the zero magnetization $(T_{I_1} + T_{I_2})$ and finally the host sequence is played. The appropriate set of T_I's can be calculated by minimizing Eq.(7) for a desired range of T_1's and a prescribed T_R. It can be seen from Figure 16A as for Figure 11A that the amount of dummy scans to reach a steady state condition increases with decreasing T_R.
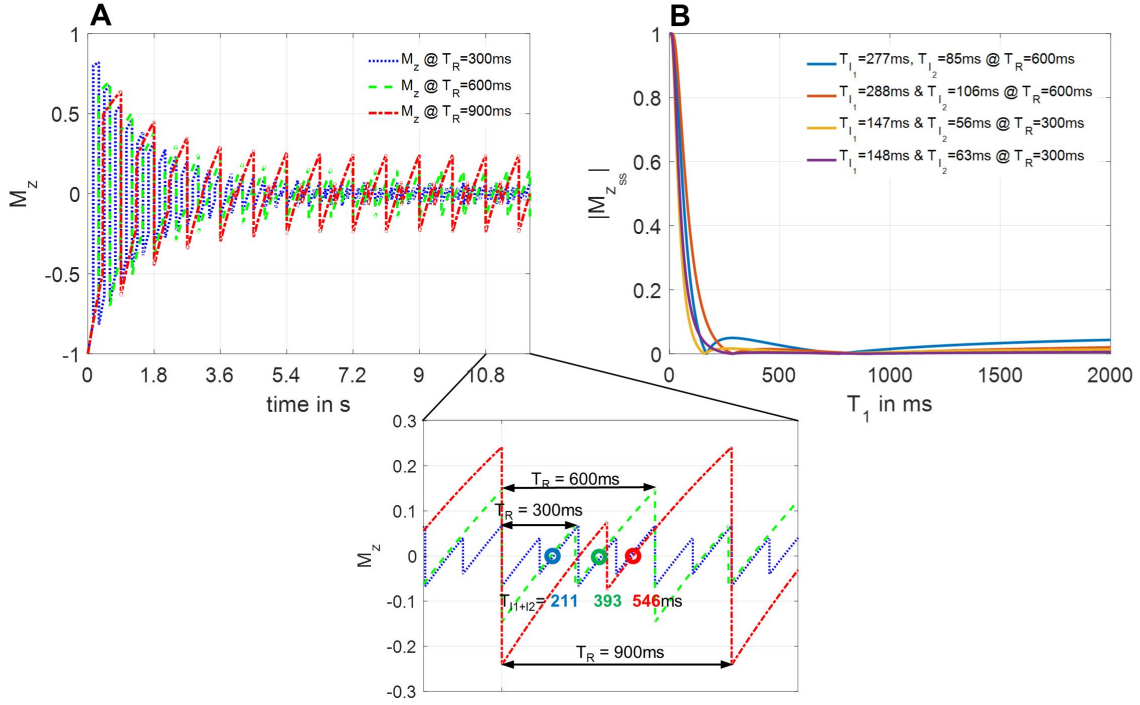
Figure 16: Simulations on the longitudinal magnetization M_z of replacing blood spins for a QIR preparation. **A** Bloch equation simulation of M_z (replacing blood spins) as a function of time for $T_R=300/600/900$ms. T_I's were obtained by minimizing Eq.(7) for a T_1 blood value range of 200 to 1400ms. T_{I_1}/T_{I_2} were as follows: 148/63ms for $T_R=300$ms; 288/106ms for $T_R=600$ms; 412/135ms for $T_R=900$ms; M_z is centered around zero magnetization at $T_{I_1} + T_{I_2}$. **B** Simulation of $M_{z_{ss}}$ by Eq.(7) for following configurations $T_R/T_{I_1}/T_{I_2}/T_{1_{range}}$: 600/277/85/100-1400ms; 600/288/106/200-1400ms; 300/147/56/100-1400ms; 300/148/63/200-1400ms; By minimizing Eq.(7) for a desired range of blood T_1 species, a special set of T_I's is obtained. Simulations are realized for tissue relaxation times @3T.

The *steady state* M_z for the replacing blood spins can be expressed by Eq.(7) [57].

$$M_{z_{ss}} = 1 - \frac{2e^{-T_{I_2}/T_{1_{blood}}}\left[1 - e^{-T_{I_1}/T_{1_{blood}}}\right]}{1 - e^{-T_R/T_{1_{blood}}}} \tag{7}$$

Figure 16B shows examples of simulations by Eq.(7) for a set of T_I and T_R. Minimizing Eq.(7) for different blood T_1 ranges (100 to 1400ms / 200 to 1400ms) results in special sets of T_I's which directly effects the extend of blood suppression over the defined T_1 range for a certain T_R. It can also be seen that including shorter T1 species causes a slight increase in blood M_z but at the same time allows suppression of shorter ones.

Figure 17A shows examples of Bloch equation simulations for $M_{xy}(T_E)$ on different static tissues and the consequent saturation effect introduced by the use of a QIR preparation module. The extend of reduction in static tissue signal (M_{xy} ratio of a QIR-GRE and GRE) depends on T_R. The shorter T_R the stronger the saturation effect which is obvious as a decrease in T_R shortens T_I and consequently the recovery time M_z for the static tissue between subsequent repetitions. Figure 17B shows phantom measurements of an implemented QIR-GRE @3T Siemens TimTrio based on the diagram shown in Figure 15. As can be seen from the images the saturation effect is more pronounced for the shorter T_R time.
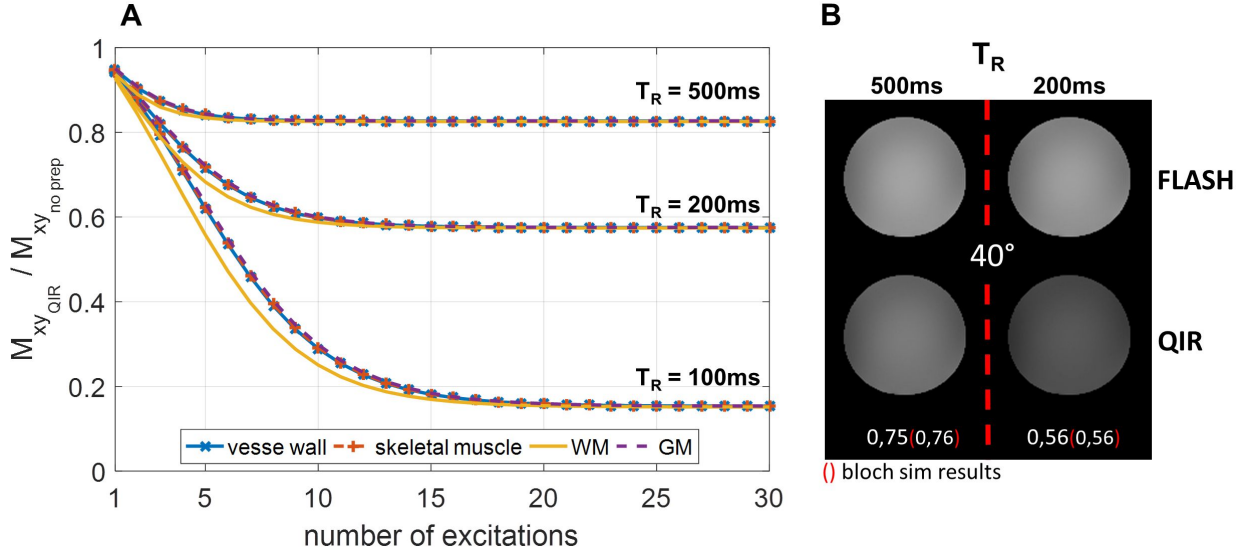
Figure 17: Simulation of the transverse magnetization M_{xy} of static tissues with and without a QIR preparation module and a GRE as host sequence. In addition, phantom measurements of an implemented QIR-GRE are shown. **A** Bloch equation simulations of static tissues for $T_R=100/200/500$ms. T_{I_1} and T_{I_2} were calculated by Eq.(7) for a blood T_1 range of 200 to 1400ms. Hence, following configurations are obtained $T_R/T_{I_1}/T_{I_2}$: $100/50/24$ms; $200/100/44$ms; $500/243/93$ms; GRE parameters are $T_E=5.3$ms, $\alpha = 40°$; DIR module time between non- and spatial-selective 180° RF pulse is 21ms; T_1/T_2 relaxation times: vessel wall = 1400/120ms; skeletal muscle = 1420/32ms; WM = 1110/56ms; GM = 1470/71ms corresponding to [58]. The ratio between M_{xy} of a QIR-GRE and GRE is plotted as a function of excitations (number of repetitions, approach to steady state). Static tissue is saturated by the QIR preparation and the extend depends on T_R. M_{xy} was taken at T_E. Simulations are realized for tissue relaxation times @3T. **B** Phantom measurements (Siemens QA phantom, $T_1=102$ms and $T_2=76$ms) of a QIR-GRE implemented @3T Siemens TimTrio VB17 based on diagram Figure 15 using a T_R of 200/500ms and T_E of 5.3ms. Saturation of static tissue is calculated as the ratio between QIR-GRE and GRE. Values are 0.56 and 0.75 for T_R 200 and 500ms. Measured data fit well with data simulated by Bloch equations as indicated in red brackets.

Figure 18 shows an example of in vivo (volunteer's common carotid artery) dark blood imaging by QIR-GRE. It can clearly be seen that the lumen signal do not contribute to the wall signal due to the suppression of inflowing blood spins. In addition, the limited coil sensitivity of the used surface coil lead to noise enhancement in the center of the image.
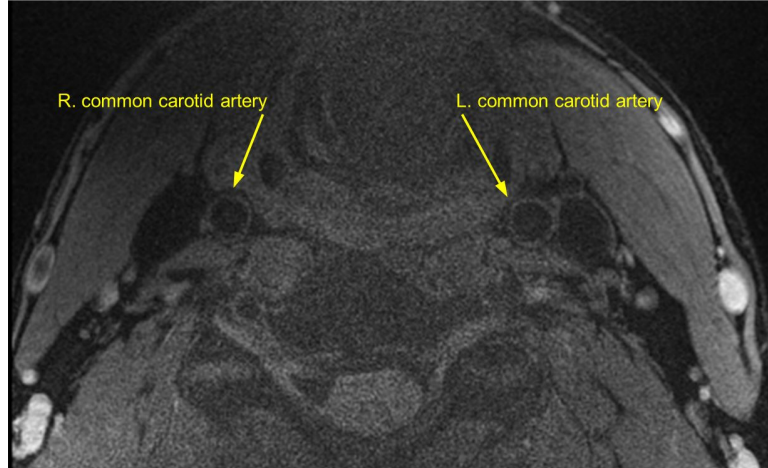
Figure 18: Dark blood imaging of the common carotid arteries *(single-slice)* of a volunteer using a 2D QIR-GRE measured @3T Siemens TimTrio and 2x4CH CPC coil. **A** 2D QIR-GRE with T_R=500ms, T_E=5.6ms, α = 60°, T_{I_1}=236ms, T_{I_2}=77ms, FOV=120x120mm^2, matrix=384x384, bandwidth=243Hz/pixel, resolution=312x312μm^2, slice thickness=3mm, NEX=1, spectral fat suppression, $\sim$4min acquisition time.

The major drawback of this technique is its single-slice nature and the more pronounced saturation of stationary tissue when compared to the DIR sequence (see Figure 12, DIR vs Figure 17, QIR: 0.9 vs 0.8 for TR=500ms; 0.8 vs 0.6 for TR=200ms; 0.6 vs 0.2 for TR=100ms). However, as the sequence was intended to be used for T_1-weighted contrast enhancement, Yarnykh et al showed that quantitative CE values are higher compared to DIR and that there is no need for post contrast blood T_1 estimation.

3.5 Cardiac gating

The combination of the above mentioned techniques (DIR, mDIR, QIR) with cardiac triggering further helps to reduce image corruption introduced by pulsatile vessel motion. A common strategy as visualized in Figure 19 is to execute the preparation module *(blue box)* before a period of fast flow and acquire data during the period of slow flow *(purple box)* [62]. In case of a DIR sequence, the time between both modules is prescribed by a specific inversion time T_I. In addition, the repetition time T_R is substituted by the heart rate and gating is usually performed using the R-wave (e.g. T_R = 1 RR interval, T_1w; T_R = 2-3 RR, T_2w). This configuration enables replacement of noninverted blood

during maximal through plane flow (*blood flow curve*, Figure 19) and data acquisition at the time of minimal vessel motion (*blood pressure curve*, Figure 19) i.e. constant wall geometry is preserved as the distensibility of the vessels causes a change in lumen area. End-systolic and end-diastolic distensibility measurements of healthy human carotids revealed a change in lumen area up to a value of 10% indicating the importance for minimizing pulsatile motion [63].
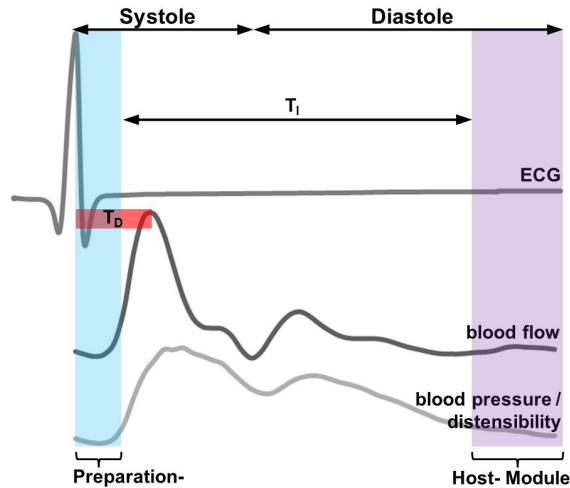
Figure 19: Dark blood signal acquisition with cardiac triggering. R-wave of the ECG, blood flow and blood pressure curves are shown from top to bottom. In addition *blue* and *purple box* represent the localization of the preparation (IR, DIR, QIR) and host module (SE, TSE, GRE) in the cardiac phase separated by inversion time T_I. In addition, the *red box* represents the trigger delay T_D for timing acquisition and maximum through plane blood flow in carotid arteries.

Dark blood imaging with gradient-recalled echo (GRE) pulse sequences without any preparation is challenging but possible using cardiac triggering. In principle, these type of sequences are fast imaging techniques, lack the 180° RF refocusing pulse but instead use the frequency-encoding gradient to rephase the GRE echo and allow for shorter echo-times compared to spin echo based sequences [64]. The replacement of excited flowing spins from the imaging slice can be achieved by adjusting an appropriate delay window (*red box*, Figure 19) between the detected R-wave and the time of maximal through plane flow. As can be seen from Figure 19, this is realized by tuning the trigger delay T_D which is used to acquire data at different cardiac phases. As the prerequisite for this technique is a fast blood flow the method works best for the measurement of proximal blood vessels (e.g. carotid arteries).

33

Figure 20A-C shows examples of different dark blood imaging strategies (2D DIR-GRE with T_R=2RR and T_I, 2D GRE and 3D GRE with T_R=1RR and T_D, Top to Bottom) of the mouse brachiocephalic artery (ApoE-/- mouse model to study atherosclerosis) using cardiac gating and a GRE sequence. For the 2D DIR-GRE the preparation module is played with the first trigger and data acquisition starts with the next trigger after T_I. It can be seen for all three cases that the magnetization of the arterial lumen is canceled and does not contribute to the wall signal. Especially for the DIR sequence also the lumen signal of the slow flowing venous blood is nulled due to the extended time to leave the imaging slice. In contrast, the contribution of the venous signal gradually increases from imaging a thin slice in a 2D and a slab in a 3D GRE.
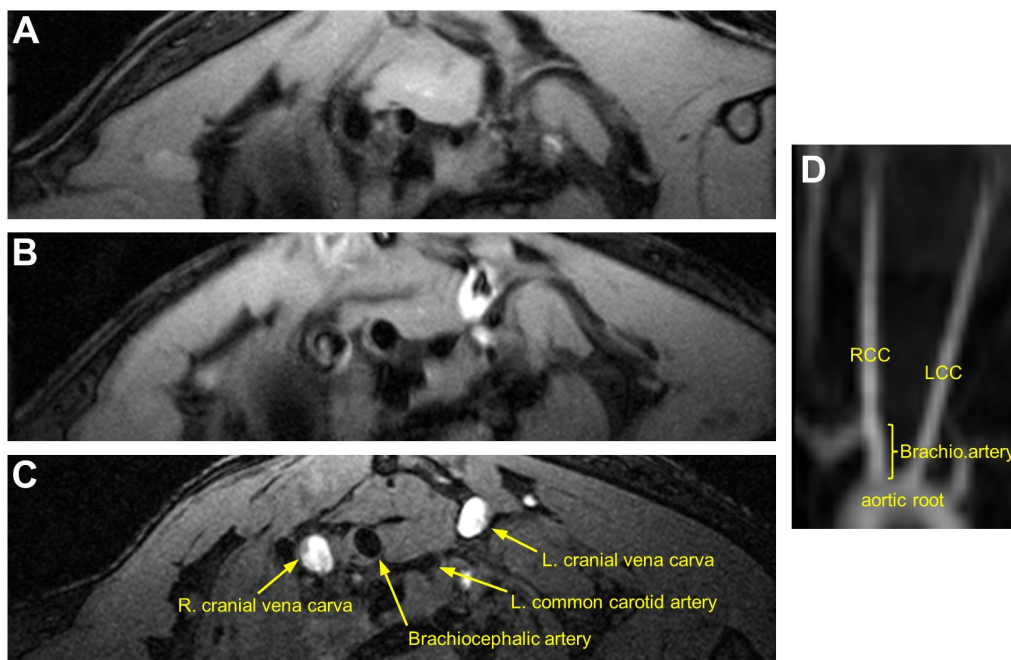
Figure 20: Dark blood imaging strategies of the mouse brachiocephalic artery (ApoE-/- mouse model to study atherosclerosis) using cardiac gating and a GRE sequence measured @7T Bruker Biospec 70/20 and 20mm surface coil. **A** 2D DIR-GRE with T_R=2RR ($\sim$280ms), T_I $\sim$135ms *(second trigger)*, T_E=3.5ms, $\alpha = 50°$, FOV=20x20mm^2, matrix=384x384, resolution=52x52μm^2, slice thickness=700μm, NEX=16, spectral fat suppression, 30min acquisition time; **B** 2D GRE with T_D=10ms, T_R=1RR, T_E=3.5ms, $\alpha = 50°$, FOV=20x20mm^2, matrix=384x384, resolution=52x52μm^2, slice thickness=700μm, NEX=16, spectral fat suppression, 15min acquisition time; **C** 3D GRE with T_D=10ms, T_R=1RR, T_E=3.5ms, $\alpha = 50°$, FOV=20x20x2mm^3, matrix=384x384x10, resolution=52x52x200μm^3, NEX=6, spectral fat suppression, 40min acquisition time; **D** 3D time of flight (TOF) maximum intensity projection (MIP) of the aortic arch, left and right common carotid arteries.

3.6 Inner volume imaging / local-look technique / zoom imaging

Inner volume imaging also referred to as local-look is a (turbo)-spin-echo based technique with limited FOV in the phase-encoding direction [65]. Instead of coplanar slice-selection-gradients for the spatially selective 90° excitation and 180° refocusing pulse the lobes are played on orthogonal axes. Because only spins of intersecting regions experience both RF pulses and hence contribute to the final signal no foldover artifacts will be introduced from object areas exceeding (surrounding) the subsectional region. Advantages arising out of this technique are the elimination of image corruption by moving tissues (respiration) and scan time reduction. The two-dimensional single slice nature of the sequence can be extended by a secondary phase-encoding gradient played on the slice-selection refocusing axis (slab) to reconstruct three-dimensional volumes. The extension in the section-selection direction compensates for the sacrificed signal to noise ratio (SNR) caused by the reduced phase FOV in the 2D version and stretches the anatomical (vessel wall) coverage but at the expense of the before mentioned saved imaging time. An application of this 3D technique was found in an cardiac gated measurement of the distensibility and wall area of human healthy carotid arteries [63]. In detail, a double inversion preparation module to null flowing spins followed by the 3D volume selective TSE sequence revealed a good wall SNR agreement to the conventional single slice dark blood 2D cross sectional image recorded over the same acquisition time. The advantage of enlarged vessel coverage in conjunction with no prolonged imaging time and interfering respiration artifacts makes this technique a well suited tool to analyze atherosclerotic wall alterations.

3.7 Multispectral MRI and techniques beyond

Multispectral MRI: 3DTOF, T1w, T2w, PDw
The afore mentioned techniques (spatial presaturation, DIR, mDIR, QIR, cardiac gating etc.) are used to null the signal of flowing spins, minimize image corruption, shorten acquisition time while improving the appearance of the vessel wall. These methods combined with different weightings (T1w, T2w, PDw) and TOF allow atherosclerotic plaque tissues to be identified and characterized and finally an estimation of the degree of lesion vulnerability. Three-dimensional time of flight (3DTOF) is a bright blood angiographic technique which commonly uses a gradient-recalled echo pulse sequence and

is based on the so called flow-related enhancement (FRE) [66, 53]. Blood spins entering the imaging slice are enhanced (inflow enhancement) compared to the stationary background tissue to produce an increased vessel signal. One limitation is the gradual saturation of inflowing blood as it travels through the imaging slab and experiences multiple RF excitation pulses depending on blood velocity and slab thickness. The result is a strong enhancement of blood signal at the entry slice and an attenuation of the blood spins at the exit slice. This drawback is compensated by using multiple overlapping thin-slab acquisition (MOTSA) and tilted optimized nonsaturating excitation (TONE) pulses [67, 68]. The flip angle produced by this pulse (spatially asymmetric RF pulse) increases with distance in the direction of blood flow and therefore equalizes the signal of flowing blood through the imaging slab. Moreover, instead of using one thick imaging slab, multiple thin slabs of a few centimeter are imaged sequentially and combined to one large volume to reduce the number of excitations of flowing spins. Beside the ability of the sequence to gather information on the degree of luminal narrowing it was shown that it can also be used to classify the integrity of the fibrous cap (intact thick vs intact thin vs ruptured cap) in atherosclerotic human carotids in vivo [69, 70]. In general, the fibrous cap appears as a dark band near to the white lumen and intact thick, thin or ruptured cap was categorized as uniform visible, not visible or disrupted, respectively. Discrimination from calcification was based on inspections of additional multicontrast weightings (T1w, T2w, PDw) as the fibrous cap is a hypointense band exclusively on TOF weighting whereas calcification appears dark on all weightings. In addition, comparison of fibrous cap appearance between histology and MRI revealed a high level of agreement and association of fibrous cap rupture with transient ischemic attack (TIA) and stroke. Moreover, the high accuracy of a multicontrast protocol (T1w, T2w, PDw and 3DTOF) was shown for classifying the integrity of the fibrous cap (stable: thick vs unstable: thin, ruptured, ulcerated) when compared to the gold standard histology [71]. In the nineties Toussaint et al was one of the first demonstrating the capability of in vivo MRI to differentiate human plaque components of carotid arteries like lipid core, fibrous cap, calcification, intraplaque hemorrhage, thrombosis, normal media and adventitia [72]. A good agreement of quantitative in vivo and ex vivo plaque / normal wall T2 values was found. They showed that a T2w sequence can be used to discriminate the lipid rich core (low signal) from fibrous cap and media (high signal) which are surrounded by a thin black band (adventitia) in vivo. Moreover, calcification characterized as signal voids on T2w and T1w sequences could also be detected and classified in vivo. Fresh thrombus on a T2w sequence appeared as high signal intensity area at the side of

occlusion and showed lower signal intensity values in the superficial layers. For intraplaque hemorrhage, characterized as a low intensity region, shorter T2 values compared to the lipid core were reported. However, the signal behaviour of a hemorrhage is more complex as the signal intensity depends on the age of the hematoma and type of MR weighting (T1w or T2w) [73]. Bradley et al outlined the stages that hemoglobin passes with age (from oxy-,deoxy-, methemoglobin to reversible hemichromes or breakdown to ferritin and hemosiderin) and described the resulting MR signal appearance. They defined five distinct stages ($< 24h$ to $> 14d$) of hemorrhage including hyperacute, acute, early subacute, late subacute and chronic phase all affecting the final MR appearance of that tissue. For example, during the late subacute phase ($age > 7days$) the signal intensity is high for both weightings due to the paramagnetic properties of methemoglobin and its reduced susceptibility effect in its extracellular state (decompartmentalization). During the early subacute phase ($age > 3d$) methemoglobin is intracellular and leads to a shortening of T1 and T2 and therefore to a high signal on T1w and low signal on T2w sequences (T2 effect is even stronger for gradient echo images). The ability to detect intraplaque hemorrhage of carotid arteries in vivo with a high interobserver agreement was shown by using T1w TSE and TFE (TurboFlash) sequences [74]. The agreement for the TFE sequence was higher and misinterpreted regions belonged to fibrous tissue outside the main plaque area. The ability to study aortic plaque morphology and composition in vivo using a multispectral MR protocol was shown by Fayad et al [75]. Morphological parameters like plaque thickness and extent as well as compositional features (IV/Va: fibrolipid-, Vb: calcified-, Vc: fibrotic-, VI: thrombotic type) classified based on the American Heart Association (AHA) criteria (used types: IV to VI) revealed strong agreements between MRI and transesophageal echocardiography (TEE). Moreover, Yuan and colleagues used the multispectral approach to identify lipid rich necrotic cores and intraplaque hemorrhage of carotid arteries in vivo and comparison to gold standard histology showed a high overall accuracy [76]. Beside the in vivo work, carotid endarterectomy specimens were used to characterize plaque components ex vivo using multiple sequence weightings and to analyze the diagnostic accuracy when compared to histological findings [77]. A set of endarterectomy samples was used to generate MRI criteria (based on published criteria) for plaque tissues and finally a high accuracy was found for lipid core, calcification and fibrocellular tissue while thrombus was lowest in sensitivity when cross tabulated to histology. They also showed the ability of a algorithm in combination with parametric MR images (T1, T2, diffusion coefficient, proton density image) to semiautomatically detect and segment plaque tissues. A similar approach was

implemented by Clarke and co-workers using a supervised classification algorithm and eight contrast weightings to identify and segment plaque components [78]. The classifier showed high sensitivity and specificity values for different plaque tissues when compared to matched histological images. As previously mentioned, AHA criteria which act as a *histological template* are used to classify an atherosclerotic plaque (Type I to VIII). Cai et al modified the conventional criteria as some of the lesion types has not been proofed to be distinguishable by MRI because of the limited resolution in vivo [79]. Carotid atherosclerotic plaques were measured in vivo using multicontrast weightings and showed good agreement when compared to the histological findings which further indicates the capabilities of MRI to differentiate between early, intermediate and advanced atherosclerotic plaque lesions. Another evaluation study performed by Saam and co-workers points the multicontrast approach to be reproducible and excellent to differentiate between plaque tissue components [80]. In addition to the multispectral approach, signal alterations induced by the administration of a non-specific gadolinium chelate lead to an improved discrimination between plaque tissues [52]. Wasserman et al used a T1w DIR-TSE sequence and gadolinium enhancement to differentiate fibrous cap from lipid core plaque tissue with a CNR and SNR comparable and higher than that with T2w images, respectively. Beside the mentioned studies, numerous in vivo and ex vivo trials can be found in the literature all investing the accuracy of plaque characterization by MRI [62, 81, 82, 83, 84]. All these investigations taken together show that morphological as well as compositional plaque features can be detected and classified by MRI with high accuracy and that this method my be useful to investigate aortic atherosclerosis in vivo as well as to study therapeutical interventions and plaque progression and regression. Table 1 summarizes MRI signal intensity criteria to classify atherosclerotic plaque constituents by a multicontrast approach and gadolinium enhancement and is adopted from [77, 69, 85, 76, 80, 86, 87, 17, 88].

Table 1: Atherosclerotic plaque tissue signal intensities with multicontrast approach

Plaque tissue	T1w	T2w	PDw	TOF	CA
Fibrous cap	i/H	i/H	i/H	h	u
LRNC	H	h	i/H	-	nu
Calcification	h	h	h	-	nu
IPH	v/H	v	i/H	-	nu

LRNC, lipid rich necrotic core; IPH, intraplaque hemorrhage; TOF, time of flight; CA, contrast agent; h=hypointense, H=hyperintense, i=isointense, v=variable; (n)u= (no)CA update; all plaque tissue signal intensities are relative to adjacent muscle tissue. Investigations analyzing or summarizing plaque tissue signal appearance see Ref. [77, 69, 85, 76, 80, 86, 87, 17, 88].

Techniques beyond:

Beside the use of multispectral weightings their are also efforts to have all-in-one sequences for identifying multiple atherosclerotic plaque components in one shot or to have specific sequence implementations for improved detection of a certain plaque tissue (e.g. intraplaque hemorrhage). Saam and colleagues showed that the complexity of an atherosclerotic plaque rather than the degree of luminal narrowing is thought to be a valuable predictor of lesion vulnerability [27]. They analyzed the prevalence of AHA lesion type VI (complex plaque with possible surface defect, hemorrhage, thrombus) in carotid arteries by multicontrast MRI and found this type frequently in arteries with a low degree of stenosis ($< 50\%$). Hemorrhage was detected in more than 80% of the type VI lesions and fibrous cap rupture in about half of them. Therefore, hemorrhage is an important plaque feature in atherosclerosis progression and destabilization and of special interest in sequence development. Wang et al proposed a 3D slab-selective phase-sensitive inversion-recovery (**SPI**) sequence for improved detection of intraplaque hemorrhage [89]. The sequence is a modification of the magnetization-prepared 3D rapid acquisition gradient echo (MP-RAGE) sequence which shows poor hemorrhage-wall contrast and insufficient blood suppression. The SPI sequence consists of a extra TFE module for phase correction but at the expense of a doubled IRTR time. The inversion time is optimized to maximize the distance between wall, hemorrhage and the signal of flowing spins. The paramagnetic properties of methemoglobin in combination with the phase-sensitive reconstruction of the proposed T1w sequence maximizes the CNR between wall, hemorrhage and lumen and improves accuracy of hemorrhage identification when compared to the standard T1w MP-RAGE. DIR or QIR dark blood preparation

modules are used to null the spins of flowing blood to improve image quality and delineation of wall architecture but suppression remains challenging at regions of complex flow (carotid bulb). Wang et al proposed a method for improved suppression of plaque-mimicking artifacts in the carotid bifurcation using an (improved) motion-sensitized driven-equilibrium **(i)MSDE** turbo spin echo (**TSE**) sequence [90, 91]. Comparison to inflow saturation, DIR and multislice DIR revealed superior CNR (between adjacent muscle and lumen) and lumen SNR values for the (i)MSDE implementation. Moreover, wall area and thickness measurements showed slightly but significant lower values due to the improved delineation of lumen-wall boundaries. An interesting candidate using driven-equilibrium as a black-blood preparation module with intrinsic T1 and T2 weighting properties is the three-dimensional MSDE rapid black-blood gradient echo sequence (**3D-MERGE**) proposed by Balu and co-workers [92, 93]. The sequence allows the acquisition of the entire cervical carotid artery at high isotropic resolution within two minutes while preserving good blood nulling properties as well as accurate plaque morphology measurements when compared to existing MRI approaches. This technique is advantageous as 2D black-blood protocols are time consuming especially when covering a large anatomical location. In addition, the feasibility of that implementation alone to classify plaque components like calcification, lipid rich necrotic core was evaluated against a well validated multicontrast protocol [94]. Moreover, the intrinsic T1 and T2 contrast tuned by shot and MSDE duration allows the detection of short T1 species like hemorrhage and the opportunity to image long T2 components like loose extracellular matrix in one shot [93]. Along with the black-blood imaging it simultaneously provides angiographic information. Another candidate providing black and bright-blood contrast and specifically directed to intraplaque hemorrhage detection is the simultaneous non-contrast angiography and intraplaque hemorrhage (**SNAP**) sequence proposed by Wang and colleagues [95]. The sequence design is based on the SPI technique consisting of two TFE modules one for image acquisition and the second for phase correction. However, the SNAP technique uses a smaller flip angle to acquire the reference image for background phase estimation and to accurate reconstruct phase sensitive images. It provides a so called SNAP'-' image for lumen imaging (bright angiographic signal like in TOF) and a SNAP'+' image for hemorrhage detection just by displaying either the negative or the positive signals. The sequence is again optimized to provide the best contrast between hemorrhage, wall and the lumen component as was done for the SPI implementation. A comparison to TOF and MP-RAGE indicates strong correlation for lumen size measurements and high accuracy for hemorrhage detection, respectively.

Another interesting approach for rapid isotropic imaging beside 3D-MERGE is the delay alternating with nutation for tailored excitation (**DANTE**) black-blood prepared **3D FLASH** sequence proposed by Xie et al [96]. It was developed for imaging peripheral artery disease (PAD) aimed at covering a large anatomical location for fast evaluation (4min acquisition time) of vessel wall morphology. The overall goal was to maximize the CNR of wall-lumen boundaries and for that parameters of the DANTE preparation (RF pulse flip angle, pulse train length) and FLASH readout (flip angle, turbo factor) had to be optimized to efficiently null the signal of flowing spins as both modules are affecting the final wall-lumen contrast. A comparison of morphological parameters (wall area and thickness, lumen area, luminal stenosis) as well as wall SNR and wall-lumen CNR measurements showed excellent agreement to a conventional 2D DB-TSE and MRA sequence. Fan and co-workers proposed the multicontrast atherosclerosis characterization (**MATCH**) sequence for carotid plaque imaging with a single interleaved five minute scan [97]. It consists of a 3D spoiled segmented FLASH readout to provide three different contrast weightings (1st: hyper T1w; 2nd: gray blood and 3rd: T2w) for the characterization of intraplaque hemorrhage (hyperintense at 1st weighting), calcification (hypointense at 2nd), lipid rich necrotic core (hypointense at 3rd and isointense at 1st) and loose-matrix (hyperintense at 3rd and isointense at 1st). Flow-sensitive dephasing (FSD) black-blood preparation is used to null the signal of flowing spins on the 1st and 3rd weighting. In detail, the 1st weighting focus on hemorrhage identification, the 2nd provides a gray contrast to highlight dark calcification and the 3rd is used to characterize loose-matrix, lipid rich necrotic core and to differentiate acute from recent hemorrhage. Comparison to a conventional multispectral protocol showed good agreement for component detection and significant higher contrast to signal ratios ($[S_1 - S_2]/S_2$) for hemorrhage and calcification. Another candidate for imaging the carotid arterial wall is the 3D variable-flip-angle turbo spin-echo (SPACE) sequence which provides inherent black-blood contrast due to the long echo train but may exhibit plaque mimicking artifacts at regions of complex flow like carotid bifurcation. To counteract that, Fan and colleagues proposed a **FSD** black-blood prepared **SPACE** to improve suppression of flowing spins [98]. Wall-lumen CNR and morphological parameters (lumen and wall area) measured at locations with residual blood signal on SPACE images were compared to the FSD prepared version. Improved CNR values and larger lumen area values were found for the latter one whereas CNR for other regions not showing plaque-mimicking artifacts was slightly reduced. The superiority of the FSD-SPACE to a 2D T2w TSE with spatial saturation bands regarding higher spatial resolution (in z-direction), shor-

ter imaging time and larger anatomical coverage was also demonstrated but wall and lumen area measurements showed good agreement. However, it has to be kept in mind that the motion sensitizing FSD preparation as well as motion-related artifacts introduced by body movement, breathing or swallowing are able to compromise the entire 3D dataset. Beside these candidates susceptibility-weighted imaging (SWI), magnetization transfer (MT) as well as diffusion weighted imaging (DWI) are under investigation for plaque component detection. As outlined in *Chapter 4* special **DWI** sequences are proposed (DP-TSE, ss-IMIV-DWEPI) for identifying wall and plaque features like lipid rich necrotic core, fibrous tissue, hemorrhage, less diseased wall, normal wall based on the calculated apparent diffusion coefficient (ADC) in z-direction. Yang et al proposed **SWI** for identifying calcification and morphological parameters (size and position) of that plaque feature correlated well between MRI and CT [99]. The magnitude image allows for differentiation between the lumen-wall boundary while the phase image depicts calcification within the vessel wall as a bright spot. **MT** was tested on carotid endarterectomy specimens and analyzed for its ability to characterize plaque components based on its specific magnetization transfer ratio (MTR) when correlated with histology [100]. Qiao and co-workers showed that after appropriate MT calibration (saturation pulse: offset=10kHz; amplitude=670Hz and duration=10ms) specific MTR's can be obtained for plaque tissues like collagen (type I, III), intraplaque hemorrhage (fresh, recent, old), calcification and lipids. Plaque features with high protein density (collagen type I, lipids) showed higher MTR compared to components with low protein density like calcification or collagen type III. Unique values were found for the three hemorrhage phases due to protein density differences and the resulting effect on MT. Especially information gained from hemorrhage may help to further characterize its role in plaque progression and destabilization.

Assessing plaque morphology and composition by the use of a two-dimensional multi-contrast protocols are getting replaced by (fast) three-dimensional isotropic *all-in-one* protocols to compensate for limited resolution (in slice direction), partial volume effects, spatial coverage, image misregistration and long scan times [101]. Zhou and colleagues evaluated a three-dimensional multispectral vessel wall (coverage of intra and extra-cranial vessels) protocol (MERGE, SNAP etc) and found good image quality, blood suppression as well as wall and lumen SNR, wall-lumen CNR parameters for each sequence and vessel wall locations. Table 2 lists the above described three-dimensional black-blood imaging techniques together with selected sequence parameters.

Table 2: Three-dimensional black-blood imaging techniques and selected sequence parameters

Sequence name	Spatial resolution	FOV	Acquisition time	Orientation	Ref.
FSD-SPACE	$0.63mm^3$ isotropic	$160x116x50mm^3$	6.40min	coronal	[98]
MATCH	$0.55x0.55x2mm^3$	$140x140x32mm^3$	4.75min	axial	[97]
DANTE-FLASH	$0.72mm^3$ isotropic	300mm l.c.	3.50min	coronal	[96]
SNAP	$0.80mm^3$ isotropic	$160x32x160mm^3$	5.30min	coronal	[95]
SPI	$0.60x0.60x2mm^3$	$160x160x32mm^3$	3.00min	axial	[89]
MERGE	$0.70mm^3$ isotropic	$250x160x70mm^3$	2.00min	coronal	[92]

FOV, field of view; l.c., longitudinal coverage; FSD-SPACE, flow-sensitive dephasing black-blood prepared variable-flip-angle turbo spin-echo sequence; MATCH, multicontrast atherosclerosis characterization sequence; DANTE-FLASH, delay alternating with nutation for tailored excitation black-blood prepared fast low angle shot sequence; SNAP, simultaneous noncontrast angiography and intraplaque hemorrhage sequence; SPI, slab-selective phase-sensitive inversion-recovery sequence; MERGE, three-dimensional MSDE rapid black-blood gradient echo sequence; MSDE, motion sensitized driven equilibrium.

4 Measurement of vessel wall diffusion anisotropy

4.1 Introduction

Magnetic resonance diffusion weighted imaging (MR-DWI) allows to measure the self-diffusion of water molecules in their microenvironment [102]. This is possible by sensitizing a MRI sequence to the microscopic motion of water molecules. A well-known implementation is the pulsed gradient technique introduced in the sixties by Stejskal-Tanner [103]. The 180° refocusing RF pulse of the spin-echo module is surrounded by two diffusion-encoding gradients and the resulting diffusion weighting factor (b-value) is expressed by $b = \gamma^2\delta^2 G^2(\Delta - \delta/3)$, where δ is the duration of the gradient pulses, Δ the gradient separation time, γ the gyromagnetic ratio and G the gradient strength. The degree of signal attenuation depends on the magnitude of displacement of water molecules along the applied gradient direction and is given by $S(b) = S_0 e^{-bD}$. The weighting of signal attenuation by diffusion S(b) is therefore prescribed by the selected b-value in units of s/mm^2 and the diffusion coefficient (D in mm^2/s) which is a measure of water mobility in their microenvironment. S_0 is the reference signal without diffusion weighting (no diffusion-encoding gradients). The repetition of such an experiment for N diffusion directions ($N \geq 6$) allows to calculate the direction of the principle contribution of diffusion and is called diffusion tensor imaging (DTI). This approach allows to visualize directed diffusion (anisotropic diffusion) of water molecules for instance along a fiber which is the case in white matter structures or muscles [104, 105]. The diffusion tensor $\mathbf{D}$ is given by a 3x3 matrix or 2x2 matrix for the 2D case. Mathematical aspects of the 3D tensor are described in the following and is in detail discussed by Kingsley et al. [106, 107, 108]. The signal attenuation (S_k) is dependent on the direction of the applied diffusion-encoding gradients ($\mathbf{g}$, normalized gradient components) and is given by Eq.(8).

$$S_k = S_0 e^{-b\mathbf{g_k^T}\mathbf{D}\mathbf{g_k}} \tag{8}$$

The exponent of the diffusion weighted signal S_k can be rewritten as:

$$bg_{\mathbf{k}}^{\mathbf{T}}\mathbf{D}g_{\mathbf{k}} = b \begin{bmatrix} g_{xk} & g_{yk} & g_{zk} \end{bmatrix} \begin{bmatrix} D_{xx} & D_{xy} & D_{xz} \\ D_{yx} & D_{yy} & D_{yz} \\ D_{zx} & D_{zy} & D_{zz} \end{bmatrix} \begin{bmatrix} g_{xk} \\ g_{yk} \\ g_{zk} \end{bmatrix} \tag{9}$$

Expansion of Eq.(9) results in Eq.(10):

$$b \left(g_{xk}^2 D_{xx} + g_{yk}^2 D_{yy} + g_{zk}^2 D_{zz} + 2g_{xk}g_{yk}D_{xy} + 2g_{xk}g_{zk}D_{xz} + 2g_{yk}g_{zk}D_{yz} \right) \tag{10}$$

Hence, Eq.(8) can be rewritten as Eq.(11) which is also known as the B-matrix formalism which accounts for attenuation effects of all gradients (also imaging gradients):

$$S_k = S_0 e^{-\sum\limits_{i=1}^{3}\sum\limits_{j=1}^{3} b_{ij}D_{ij}} \quad \text{i,j=x,y,z} \quad \text{k=1...N diffusion experiments} \tag{11}$$

The diffusion tensor $\mathbf{D}$ is evaluated by solving Eq.(12)

$$\mathbf{x} = \mathbf{B}\alpha \tag{12}$$

in a linear least-squares sense with the solution:

$$\alpha = (\mathbf{B^T B})^{-1}\mathbf{B^T x} \tag{13}$$

The six tensor elements of $\mathbf{D}$ and the logarithm of the b=0 signal intensity are expressed as a seven-element column vector α and is given by Eq.(14)

$$\alpha = \begin{bmatrix} D_{xx} & D_{yy} & D_{zz} & D_{xy} & D_{xz} & D_{yz} & ln(S_0) \end{bmatrix}^T \quad , \tag{14}$$

the $\mathbf{B}$ matrix (Nx7 matrix) is expressed by Eq.(15)

$$\mathbf{B} = \begin{pmatrix} -b_{xx1} & -b_{yy1} & -b_{zz1} & -2b_{xy1} & -2b_{xz1} & -2b_{yz1} & 1 \\ \vdots & \vdots & \vdots & \vdots & \vdots & \vdots & \vdots \\ -b_{xxN} & -b_{yyN} & -b_{zzN} & -2b_{xyN} & -2b_{xzN} & -2b_{yzN} & 1 \end{pmatrix} \quad , \tag{15}$$

and the diffusion weighted signal S_k is rewritten as

$$\mathbf{x} = \begin{pmatrix} ln(S_1) \\ \vdots \\ ln(S_N) \end{pmatrix} \quad . \tag{16}$$

From column vector α corresponding eigenvalues (λ) and eigenvectors (ϵ) can be calculated by using eigenvalue decomposition. In case of multiple diffusion directions but one diffusion weighting factor an alternative approach can be used to evaluate the diffusion tensor by solving

$$\mathbf{Y} = \mathbf{Hd} \tag{17}$$

in a linear least-square sense with the solution:

$$\mathbf{d} = (\mathbf{H^T H})^{-1} \mathbf{H^T Y} \quad , \tag{18}$$

where $\mathbf{Y}$ represents the calculated diffusion coefficients for the N diffusion directions

$$\mathbf{Y} = \begin{pmatrix} ln(S_0/S_1)/b \\ \vdots \\ ln(S_0/S_N)/b \end{pmatrix} \quad , \tag{19}$$

$\mathbf{H}$ the Nx6 matrix normalized gradient components

$$\mathbf{H} = \begin{pmatrix} g_{x1}^2 & g_{y1}^2 & g_{z1}^2 & 2g_{x1}g_{y1} & 2g_{x1}g_{z1} & 2g_{y1}g_{z1} \\ \vdots & \vdots & \vdots & \vdots & \vdots & \vdots \\ g_{xN}^2 & g_{yN}^2 & g_{zN}^2 & 2g_{xN}g_{yN} & 2g_{xN}g_{zN} & 2g_{yN}g_{zN} \end{pmatrix} \quad , \tag{20}$$

and $\mathbf{d}$ is the tensor given as a six-element column vector

$$\mathbf{d} = \begin{bmatrix} D_{xx} & D_{yy} & D_{zz} & D_{xy} & D_{xz} & D_{yz} \end{bmatrix}^T \quad . \tag{21}$$

From the calculated tensor measures like fractional anisotropy (FA), mean- (MD), axial- (AD), radial diffusivity (RD) or anisotropy coefficients (CL, linear; CP, planar; CS, spherical) can be extracted [109]. Moreover, tractography links voxels with similar eigenvectors to reconstruct orientations of fiber pathways [110]. MR-DWI has also shown great potentials to discriminate between healthy and pathological vessel tissue by evaluating the apparent diffusion coefficient (ADC) along the z-axis of carotid vessel wall segments [111, 112, 113, 114]. A comparison of literature values highlight ADCs for healthy vessel wall tissue ranging from 1.3e-3 to 1.6e-3 mm^2/s, for plaque components like lipid rich necrotic core (LRNC) from 0.4e-3 to 0.75e-3 mm^2/s or for plaque tissue in general from 0.3e-3 to 0.9e-3 mm^2/s. These measurements were done on healthy volunteers and patients. Table 3 summarizes in detail found literature ADC values for intact vessel wall and atherosclerotic plaque components.

Table 3: Comparison of ADC literature values of intact vessel wall and atherosclerotic plaque components

Normal wall	Less diseased wall	Plaque	LRNC	Hemorrhage	Fibrous tissue	Ref.
1.28±0.009		0.29-0.87				[111]
1.27±0.160			0.38±0.10	0.98±0.25		[113]
1.53±0.230			0.60±0.16		1.27±0.29	[114]
			0.73±0.23		1.04±0.30	[112]
	0.48	0.29				[115]
x1e-3	x1e-3	x1e-3	x1e-3	x1e-3	x1e-3	

LRNC, lipid rich necrotic core. Data are reported as x̄±σ.

In the following chapter, parts of the paper published in the *Journal of Cardiovascular Magnetic resonance* entitled *In vivo cardiovascular magnetic resonance of 2D vessel wall diffusion anisotropy in carotid arteries* are presented and reprinted [116].

4.2 An in vivo human study: In vivo cardiovascular magnetic resonance of 2D vessel wall diffusion anisotropy in carotid arteries

Introduction:
As outlined in the former section, pathological wall transformations can be studied by

quantification of the ADC along the longitudinal axis of the artery as diffusion is affected by plaque constituents. However, ADC depends on subject's orientation in the scanner reference frame, therefore possible errors like scan-rescan variations or confound comparisons between subjects may be introduced. Recent ex vivo DWI studies on swine arteries aimed to investigate the fibrous structure (collagen orientation) of vessel walls by diffusion tensor imaging [117, 118]. The data revealed a circumferential fiber orientation rather than an organization in z-direction, suggesting a principle diffusion direction aligned perpendicular to the slice direction. Arterial vessels are made up of multiple layers (intima, media, adventitia), concentric organized elastic laminae (medial, internal) and collagen fibers, properties best suitable to image diffusion anisotropy by DTI [119]. Limiting factors accessing diffusion metrics in vivo are the low spatial resolution and increasing scan time for sufficient diffusion directions when conventional single-shot EPI (ss-EPI) sequences are used. In addition, they suffer from T_2^* blurring and susceptibility artifacts due to the extended time required to fill the k-space. Therefore, studying the unique architecture of vessels and investigating diffusion anisotropy by DTI in vivo has never been done so far. Our proposed approach overcomes these limitations by measuring tangential and radial diffusion evaluated from a 2D diffusion tensor. High spatial resolution and sufficient SNR is achieved by using a read-out segmented EPI (rs-EPI, syngo RESOLVE, Siemens) pulse sequence [120]. In combination with a novel gradient direction scheme (18 diffusion gradient directions oriented on a hemicycle within a plane perpendicular to the z-axis of the carotid artery) the measurement time is reduced to a clinical acceptable range. In this proof of concept we demonstrated the feasibility of measuring diffusion in the vessel wall of carotid arteries in vivo in a non-destructive and non-invasive fashion and provide initial results from twelve healthy male volunteers.

Methods:

Two-dimensional diffusion acquisition scheme:

The basic idea to reduce the amount of diffusion sensitizing gradients is the reduction of a three-dimensional diffusion measurement to a two-dimensional diffusion measurement perpendicular to the artery's axis (Figure 21). This strategy is justified by the work from Flamini et al revealing a tangential fiber orientation that indicates the principle direction of diffusion [118]. Given the fact that diffusion in z-axis is low compared to tangential and radial diffusion, this simplification provides the basis for in vivo measurements due to the significant reduction of diffusion sensitizing gradients needed for DTI. To demonstrate

the validity of our approach 3D and 2D diffusion measurements on a porcine aorta were performed.
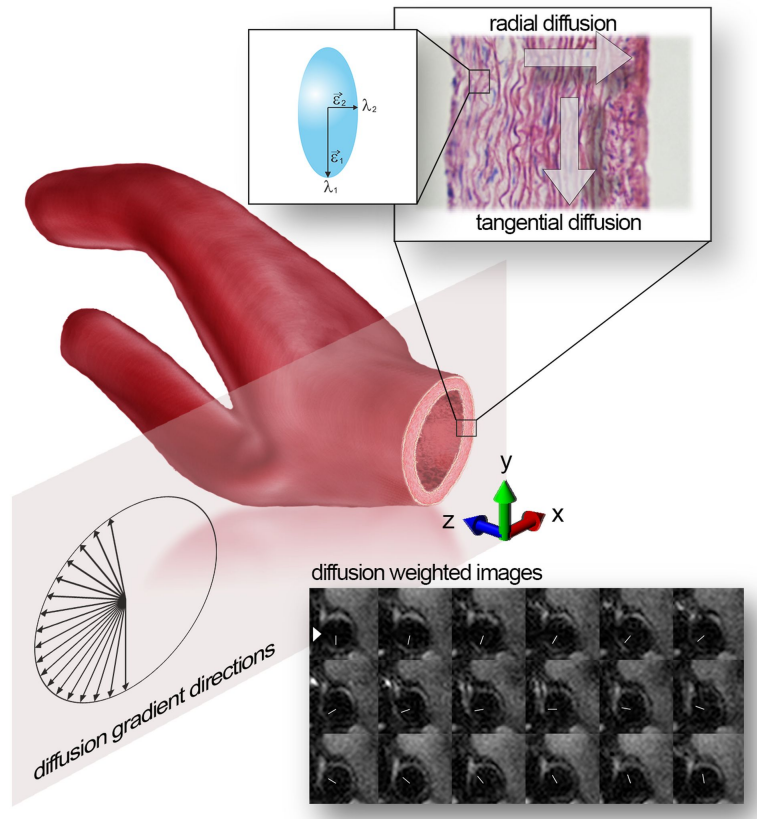
Figure 21: Gradient direction scheme to measure tangential and radial diffusion. **Top** The concept of tangential and radial diffusion is outlined as well as the 2D ellipsoid with eigenvalues (λ) and eigenvectors (ϵ). **Middle** The sketch outlines the anatomical region of interest (carotid artery) and the orientation of the 18 diffusion gradient directions on a hemicycle within a plane perpendicular to the longitudinal axis of the carotid artery (black arrows). **Bottom** Representative in vivo DWI from a carotid artery at a b-value of $600s/mm^2$ for the 18 diffusion directions (white headless arrows).

Preliminary work on porcine aorta:

Ex vivo DWI of a slaughterhouse harvested porcine aorta was performed on one selected axial slice using rs-EPI and both a three-dimensional gradient direction schema with 30 directions (Multi Directional Diffusion Weighting, MDDW; acquisition time = ∼50 min) and a two-dimensional schema with 18 directions (acquisition time = ∼30 min). Sequence parameters were as follows: FOV = 111x111 mm^2, matrix = 308x308, slice thickness = 10 mm, T_R = 2500 ms, T_E = 81 ms, GRAPPA = 2, number of readout

segments = 31, b-values = 0 and 1000 s/mm^2. To extract angle distributions of the principle 3D-DTI tangential vector with respect to the longitudinal axis of the artery Eq.(22) was used.

$$\Theta = \frac{\pi}{2} - arccos \frac{z}{\sqrt{x^2 + y^2 + z^2}} \tag{22}$$

To optimize imaging conditions, ex vivo specimens were immersed in a fluid (1,1,2-Trichloro-1,2,2-trifluoroethane, Genetron® 113, Sigma-Aldrich) having no MR signal and to minimize magnetic susceptibility effects at air-tissue boundaries [78, 121].

In vivo MR imaging:
The 2D diffusion acquisition scheme was used for in vivo measurements requiring that the diffusion sensitizing directions, lying within a plane in space, are oriented perpendicular to the artery's axis. This was achieved by defining the diffusion directions in the (p,r,s) coordinate system that is linked to the orientation of the field of view.

High resolution diffusion weighted imaging (DWI) of twelve healthy male volunteers (25-60years) was performed on one selected axial slice using rs-EPI on a 3T whole body MR scanner (Prisma, Siemens Medical Solutions, Erlangen, Germany) with a 2x4 channel multifunctional coil (NORAS MRI products GmbH, Germany) and FOV = 189x189 mm^2, matrix = 346x346, slice thickness = 10 mm, T_R = 2RR intervals, trigger delay = 50ms to acquire images in the diastolic phase, T_E = 93 ms, GRAPPA = 2, number of readout segments = 9, b-values = 0, 200, 400, 600 s/mm^2, acquisition time = ~12 min. 18 gradient directions were defined on a hemicycle within a plane oriented perpendicular to the longitudinal axis of the carotid artery. To minimize artifacts, introduced by pulsatile vessel motion, peripheral pulse-triggering was performed using the systems' internal physiological monitoring unit. To avoid chemical shift artifacts caused by periadventitial fat, a spectral fat saturation pulse was applied. A series of two-dimensional (2D) angiographic axial vessel scout images (TurboFLASH: T_R = 500ms, T_I = 280ms, T_E = 4.65ms, flip angle = 15°, FOV = 150x150 mm^2, matrix = 256x102, slice thickness = 5mm, acquisition time = ~1 min) preceded the main task to locate the carotids and orient the slice perpendicular to the long axis of the artery. Measured DWI data with an in-plane resolution of 0.55x0.55 mm^2 were interpolated to 0.2x0.2 mm^2 using zero-filling. *Registration* of the individual DWI images was achieved by applying publicly available elastix software [122, 123]. In detail, registration of the individual DWI images was applied to the b0 image. The registration process included a rigid registration (in-plane

translation only) to correct for motion introduced by the relaxing back muscles during the investigation. In a next step the wall of the individual DWI images was manually segmented to prevent misregistration to the dominant spine/neck structures. As a final processing step in order to correct for distortions introduced by more complex motion (eddy currents, breathing, swallowing and residual vessel motion) a B-spline transform was applied to register the delineated wall DWI images [124, 125].

The study was approved by the institutional review board (IRB) as well as followed Declaration of Helsinki recommendations and informed consent was signed by each participant prior to the MR measurements.

Reproducibility of in vivo FA measurements:

To test the robustness of repeated FA measurements using the above introduced in vivo high resolution diffusion weighted imaging (DWI) sequence, the carotid artery of four male volunteers was repeatedly (in total four visits) measured and the coefficient of variation (CV), defined as the ratio of the standard deviation (σ) to the mean ($\bar{x}$), was calculated.

Multiple b-value selection for the in vivo DWI imaging experiment:

The afore mentioned in vivo high resolution diffusion weighted imaging (DWI) parameter setup was used to investigate optimal b-values on one selected axial carotid slice of a male volunteer. With all other sequence parameters held constant, the T_E was set to 97ms in order to allow for measurements with increasing b-values from 0 to 1000 s/mm^2 (in steps of 200 s/mm^2) for a certain diffusion gradient direction perpendicular to the slice direction.

Statistical Analysis:

To investigate the relationship between fractional anisotropy (FA), radial diffusivity (RD) and primary eigenvalue (λ_1) data with volunteer's age a linear regression analysis was used to estimate parameters (coefficient of determination (R^2), slope and intercept) and assess linearity. In addition, 95% confidence and prediction intervals for the linear regression were calculated. An F-test for linear models was employed to compare variances and a probability value of $P < 0.05$ was considered as significant. Normal distribution was tested based on Shapiro-Wilk Normality Test. All analyses were per-

formed using freely available R-project software [126].

Diffusion tensor mathematics, FA, RD, MD and primary eigenvalue calculation:
The 3D diffusion tensor described by a symmetric 3x3 matrix and its derived quantities can easily be reduced to the 2D case where the tensor is defined by a 2x2 matrix. Mathematical aspects are discussed in the following and are detailed described by Kingsley et al [106, 107, 108]. A Levenberg-Marquardt nonlinear least squares fitting algorithm was applied based on Eq.(23) to calculate diffusion coefficients (D, measured apparent diffusion coefficient) for every voxel for all measured gradient directions. Attenuation of the MRI signal S(b) is introduced by varying the b value (200, 400, 600 s/mm^2) sensitizing it to water diffusion. S_0 represents the reference signal without diffusion weighting (no diffusion gradient).

$$S(b) = S_0 e^{-bD} \tag{23}$$

The 2D gradient direction sampling scheme enables the evaluation of the diffusion tensor **d** by solving Eq.(24):

$$\mathbf{Y} = \mathbf{Hd} \tag{24}$$

where **Y** represents the calculated apparent diffusion coefficients (18 element row vector), **H** is derived from the normalized gradient components Eq.(25) and **d** is the tensor given as a three-element column vector Eq.(26).

$$\mathbf{H} = \begin{pmatrix} g_{x1}^2 & g_{y1}^2 & 2g_{x1}g_{y1} \\ \vdots & \vdots & \vdots \\ g_{x18}^2 & g_{y18}^2 & 2g_{x18}g_{y18} \end{pmatrix} \tag{25}$$

$$\mathbf{d} = \begin{bmatrix} D_{xx} & D_{yy} & D_{xy} \end{bmatrix}^T \tag{26}$$

From tensor $\mathbf{d}$ corresponding eigenvalues (λ) and eigenvectors (ϵ) can be calculated on a pixel by pixel basis using eigenvalue decomposition. To study tangential and radial diffusion of the vessel wall 2D FA values were obtained using Eq.(27).

$$FA = \frac{\lambda_1 - \lambda_2}{\sqrt{\lambda_1^2 + \lambda_2^2}} \tag{27}$$

FA values close to zero mean no directed diffusion whereas anisotropy is given if one of the eigenvalues will be higher than the other. Calculation included the primary eigenvalue (λ_1), RD (λ_2 for the two-dimensional tensor) and the mean diffusivity (MD) which is the average of the eigenvalues.

Results:

In vivo vessel wall diffusion imaging:

Table 4 summarizes the calculated mean diffusion components as well as the mean diffusivity (MD) and FA for the high resolution 2D-DTI in vivo case of the twelve male volunteers. The tangential and radial diffusion components correspond to the eigenvalues λ_1 and λ_2, respectively.

Table 4: Volunteer Demographics and mean diffusion components of the in vivo high resolution 2D-DTI case

Demographic		Diffusion Tensor			
Volunteer male	Age yr	Tangential (λ_1) (mm^2/s)	Radial (λ_2) (mm^2/s)	MD (mm^2/s)	FA
V1	27	1.59±0.52	0.44±0.32	1.02±0.36	0.697±0.192
V2	29	1.84±0.47	0.55±0.22	1.19±0.28	0.659±0.147
V3	32	1.85±0.69	0.64±0.36	1.24±0.50	0.636±0.151
V4	33	2.29±0.80	0.71±0.30	1.50±0.50	0.653±0.118
V5	33	3.61±2.60	1.14±0.52	2.38±1.49	0.612±0.131
V6	34	3.10±1.07	1.11±0.44	2.11±0.67	0.592±0.145
V7	37	2.05±0.77	0.74±0.43	1.40±0.54	0.604±0.180
V8	41	2.31±0.63	1.04±0.39	1.68±0.44	0.500±0.148
V9	44	2.56±0.65	0.99±0.48	1.78±0.50	0.581±0.181
V10	45	2.34±0.79	0.91±0.42	1.63±0.55	0.571±0.165
V11	47	2.58±0.66	1.09±0.41	1.84±0.46	0.527±0.163
V12	57	2.22±0.54	0.88±0.29	1.55±0.38	0.563±0.118
		x1e-3	x1e-3	x1e-3	

MD, mean diffusivity. Data are reported as x̄±σ.

Figure 21 outlines the anatomical region of interest (carotid artery) and the orientation of the diffusion gradient directions on a hemicycle within a plane perpendicular to the longitudinal axis of the carotid artery. The concept of tangential and radial diffusion as well as the two-dimensional diffusion ellipsoid with eigenvalues (λ) and eigenvectors (ϵ) is delineated. In addition, Figure 21 shows representative in vivo DWI from the carotid artery at a b-value of 600 s/mm^2 for the predefined set of diffusion directions (headless white arrows). It can be observed that the signal is suppressed in the direction of the diffusion sensitizing gradient, marked by the white arrowhead. Calculating the 2D diffusion tensor revealed consistently for all twelve volunteers that the largest eigenvalue is oriented tangential to the vessel wall while the second component therefore shows a radial orientation. This fact provides clear evidence for the tangential direction as the principle contribution for diffusion within the vessel wall as shown in Figure 22A. Based on the eigenvalues a two-dimensional fractional anisotropy map (FA) was generated (Figure 22B). Additionally overlain is the direction of the principal DTI vectors denoted by the red lines.
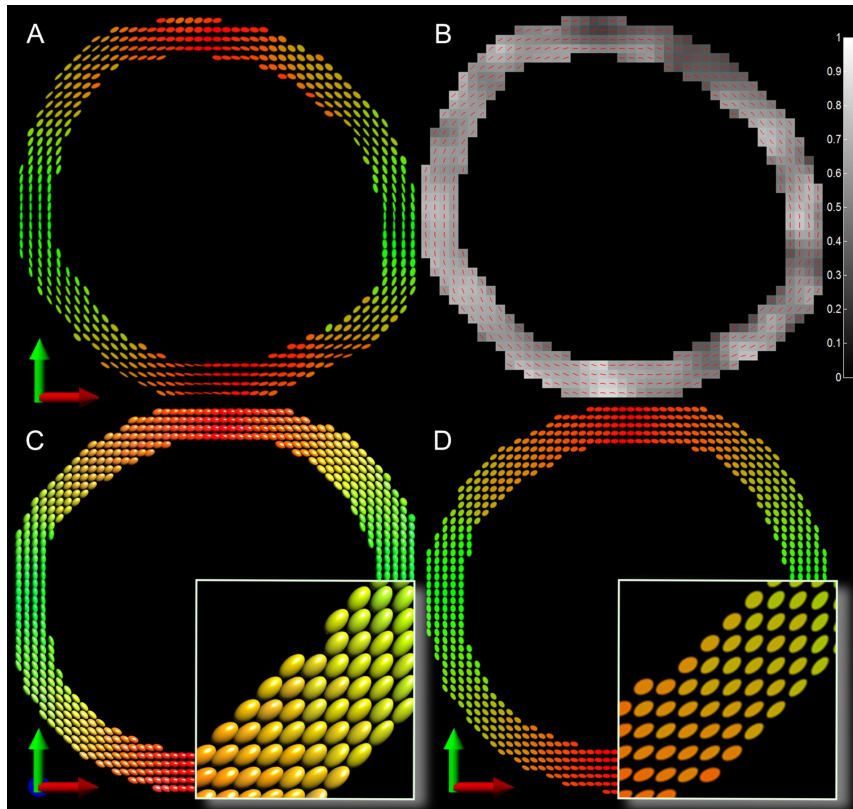
Figure 22: Color coded vector images of the principle diffusion tensor direction and FA map. **A** Representative RG vector image illustrating the diffusion tensor directions as 2D ellipsoids. **B** Corresponding FA map with superimposed direction of the principle DTI vectors by red lines. **C** RGB vector image based on the 3D-DTI rs-EPI with 30 gradient directions representing diffusion tensor directions as 3D ellipsoids of a porcine aorta. **D** RG vector image based on the 2D-DTI rs-EPI with 18 gradient directions representing diffusion tensor directions as 2D ellipsoids of the same porcine aorta.

Robustness of in vivo FA measurements:

Table 5 summarizes repeated measurements (#1 to #4) of individual mean FA values of four male volunteers (R1 to R4). The robustness of the measurement is demonstrated by the coefficient of variation (CV) with values ranging from 2.5% to 5.4%.

Table 5: Repeatability of mean FA measurements tested on four male volunteers

| | Volunteer | | | |
	R1	R2	R3	R4
#1	0.525	0.551	0.592	0.535
#2	0.562	0.585	0.604	0.540
#3	0.563	0.614	0.607	0.566
#4	0.597	0.617	0.628	0.602
σ	0.029	0.031	0.015	0.031
$\bar{x}$	0.562	0.592	0.608	0.561
CV	5.3%	5.2%	2.5%	5.4%

3D and 2D diffusion comparison in porcine:

To confirm the tangential diffusion as the direction of the largest eigenvalue ex vivo high resolution 3D-DTI and 2D-DTI of a slaughterhouse harvested porcine aorta was performed using rs-EPI. Figure 22C and 22D represents the 3D diffusion tensor as ellipsoids in a three-dimensional color space (RGB), and the 2D diffusion tensor in a two-dimensional color space (RG), respectively. Calculating the angle between the principle diffusion direction and the artery's axis for the 3D measurement, the mean value of $1.8 \pm 7.2°$ confirms the dominant orientation of diffusion perpendicular to the artery's axis. The low diffusion in z-direction justifies the 2D diffusion measurement perpendicular to the artery's axis allowing for in vivo measurements in a clinically feasible time due to the lower number of diffusion sensitizing gradient directions. In addition, Table 6 and 7 summarizes the calculated mean diffusion components for the high resolution 2D-DTI (tangential and radial) and 3D-DTI (tangential, radial and longitudinal) ex vivo case of the slaughterhouse porcine aorta. For the 2D case the diffusion components correspond to the eigenvalues λ_1 and λ_2. For the 3D case the tangential component corresponds to the largest eigenvalue (λ_1). The radial and longitudinal components can either be λ_2 or λ_3 because both eigenvalues are in a comparable range of magnitude (Figure 22C).

Table 6: Mean diffusion components of the ex vivo high resolution 2D-DTI case

2D			
Tangential (λ_1) (mm^2/s)	Radial (λ_2) (mm^2/s)	MD (mm^2/s)	FA
1.10±0.08	0.65±0.10	0.88±0.08	0.36±0.07
x1e-3	x1e-3	x1e-3	

Data are reported as $\bar{x}\pm\sigma$.

Table 7: Mean diffusion components of the ex vivo high resolution 3D-DTI case

3D				
Tangential (λ_1) (mm^2/s)	Radial (mm^2/s)	Longitudinal (mm^2/s)	MD (mm^2/s)	FA
1.07±0.06	0.64±0.10	0.62±0.07	0.78±0.06	0.32±0.04
x1e-3	x1e-3	x1e-3	x1e-3	

Data are reported as $\bar{x}\pm\sigma$.

b-value estimation:

To estimate optimal b-values and study the tissues' anisotropic properties, an in vivo vessel wall ADC map was generated from multiple measurements with increasing b-values (0-1000 s/mm^2) for a certain diffusion direction perpendicular to the slice direction (Figure 23A).
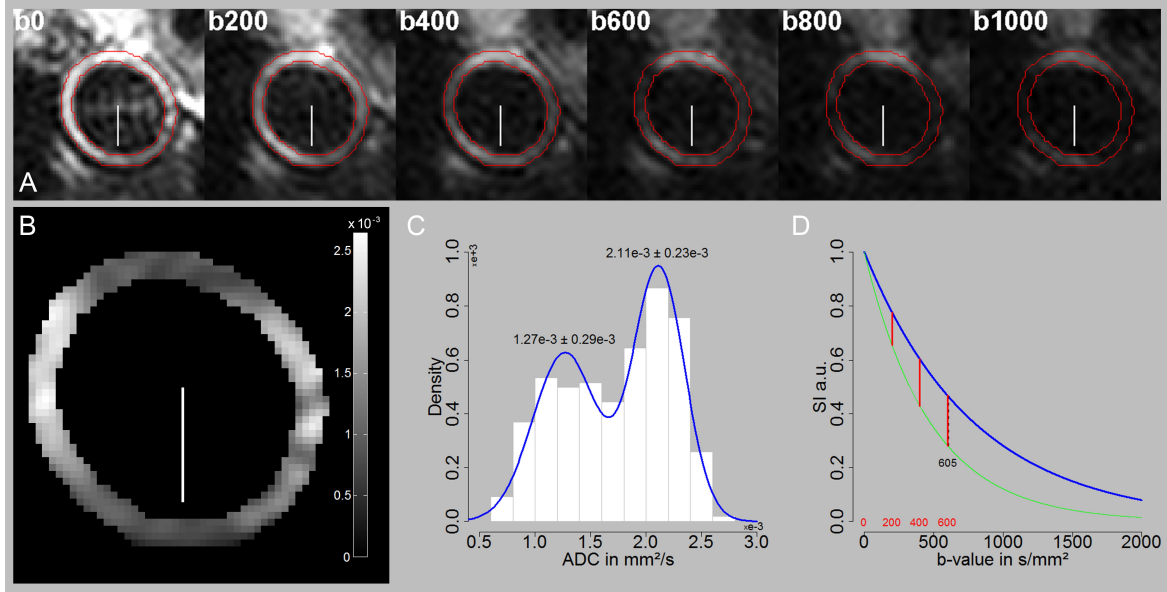
Figure 23: Vessel wall ADC map generated from six b-values images (0-1000 s/mm^2). **A** B-value images along a certain gradient direction perpendicular to the slice direction (white headless arrow). **B** ADC map generated from the six b-value images illustrating a signal enhancement along and a signal drop perpendicular to the direction of the applied gradient direction. **C** Histogram distribution of ADC map indicating two populations of ADC values. **D** Result of signal simulation using equation $S(b) = S_0 e^{-bD}$ and found ADC populations (green line 2.11 and blue line 1.27e-3 mm^2/s). Red vertical lines indicate the final set of selected b-values and black dashed vertical line the maximum difference of the found ADC pool.

Given that a signal drop can be observed in the direction of the applied diffusion gradient direction and a signal enhancement perpendicular to it, a diffusion process perpendicular to the vessels' longitudinal axis is assumable as exemplified in Figure 23B. As shown in Figure 23C, two pools of ADC values could be identified (mean values: $2.11e-3 \pm 0.23e-3$ and $1.27e-3 \pm 0.29e-3 mm^2/s$). In addition, outlined in Figure 3D is the final selected set of four equidistant b-value increments (0, 200, 400, 600 s/mm^2) and the maximum difference of both populations found at a b-value of about 605 s/mm^2. In addition to the diffusion decay factor e^{-bD}, signal loss is given by the vessel's tissue T_2 relaxation time and predefined echo time as expressed by the decay constant e^{-T_E/T_2}. All these effects contribute to a signal drop and justify a distribution of selected b-values between zero and the found maximum.

58

FA, RD and primary eigenvalue vs. age relationship:

In Figure 24A, B and C, mean vessel wall FA, RD and primary eigenvalue (λ_1) data for twelve male volunteers ranging from 0.7 for the youngest to 0.56 for the oldest are plotted as a function of age. The linear regression for the FA and age relationship was highly significant $P < 0.01$ with an adjusted R^2 of 0.52 and the linear equation y = -0.0049x+0.79. For the relationship between mean RD and age a linear trend $P < 0.1$ with an adjusted R^2 of 0.18 was observed. No linear relationship $P > 0.6$ between the mean primary eigenvalues (λ_1) and age was found. This analysis indicates that FA, measured within the vessel wall, is a sensitive parameter able to capture changes in the vascular architecture due to aging.
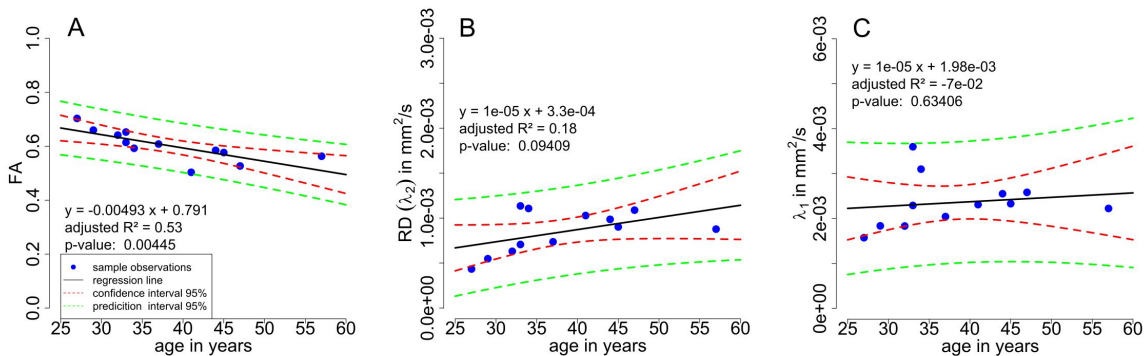
Figure 24: Linear regression analyses to compare FA, RD and $lambda_1$ vessel wall values with volunteer's age. **A** Significant linear relationship (p-value=0.00477) between mean FA and age; black solid line represents the fitted linear model (adjusted $R^2 = 0.52$; linear equation: y=-0.0049x+0.79). B, Linear trend (p-value=0.095) between mean RD and age; black solid line represents the fitted linear model (adjusted $R^2 = 0.18$; linear equation: y=1e-5x+3.4e-4). **C** No linear relationship (p-value=0.65) between the mean primary eigenvalues ($lambda_1$) and age was found; black solid line represents the fitted linear model (adjusted $R^2 = -0.08$; linear equation: y=1e-5x+2e-3). In addition, calculated 95% confidence (CI, red dashed line) and prediction intervals (PI, green dashed line) are plotted.

Discussion:

Twelve healthy male volunteers with varying ages (between 25 and 60years) were imaged and consistently revealed the tangential component as the principle direction of diffusion. Moreover, a significant linear relationship between age and FA (decrease of FA with increasing age) was found which may indicate a possible alteration of tissue microstructural integrity. In addition, these findings point FA being a sensitive metric able to uncover

changes in the wall architecture with age. The reduction from a three-dimensional tensor to a two-dimensional one is supported and was proofed by an ex vivo investigation of a porcine aorta which showed an excellent agreement of the tangential and radial components from the 2D and 3D DTI analysis. Slightly higher anisotropy values were achieved for the 2D case as the component of the z-direction (vessel's longitudinal axis) is not contributing to the FA calculation. Motion has been shown to be a huge contributing factor in achieving accurate estimates of the self-diffusion tensor [111, 113, 114, 127]. Xie et al presented a R-wave triggered 3D black-blood variable flip angle turbo spin echo sequence (SPACE) in combination with a diffusion preparation module and additional self-gating readout to compensate for motion artifacts [128]. A further implementation is the pulse-wave triggered 3D black-blood diffusion-prepared turbo spin echo sequence (DP-TSE) with segmented 3D TSE kernel and reduced field of view (rFOV) [114]. The diffusion module is based on the driven equilibrium technique and designed to additionally compensate for 1st order motion and eddy currents by using a pair of bipolar gradients and extra gradients to suppress residual blood spins. Another technique presented by Kim et al is the 2D single-shot interleaved multislice inner volume diffusion weighted echo planar imaging sequence (2D ss-IMIV-DWEPI). Its a modified standard ss-EPI using IMIV preparation pulses to allow for inner volume imaging (rFOV) and time-efficient interleaved acquisition of multiple slices. For these implementations, phase encoding steps are reduced due to the reduced FOV and therefore T_2^* blurring and evolving phase errors causing susceptibility related geometric distortions. They could show that the quality of vessel appearance is dramatically improved when compared to the standard 2D ss-EPI technique. However, these techniques are used to compute ADC values along the slice direction and do not allow quantification of the tensor. Several strategies of the proposed 2D method for measuring the circumferential orientation of diffusion address the aspect of motion. Firstly, the rs-EPI sequence (syngo RESOLVE) corrects for non-linear phase errors introduced by non-rigid body motion using a 2D navigator echo and parallel imaging (GRAPPA) further helps to reduce the sensitivity to image distortions by shortening the EPI echo spacing [129, 130, 120, 131, 132]. Secondly, pulse-wave triggering reduces pulsatile related motion artifacts and thirdly the distance between images is minimized by a coregistration process including translation followed by b-spline based registration. Finally, repeatability measurements of mean FA values (2.5 to 5.4%) clearly depict the robustness and feasibility of the 2D tensor technique. In the following, (*Chapter 4.3*) consequences of dietary regimens on aortic lesion development in a rabbit model of atherosclerosis is outlined.

4.3 An ex vivo NZW study: consequences of aortic atherosclerosis induced by HHcy and HCL

Introduction:

As already outlined in *Chapter 2* NZW rabbits require a stimulus to induce aortic atherosclerosis. The most popular strategy is the combination of a dietary trigger and balloon catheter denudation. In general, rabbits (>3kg) are fed a high-fat diet (0.5 to 2% cholesterol) for 4 to 16 weeks to induce hypercholesterolemia and mechanical injury is performed on one or two occasions (one month separation) with the first started in parallel with or slightly delayed (1 to 2 weeks) to the diet [28].

Beside hypercholesterolemia (HCL) as the major risk factor for atherosclerosis, hyperhomocysteinemia (HHcy), characterized by elevated levels of homocysteine (Hcy) and normal serum lipids, has been recognized as another independent risk factor [133]. In short, an increase in Hcy leads to synthesis of S-adenosyl-L-homocysteine (AdoHcy) which in turn inhibits the methylation of lipids, proteins, nucleic acid, phospholipids etc. by S-adenosyl-L-methionine (AdoMet)-dependent methyltransferases. Pathological consequence stimulated by elevated levels of Hcy on atherosclerosis are poorly understood. A project (Futurespace) funded by the 'BioTechMed initiative ($https : //biotechmedgraz.at/en/projects/interlinking-formats/future-space/$)' aimed at investigating HHcy-associated atherosclerosis in rabbits and to compare it to the conventional high-cholesterol induced counterpart. HHcy is stimulated by a special diet deficient in choline, folate, vitamine B_6 and B_{12}. The project was performed in collaboration with the Clinical Institute of Medical and Chemical Laboratory Diagnostics (Gunter Almer), Medical University of Graz and the Institute of Molecular Biosciences (Oksana Tehlivets, Heimo Wolinski), University of Graz.

Methods:

Animal model:

A total of ten male New Zealand White (NZW) rabbits (age: 8 to 9 months; body weight: 3.5-4.5kg) were used in this study. Abdominal aortic atherosclerosis was induced in all rabbits by a combination of balloon catheter denudation and a two month special(normal) diet (6 to 8 weeks: started in parallel to the injury), followed by a normal chow diet (1 to 2 weeks). The injury was performed from the renal artery to the iliac bifurcation introducing a Fogarty 4F embolectomy balloon catheter (Edwards Lifesciences) through the femoral artery. Four rabbits were fed a special diet deficient in

choline, folate, vitamine B_6 and B_{12} to induce HHcy-associated atherosclerosis. Three rabbits were fed a 1% high-cholesterol diet to induce hypercholesterolemia. Three control rabbits were maintained on a normal chow diet. After the preparatory regimen the animals were sacrificed, abdominal aortic specimens dissected and prepared for ex vivo MR imaging @7T Bruker Biospec 70/20 and MRI CryoProbe, histology and microscopy. All animal procedures were approved by the Ministry of Science and Research, Austria.

MR imaging:

The ex vivo specimens were immersed in a fluid (1,1,2-Trichloro-1,2,2-trifluoroethane, Genetron® 113, Sigma-Aldrich) to minimize magnetic susceptibility effects at air-tissue boundaries [78, 121]. An accurate preparation of the three control sections for ex vivo MRI was impossible due to the soft and collapsing structure, instead a portion of a high-fat diet sample free of atherosclerotic lesions was used as a pseudo-control. T_1 and T_2 relaxometry was performed using a spin-echo sequence with variable time of repetition TR (2D RAREVTR) and diffusion weighted imaging (2D DWI) was achieved using a readout segmented EPI (rs-EPI) with a three-dimensional gradient direction schema of 120 directions (b-value of 1000 s/mm2) plus 10 A0 images. Measurements were performed at room temperature.

RAREVR parameter: T_R 200 to 5500ms (200/400/800/1500/3000/5500ms, six experiments), T_E 7 to 63ms (spacing of 14ms, five experiments), FOV=20.48x15.36mm^2, matrix= 256x192, resolution= 80x80μm^2, slice thickness= 800μm, NEX= 1, ETL= 1, five slices, bandwidth= 318Hz/pixel, spectral fat suppression, 30min acquisition time.

rs-EPI parameter: T_R= 2000ms, T_E= 21.13ms, number of readout segments = 4, bandwidth= 250kHz, FOV= 10.24x10.24mm^2, matrix= 128x128, partial FT in phase direction= 1.6 (80 phase encoding lines), resolution= 80x80μm^2, slice thickness= 800μm, NEX= 4, nine slices, spectral fat suppression, $\sim$ one hour acquisition time.

MR data analysis:

Inner and outer vessel wall boundaries of the RAREVTR and DWI intensity images (average of the 10 A0 images) were manually segmented using ITK-SNAP and used as a mask for T_1 and T_2 relaxometry and to calculate the normalized wall index (NWI=wall area/total vessel area) as a measure of wall thickening, respectively. A Levenberg-Marquardt nonlinear least squares fitting algorithm was applied to $SI(T_E) = S_0 e^{T_E/T_2}$ for calculating T_2 relaxation times voxel-wise (two-parameter fitting routine). A three-parameter fitting routine was applied to $SI(T_R) = S_0(1 - ce^{T_R/T_1})$ for calculating T_1

relaxation times voxel-wise.

Histopathology and Immunohistochemistry:
Oilred O and hematoxylin stains were used for the detection of neutral lipids and nuclei, respectively. RAM11 antibody and neutral red stains were used for the detection of macrophages and nuclei, respectively.

Microscopy: second harmonic generation (SHG) and coherent anti-Stokes Raman scattering (CARS):
SHG is a nonlinear optical microscopy modality, high in resolution and allows the visualization of non-centrosymmetric molecule structures like collagen of the arterial wall [117]. In addition, CARS microscopy was used to visualize the lipid content of selected vessel sections [134].

Results:
Histology and microscopy:
It can clearly be seen from Figure 25ABI-III, that aortic atherosclerosis is most severe for animals fed a high-cholesterol diet whereas rabbits on a normal chow and high Hcy show a similar lower plaque progression and thickening. High levels of lipid and macrophage deposition is observed throughout the thickened aortic wall for the high-fat diet. Compared to that, a more moderate deposition of lipids and macrophages is found for the normal chow rabbits and an interesting much less deposition of both components at different layers for the HHcy animals. As can be seen from Figure 25CI-III, an organized and directed structure of collagen (SHG, green signal) is observed for all three dietary types on the microscopic images. However, the collagen texture seems to be altered for the HCL and HHcy group with some lipid depositions (CARS, red signal) in between the fibres.
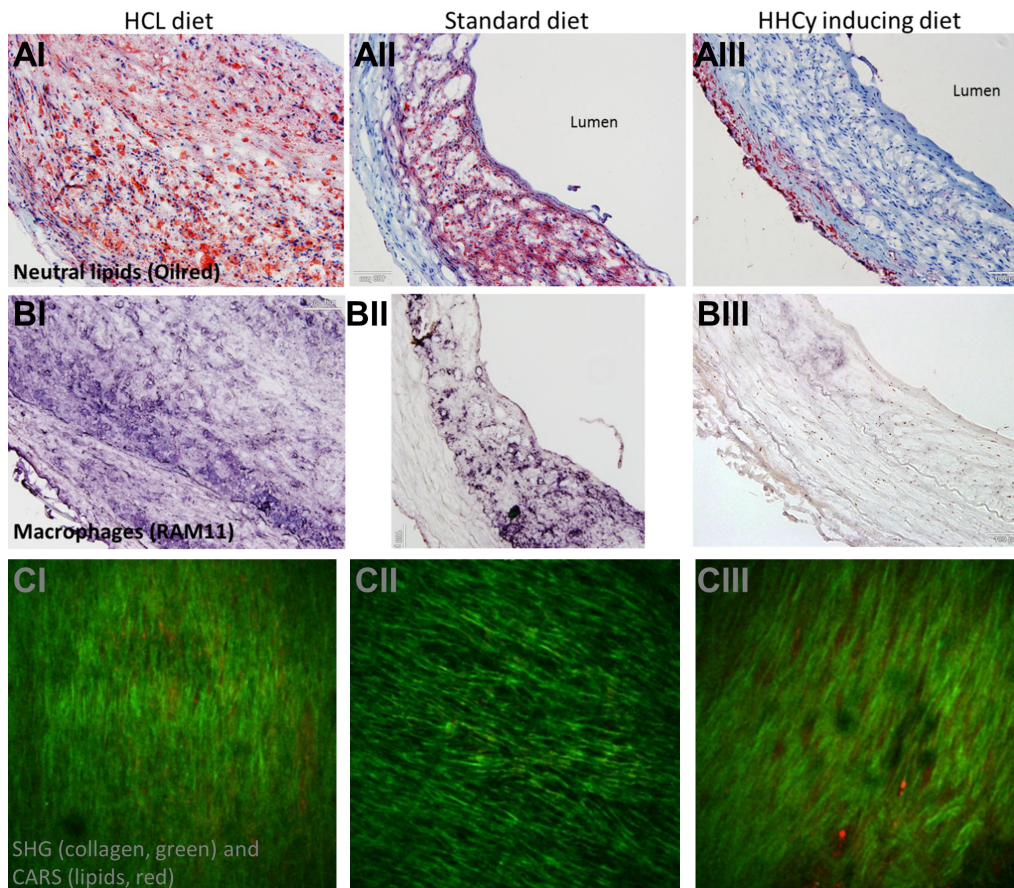
Figure 25: Histology and microscopy of balloon injured HCL, normal chow and HHcy rabbits. **AI-III** Oilred O and hematoxylin stains for the detection of neutral lipids and nuclei, respectively. **BI-III** RAM11 antibody and neutral red stains for the detection of macrophages and nuclei, respectively. Balloon injured rabbits show levels of lipid and macrophage deposition dependent on the dietary regimen. **CI-III** SHG and CARS for the detection of collagen and lipids, respectively. All balloon injured dietary types show an organized and directed structure of collagen with some lipid depositions in between the fibres. SHG, second harmonic generation; CARS, coherent anti-Stokes Raman scattering; HCL, hypercholesterolemia; HHcy, hyperhomocysteinemia.

ex vivo MRI:

Figure 26 shows the effect of the dietary regimen (HCL, HHcy) on the fractional anisotropy (FA), normalized wall index (NWI), T_1 and T_2 relaxation time parameters. The bar plots clearly indicate a strong trend to lower FA and increasing NWI values parallel to the severity of the aortic atherosclerosis (wall thickening). In addition, T_1 and T_2 relaxation times seem to be highest for the high-cholesterol diet rabbits and lowest for intact plaque free wall areas (pseudo-control).

64
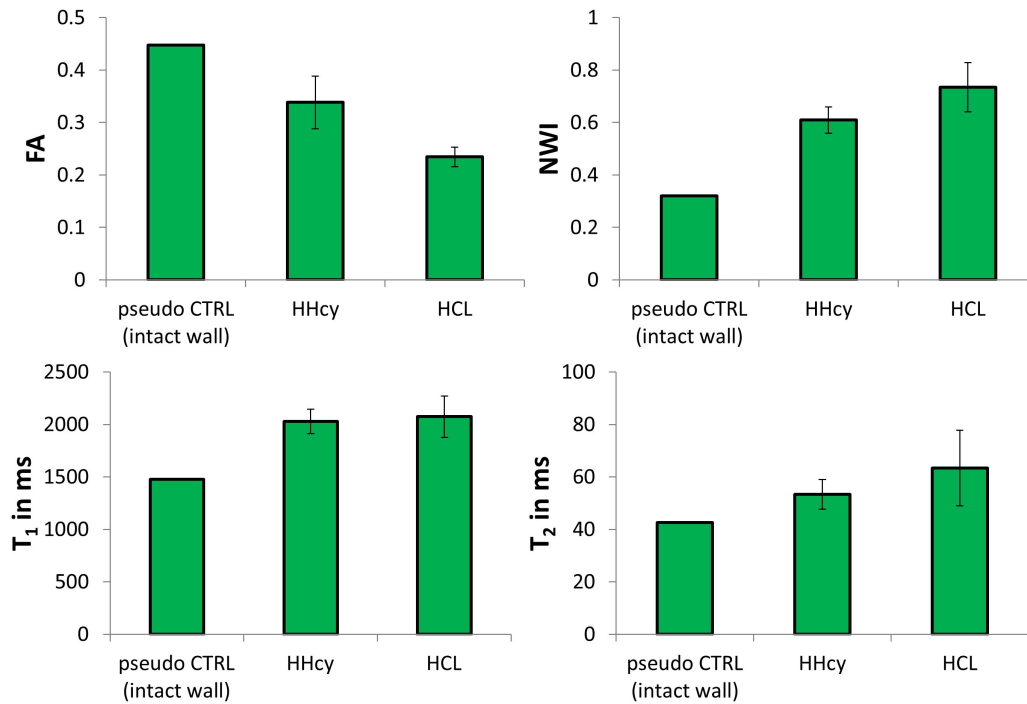
Figure 26: Effect of dietary regimen (HCL: n=3; HHcy: n=3) on fractional anisotropy (FA), normalized wall index (NWI), T_1 and T_2 relaxation time parameters. Bar plots indicate change in parameter values parallel to the severity of the aortic atherosclerosis (wall thickening). An intact plaque free control sample of a high-fat diet rabbit (pseudo-control, pseudo CTRL: n=1) is used for the sake of comparison.

Figure 27 shows representative T_1, T_2 maps and RGB vector images of the principle diffusion tensor direction for the balloon injured rabbits and the effect of the dietary regimen. The T_1, T_2 maps clearly highlight increased wall relaxation times for rabbits with a thickened wall (HCL, HHcy) when compared to the control (pCTRL). The RGB vector image of the pseudo-control clearly depicts the tangential direction as the principle contribution for diffusion within the vessel wall and therefore the largest eigenvalue oriented tangential to the vessel. For the rabbits with aortic atherosclerosis (HCL, HHcy) a similar pattern can be seen but also dominant orientations of diffusion parallel to the artery's axis for certain wall regions.
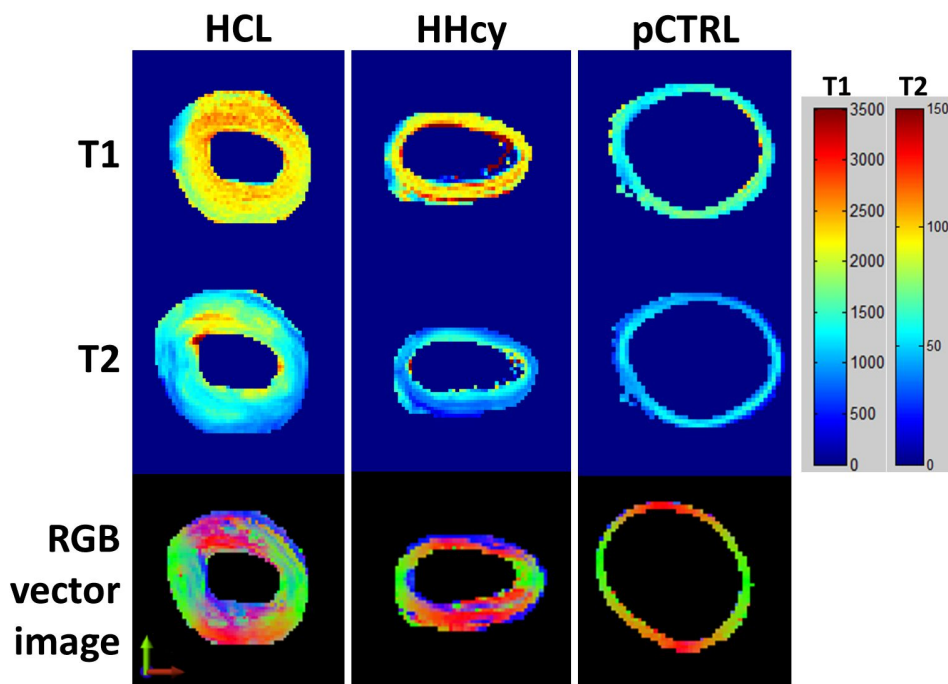
Figure 27: Representative T_1, T_2 maps and RGB vector images of the principle diffusion tensor direction for the balloon injured rabbits fed a high-cholesterol diet (HCL) or a diet deficient in choline, folate, vitamine B_6 and B_{12} to induce high levels of Hcy (HHcy). Relaxation time maps highlight increased wall T_1 and T_2 times for rabbits with a thickened wall when compared to the control. Altered dominant orientation of the diffusion from tangential to a direction parallel to the artery's axis for certain plaque areas is observed. An intact plaque free control sample of a high-fat diet rabbit (pseudo-control, pCTRL) is used for the sake of comparison.

Discussion:

In this project aimed to investigate HHcy-associated atherosclerosis a clear difference in plaque progression/appearance to the HCL and normal chow balloon injured rabbits could be demonstrated. Increased relaxation times seen for HCL and HHcy compared to an intact plaque free control sample may derive from alterations of the tissue microstructural integrity (change in collagen texture) and loosened architecture as can be seen from the histological and microscopic images. This may also alter the dominant orientation of the diffusion from tangential to a direction parallel to the artery's axis for certain plaque areas. Based on these data a *FWF project proposal (principle investigator: Oksana Tehlivets, Institute of Molecular Biosciences, University of Graz, Austria)* is prepared to investigate consequences of metabolic pathways leading to hyperhomocysteinemia on the architecture of atherosclerotic plaques.

5 Molecular plaque MRI using (super)paramagnetic nanoparticles

5.1 Introduction

Gadolinium chelates and iron oxide probes are two major families of MR contrast agents, both successfully applied in atherosclerotic plaque MRI. While (native) multispectral protocols or all-in-one solutions (see *Chapter 3*) aim at identifying plaque morphology (volume and area measurements of wall, lumen, total vessel or plaque etc.) and composition (CA, IPH, FC, LRNC etc.) molecular MRI uses (functionalized)-probes to uncover molecular/cellular processes by targeting biomarkers of apoptosis, necrosis, angiogenesis, thrombosis and inflammation. Moreover, monitoring response to therapy ('theranostic') or lesion progression/regression further extends the scope of molecular imaging strategies. Among the class of iron oxides, ultrasmall superparamagnetic iron oxides (USPIOs) were used in the past as a surrogate marker for plaque inflammation as passive targeting probes (up to 1mmol Fe/kg bw) or functionalized (in the range of 0.1mmol Fe/kg bw) to target proinflammatory endothelial surface markers (VCAM-1, E-selectin, P-selectin) in animal models of atherosclerosis [135, 136, 137, 138, 139, 140]. Due to their size (<40nm hydrodynamic diameter) they are able to evade the reticuloendothelial system (RES) and circulate for a prolonged time in the blood therefore behave as an intravascular contrast agent and finally are cleared by the liver. In contrast, SPIOs with a hydrodynamic diameter above 50nm are rapidly cleared by phagocytic-endocytic systems (liver, spleen) and rather used as RES specific imaging agents or to label stem cells for cell tracking studies but rarely used for imaging atherosclerotic lesions. The accumulation of such probes at certain (plaque) tissue regions causes local magnetic nonuniformities [73, 141, 142]. For gradient echo applications, the sensitivity to that resultant magnetic susceptibility effect is dependent on the distance of water molecules to that 'focal hot spot'. As a result, accelerated spin dephasing of nearby water molecules causes signal loss on T_2^* weighted gradient echo images. As water molecules diffuse through that nonuniformity regions (field gradients) a loss of phase coherence is caused (dependent on the interecho time) and therefore a drop in signal (T2 shortening) on T2w spin echo images. The advantage of iron oxide probes compared to gadolinium based agents is their high r$_2$ relaxivity ($\frac{1}{T_{1,2}^n} = \frac{1}{T_{1,2}^0} + \frac{1}{T_{1,2}^{CA}}$; $\frac{1}{T_{1,2}^{CA}} = r_{1,2}[CA]$;

$r_{1,2} = \Delta \dfrac{1}{T_{1,2}} \dfrac{1}{[CA]}$; [CA], contrast agent concentration) which allows the detection of biomarkers in the nanomolar concentration range. Moreover, T1 shortening effects introduced by UPSIOs (Sinerem/Ferumoxtran-10, Guerbet; Supravist/SHU-555-C, Schering AG; Ferumoxytol/Feraheme, AMAG Pharmaceuticals) at moderate concentrations (in the range of 0.05mmol Fe/kg bw) impart angiographic properties and are a valuable alternative to nonspecific extravascular gadolinium based agents because of the extended blood half-life and imaging time window (equilibrium phase MR angiography), the reduced dosage and injection rate due to their higher r1 relaxivity [143, 144, 145, 146, 147]. For instance, Ferumoxytol is at the moment the sole FDA approved drug for i.v. treatment of iron deficiency anemia in patients with a kidney disease but was initially investigated as an MRI contrast agent [148, 149, 150]. A promising clinical applicable (Phase III) dextran T-10 coated USPIO (Sinerem also named Ferumoxtran-10, AMI-227, Combidex, Guerbet) was proposed by Schmitz et al and Kooi et al more than one decade ago for imaging macrophages in ruptured and rupture-prone human carotid atherosclerotic lesions at a dose of 2.6mg Fe/kg bw (low dose 0.05mmol Fe/kg bw) [151, 152, 153]. Trivedi and colleagues investigated the temporal dependence of USPIO (Sinerem, 2.6mg Fe/kg) enhanced MRI for imaging carotid atheroma and found the optimum time point to be 24 to 36h after contrast agent administration [154]. Moreover, Tang and co-workers used that agent to correlate carotid atheroma plaque inflammation with the degree of luminal stenosis and found plaque inflammation to be an independent risk factor for vulnerable lesions [155, 156]. Patterson and colleagues used Sinerem (2.6mg Fe/kg) in a dose-response study to a high vs low dose statin therapy and analyzed T_2^* relaxation time changes at three different time points (baseline, 6 and 12 weeks after therapy start) [157]. They found significant differences in carotid plaque T_2^* relaxation times between the low and high statin dose patient group demonstrating a reduction in iron oxide uptake and lowering of the T_2^* shortening effect for the high dose group. Important physicochemical properties of iron oxide nanoparticles are their ionic state (anionic, neutral), size (crystal core and hydrodynamic diameter), relaxivity, blood half-life and coating (dextran, carboxy-dextran). Sigovan and co-workers compared in a mutant model of atherosclerosis (WHHL rabbits) the well established Sinerem (dextran polymer) particle with the new P904 (LMW amino-alcohol derivative of glucose) for its ability to passively detect plaque inflammation [158]. Both particles are made up of a maghemite core but differ in coating. They found that plaque inflammation imaging by P904 is possible as early as 24h after contrast agent administration compared to Sinerem which showed peak susceptibility artifact at day seven and found faster blood pharmacokinetics (lower

blood half-life, about 3.5h in rabbits; Sinerem: several days for a dose of 1mmol Fe/kg) for P904. Ferumoxytol, another interesting candidate with a modified sugar coating (carboxy-dextran) for plaque inflammation imaging was proposed by Herborn et al and compared to Sinerem in a rabbit model of atherosclerosis (WHHL) [159]. Compared to the efficient dose of 1mmol Fe/kg used in the past for this animal model they reduced the administration to a quarter and found peak lumen enhancement for ferumoxytol after three days (faster clearance and lower blood half-life) compared to five days for the Sinerem group. Moreover, susceptibility artifacts introduced by ferumoxytol are homogeneous (parallel to the wall) compared to spotted voids caused by Sinerem reflecting a unique accumulation pattern for both iron oxides in plaque lesions. Histology showed superficial distribution of Sinerem compared to a subendothelial distribution as well as penetration into deeper layers (media) of the plaque for ferumoxytol. Beside passive targeting of inflammation, Vascular Cell Adhesion Molecule 1 (VCAM-1), E-selectin and P-selectin are proinflammatory endothelial surface markers and a very early signal of plaque formation. Kang et al showed that in vivo imaging of a human endothelial specific marker is possible by the use of E-selectin targeted iron oxides [139]. In detail, experiments were performed using a mouse model implanted with a neovascularization scaffold to image E-selectin expression in functional blood vessels. P-selectin, expressed on activated platelets as well as pathologically activated endothelium (platelet-endothelium interaction is a early event in atherosclerosis), specific imaging was investigated by Valat et al [140]. Beside the successful in vitro characterization of the specific binding properties of P-selectin targeted iron oxides, in vivo experiments in the ApoE-/- mouse model of atherosclerosis showed a strong reduction of plaque signal on T2w MR images. Kelly and colleagues found a specific cell internalizing peptide and used its property to trigger the uptake of iron oxide nanoparticles into VCAM-1 expressing endothelial cells in ApoE-/- mice in vivo [138]. Colocalization of that specific ligand functionalized nanoparticle clearly demonstrated its high affinity and ability to detect VCAM-1 expressing cells in atherosclerotic lesions. Beside endothelial markers, Schellenberger and co-workers showed in cell culture experiments that annexin functionalized iron oxide particles are able to specifically detect apoptotic cells via binding to phosphatidylserine [160]. Burtea and co-workers investigated two functionalized iron oxide nanoparticles one for targeting VCAM-1 and the second to address apoptosis (phosphatidylserine) in ApoE-/- mice in vivo by the administration of a low nanoparticle dosage (0.1mmol Fe/kg) [161]. Both particles showed the ability to accumulate at specific regions in the atherosclerotic lesion which was for the VCAM-1 targeted UPSIOs macrophages in the

cap and large necrotic core and for the phosphatidylserine targeted USPIOs macrophages and neutral fats inside the plaque. MRI results clearly showed that specific plaque imaging is possible as early as 30 minutes after contrast agent administration. Another class of nanoparticles used in plaque MR imaging are liposomes. They are made up of natural phospholipids are biodegradable, biocompatible, nontoxic, nonimmunogenic can be loaded with imaging agents (T1w/T2w) and/or therapeutic drugs, coupled with ligands for specific targeting and are adequate probes for monitoring and treatment of plaque progression/regression [31]. In contrast, iron oxide nanoparticles are of potential clinical concern in atherosclerosis imaging as it turned out that macrophages are able to degrade the iron core, release soluble iron, generate superoxidases which in turn are able to trigger oxidation of LDL (oxLDL, involved in pathogenesis of AS) [162, 163, 164]. Another strategy is to entrap iron oxide cores by polyethylene glycol (PEGylated) lipid bilayer (stealth magnetic liposomes, sML) to make the construct stealthy for the RES and allow them to circulate for a prolonged time in the blood [165]. In contrast to liposomes (size: 50-700nm) which consist of an aqueous interior, surfactant stabilized oil in water emulsions (size: 200-400nm; e.g. perfluorocarbon emulsions) allow a dramatically higher payload of gadolinium complexes and finally higher r_1 relaxivities [166]. Winter and colleagues proposed a $\alpha_v\beta_3$-integrin targeted paramagnetic perfluorocarbon nanoparticle to image angiogenesis in early stage lesions of a rabbit model of atherosclerosis (NZW on WD) [167]. A specific lesion enhancement was found within 2h for the targeted nanoparticle which was confirmed in control experiments by blocking $\alpha_v\beta_3$-integrin with a targeted nonparamagnetic agent as a pretreatment. Imaging neovascularization (angiogenesis within the adventitia) is of special interest as it is involved in the initiation and rupture of atherosclerotic plaques. Phosphatidylserine enriched paramagnetic gadolinium liposomes (Gd-PS) as apoptosis mimicking agents recognized by macrophages were proposed by Maiseyeu et al for imaging atherosclerosis in ApoE-/- mice [168]. Gd-PS enhanced in vivo MRI clearly showed enhancement of atherosclerotic lesions up to 4-8h after agent administration and colocalization was found with plaque macrophages. Mulder and colleagues introduced neointimal lesions (collar around the right carotid artery) in ApoE-/- mice and compared a conventional unspecific extravascular gadolinium agent (Gd-DTPA) with paramagnetic liposomes for the visualization of intimal thickening [169]. A strong enhancement of the right neointimal vessel wall up to 24h after liposomal agent administration could be detected compared to no enhancement when using the Gd-DTPA complex or imaging the contralateral control regions with both agents. Bochove and co-workers induced two plaque phenotypes (thin cap fibroat-

heroma TCFA & non-TCFA) in the right carotid artery (tapered cast) of ApoE-/- mice and investigated the accumulation (contrast enhancement) of three differently sized paramagnetic contrast agents (liposomes, micelles and Gd-HP-DO3A) six (intermediate) and nine (advanced lesion) weeks after further plaque development [170]. Micelles and Gd-HP-DO3A enhanced all plaque types but peak enhancement was 24h and six minutes after contrast agent administration, respectively whereas liposomes failed to show any significant plaque enhancement at any time point. The authors concluded that micelles are suitable to image markers within the plaque (able to permeate the lesion) whereas functionalized liposomes are rather appropriate to image endothelial markers associated with atherosclerosis. Table 8 lists the above described nanoparticle enhanced plaque MR imaging strategies together with selected parameters (target tissue, particle type, concentration & size, species).

Table 8: Nanoparticle enhanced 'passive/active' plaque MR imaging in mouse and rabbit models of atherosclerosis and man

Target	Nanoparticle	Concentration	Average hydrodynamic diameter	Species	Ref.
Angiography	USPIO (Sinerem, Guerbet)	up to 46μmol Fe/kg	30nm	human	[143]
	USPIO (Supravist, Schering AG)	up to 40μmol Fe/kg	20nm	human	[144]
	USPIO (Feraheme, AMAG Pharmaceuticals)	up to 36μmol Fe/kg	30nm	human	[146]
Inflammation 'passive' (macrophages)	USPIO (Sinerem, Guerbet)	1000μmol Fe/kg	80-150nm	rabbit (NZW, WHHL)	[135]
	USPIO (Feridex, Berlex Laboratories)	1000μmol Fe/kg		mouse (ApoE-/-)	[136]
	USPIO (Sinerem, Guerbet) vs.	250μmol Fe/kg		rabbit (NZW, WHHL)	[159]
	USPIO (Feraheme, AMAG Pharmaceuticals)				
	USPIO (P904, Guerbet) vs.	1000μmol Fe/kg	21nm	rabbit (NZW)	[158]
	USPIO (Sinerem, Guerbet)				
	USPIO (P904, Guerbet)	1000μmol Fe/kg		mouse (ApoE-/-)	[137]
	USPIO (Sinerem, Guerbet)	46μmol Fe/kg		human	[151, 152] [154, 155] [156, 157]
Inflammation 'active' (endothelial surface marker)	VCAM1 targeted iron oxide	90μmol Fe/kg	n/s	mouse (ApoE-/-)	[138]
	P-selectin targeted iron oxide	143μmol Fe/kg	80nm	mouse (ApoE-/-)	[140]
	E-selectin targeted iron oxide	54μmol Fe/kg	45nm	athymic nu/nu mouse	[139]
Inflammation & apoptosis 'active'	VCAM1 targeted iron oxide	100μmol Fe/kg	27nm	mouse (ApoE-/-)	[161]
	PS targeted iron oxide	100μmol Fe/kg	27nm		
Angiogenesis 'active'	$\alpha_v\beta_3$-integrin targeted PFC	0.5ml/kg (3μmol Gd/kg)	273nm	rabbit (NZW)	[167]
Inflammation via apoptosis 'active'	PS enriched paramagnetic gadolinium liposomes	100μmol Gd/kg	230nm	mouse (ApoE-/-)	[168]
Neointimal lesion 'passive'	paramagnetic liposomes	40μmol Gd/kg	90nm	mouse (ApoE-/-)	[169]
Intermediate & advanced lesion 'passive'	paramagnetic liposomes	50μmol Gd/kg	123nm	mouse (ApoE-/-)	[170]
	paramagnetic micelles	50μmol Gd/kg	16nm	mouse (ApoE-/-)	
	Gd-HP-DO3A	50μmol Gd/kg	n/s	mouse (ApoE-/-)	

n/s, not specified; PFC, perfluorocarbon nanoparticle (oil in water emulsions); PS, phosphatidylserine;

72

In the following, parts of the **book chapter** *Liposome nanoparticles for diagnostic applications* of the **book** *Liposomal Delivery Systems: Advances and Challenges* published by Future Science Ltd (2016, 188:203) are reprinted / adapted from Opriessnig et al with permission of Future Medicine [171].

Considerations for liposomal contrast agents for diagnostics:

As discussed previously, nanoparticle assisted plaque MR imaging by iron oxides, paramagnetic oil in water emulsions and liposomes clearly demonstrate their diagnostic potential to selective uncover constituents of the pathological transformed vessel wall as passive as well as active targeting probes. Moreover, liposomes have a long history in drug delivery and today a number of liposomal drugs are marketed and many more products are in clinical development and clinical trials [172]. Despite a very good track record of liposomal pharmaceuticals none of the liposomal contrast agents has reached the market so far. Even though signal emitting liposomal contrast agents have been frequently used for experimental diagnostic imaging of different organs and diseases including tumors, cardiovascular diseases or inflammations, it seems as if the clinical benefit is not high enough to justify additional expenses. In the future, however, it is reasonable to expect that multifunctional targeted liposomal imaging agents will become increasingly important for monitoring of therapy in personalized treatment [173]. An advantage in this regard is that liposomes are generally recognized as safe with a low toxicity profile. However, cytotoxicity, hematocompatibility and immunogenicity of the liposomal contrast agents strongly depend on the chemical composition of liposomes, the physicochemical characteristics of its single components as well as the absolute amount of lipids and contrast agents administered. Accordingly, all liposomal formulations need a thorough preclinical in vitro and in vivo safety evaluation before entering clinical development. Apart from safety, the liposomal products have to display a high signal intensity and a proper pharmacokinetics to be suitable for imaging. One of the drawbacks of the use of liposomes is the fast elimination from the blood and capture of the liposomal formulations by the RES, primarily in the liver. To reduce this problem surface coating of liposomes with polymers has emerged as promising strategy to develop long circulating sterically stabilized liposomes. The polymers are commonly attached to a lipid moiety and incorporated into the liposomal membrane. Metal ions or nucleotides can be easily chelated to the distal end of the polymer chain, which is directly exposed to the water. In this way a high concentration of contrast agents can be accommodated within or associated to one liposome, which enhances its signal intensity and correspondingly improves the contrast properties of the liposomal contrast agent. Fi-

nally, clinically acceptable liposomes for imaging have to meet several quality criteria in manufacturing. The production should be simple, efficient and highly reproducible. The marker molecules, dyes and targeting molecules have to be affordable and easy to handle. The loaded liposomes should be stable with no release of free label or marker molecule in vivo, and liposomes need to be stable upon storage, at least for a defined period of time [174]. Facing all the hurdles in synthesis, production, upscaling, physicochemical characterization, toxicity and regulatory mechanisms a well-defined liposomal platform for diagnostics has emerged, whose further development will expedite the translation of liposomal diagnostics to clinical applications.

Therapeutic and diagnostic options within liposomes:
Doxorubicin is a prominent anticancer drug but in its free form known for its cardiotoxicity. The encapsulation of the agent into liposomes significantly improved the pharmacokinetics and reduced drug-related off-target toxicity. Since some years the liposomal formulation is well established in clinical use [175, 172]. The synergistically use of liposomal doxorubicin in combination with an imaging agent was shown by Kono et al [176]. In their work they have tested a temperature-sensitive gadolinium containing doxorubicin loaded PEG-liposome in colon tumor bearing mice. The accumulation of the theranostic agent at the tumor site could be monitored by MRI and tumor regression was followed upon temperature triggered release of doxorubicin (localized heating). In a similar experiment, Negussie et al formulated a low temperature sensitive PEGylated liposome co-encapsulating doxorubicin and a gadolinium based imaging agent in the inner aqueous phase [177]. Triggered release of the content by MRI guided high intensity focused ultrasound (MR-HIFU) was tested in phantoms and in a Vx2 rabbit tumor model. Co-localization of the contrast agent in the tumor as well as focal tumor signal increase over time following heating interventions could be successfully monitored by MRI. Using the same technique and a comparable nanoparticle design, De Smet et al have reported similar results for 9L tumor bearing rats [178]. Both groups were able to demonstrate the in vivo proof of principle of tumor visualization and temperature feedback therapy by MRI using modified liposomes. In another approach, prednisolone phosphate (PLP), a glucocorticoid with antiinflammatory and immunosuppressive effects was encapsulated in long circulating gadolinium labeled PEG-liposomes and tested in melanoma B16 syngeneic tumor bearing mice [179]. In this study the biodistribution of the particle over time as well as tumor growth inhibition induced by PLP was visualized by MRI. The co-loading of the imaging agent did not compromise the therapeutic efficacy of the

encapsulated drug. A multimodality approach to evaluate the anti-inflammatory efficacy of a PEGylated liposomal PLP in a rabbit model of atherosclerosis was introduced by Lobatto et al [31]. The imaging function was realized by incorporation of amphiphilic gadolinium chelates for MRI and Rhodamine B for ex vivo fluorescence imaging. Additionally, ^{18}F-FDG-PET/CT imaging was performed to track the antiinflammatory effects of liposomal glucocorticoids. In another approach, neural cell adhesion molecule (NCAM) targeted gadolinium containing PEG-liposomes loaded with doxorubicin were tested in a Kaposi's sarcoma tumor bearing mouse model by Grange et al [180]. The treatment with targeted compounds inhibited tumor growth compared with control constructs as visualized by MRI. Whereas nontargeted liposomes accumulated mainly in the tumor extracellular space, targeted particles were internalized by tumor cells and led to an enhanced apoptosis and reduced vascularization. However, due to the cellular uptake, targeted liposomes showed a weaker MRI signal enhancement (quenching) compared with nontargeted ones. Folate functionalized magnetic liposomes (loaded with superparamagnetic iron oxide nanoparticles) co-loaded with doxorubicin were tested in rats and rabbits with induced liver tumors [181]. In both animal models the treatment with folate targeted liposomes induced a superior inhibition in tumor growth compared with free or liposomal doxorubicin, as determined by MRI.

Perspectives:

The versatility and adaptability of liposomes make them highly attractive for diverse applications in nanomedicine. Especially, for therapeutic and diagnostic approaches and a combination thereof, liposomes provide many advantageous properties; biocompatible, biodegradable, low toxicity, easy to manufacture, easy to handle, robust and stable. Moreover, liposomes have tunable sizes and compositions and can simultaneously be loaded and labeled with drugs and tracer molecules. And finally, liposomes can be functionalized with targeting sequences for site-specific recognition.

5.2 Evaluation of endothelial barrier function in atherosclerosis induced rabbits using S-nitroso human serum albumin (S-NO-HSA) - blood pool agent compound and dynamic contrast-enhanced (DCE)-MRI

Introduction

As already outlined, cardiovascular diseases (CVDs) are the number one killer globally (one third of annual death) [1]. The most severe pathological condition is atherosclerosis (AS) affecting heart and blood vessels. As an early event, endothelial dysfunction is involved in the progression of AS. A functional vascular endothelium supports the beneficial effects of antioxidant, antiinflammatory, anticoagulant and pro-fibrinolytic actions and under normal circumstances a functional endothelium releases nitric oxide (NO) [7]. NO inhibits the adhesion and migration of leukocytes, the migration and proliferation of smooth muscle cells, the aggregation and adhesion of platelets, promotes re-endothelialization and is essential for maintaining vascular tone. Moreover, NO controls vasoreactivity, regulates endothelial cell and tight junction morphology and vascular permeability [8, 9]. Endothelial NO synthase (eNOS, NOS3) synthesizes NO in the endothelium and is a protective factor maintaining vascular integrity [10]. A reduction of NO activity therefore leads to endothelial dysfunction and precedes the development of AS. Gadolinium based blood pool agents were successfully applied in the past to gain insight into the leakiness of the endothelial layer via the altered vascular permeability and albumin as vehicle into the lesion [32, 6]. Phinikaridou and colleagues investigated endothelial damage (endothelial permeability/function vs delayed enhancement) and endothelial-dependent vasodilation to acetylcholine Ach (vasodilation) in the ApoE-/- mouse model of atherosclerosis. Delayed enhancement (30min after contrast agent injection) measurements revealed an increase in vessel wall signal dependent on the progression of AS and further correlated with changes of morphological parameters like widening of cell-cell junctions and changes of endothelial cells indicating an alteration of endothelial permeability. Furthermore, endothelial-dependent vasomotor response was paradoxical twisted to vasoconstriction for the ApoE-/- mice compared to vasodilation of control wild-type mice. Lavin and co-workers investigated vascular permeability and remodeling after injury (denudation) in NOS3-/- knockout and wild-type mice. Delayed enhancement as well as R1 relaxation rate measurements of both mice types showed increased vessel wall signals (increased permeability) compared to sham-operated ani-

mals at an early post-treatment recovery time point (seven days). However, at later time points (15 and 30days) impaired re-endothelialization and neovascularization in the knockout model led to significant higher values compared to the control group (re-endothelialization plus no neovascularization). This clearly highlights the role of NOS3 in re-endothelialization and diminishing the effects of vascular remodeling. Moreover, MRI has also been successfully applied to noninvasively assess impaired vasodilation using nitroglycerine as an endothelial-independent stimuli in patients at risk for coronary artery disease (CAD) [182, 183, 184]. In this work we set out to measure the endothelial barrier function of atherosclerotic rabbits using B-22956/1 an albumin binding agent in combination with NO donor S-nitroso human serum albumin (S-NO-HSA) and DCE-MRI. Furthermore, we tested whether the long-term S-NO-HSA-B22956/1 infusion led to a NO induced vasodilation effect. The project was performed in collaboration with the Clinical Institute of Medical and Chemical Laboratory Diagnostics (Gunter Almer, Harald Mangge, Harald Froehlich), Medical University of Graz, the Institute of Medical Engineering (Rudolf Stollberger), Graz University of Technology, Austria, the Institute of Physiological Chemistry (Gerd Hoerl, Seth Hallstroem), Medical University of Graz, Austria and Bracco Research Centre (Claudia Cabella), Bracco Imaging SpA, Colleretto Giacosa, Italy. The results were presented at the 24th Annual Meeting at the International Society for Magnetic Resonance in Medicine (ISMRM, oral communication; ISMRM Merit Awards: Summa Cum Laude) [185].

Methods:

Contrast agent:

Gadocoletic acid trisodium salt (B22956/1, Bracco Imaging S.p.A.) is an intravascular high affinity serum albumin binding blood pool agent already applied to image neovessel and macrophage density in atherosclerotic rabbits [186, 187]. S-nitroso human serum albumin is a nitric oxide (NO) donor used for NO supplementation shown to prevent endothelial NO synthase (eNOS) uncoupling in rabbits [188].

Animal model:

A total of three male New Zealand White (NZW) rabbits (age:10-11months; body weight:3.5-4.5kg) were used repeatedly in this study. Abdominal aortic atherosclerosis was induced in two rabbits by a combination of balloon catheter denudation and a two month high cholesterol diet (1% cholesterol, western diet, WD). The injury was performed from the iliac bifurcation to the renal artery bifurcation introducing a wedge pressure balloon catheter through the carotid artery. One non-treated rabbit fed a nor-

mal chow diet was used as control. Before starting the imaging procedure the animals were sedated and anesthetized by an i.m. injection of ketamine (10mg/kg), butorphanol (0.1mg/kg) and medetomidine (0.2mg/kg). The second anesthesia cocktail was a combination of xylazine (5mg/kg), acepromazine (0.5mg/kg) and ketamine (20mg/kg). All animal procedures were approved by the Ministry of Science and Research, Austria.

S-NO-HSA(-B22956/1) infusion strategy:

Either 18.5mL of B22956/1 (2mM) pre-incubated with S-NO-HSA (1mM) or B22956/1 (2mM) diluted in sodium chloride were administered intravenously during DCE-MRI. A slow infusion rate of 20mL/h was chosen for all experiments to prevent uncontrolled NO mediated hypotension. To assure contrast agent wash out from the vessel wall, experiments were separated by a whole week. For the injured rabbits the experiments were repeated two-to-three times ending up in a total of five-to-six imaging sessions.

MR imaging:

A dark blood double inversion recovery (DIR) T1-weighted turbo spin echo (T1w-TSE) sequence was used on one selected axial slice for DCE measurements. Scan parameter were TR/TE:600/12ms; NEX/ETL:4/7; matrix:256x176; FOV:120x82.5mm; resolution:0.46x0.46x3mm. To avoid chemical shift artifacts caused by periadventitial fat, a spectral fat saturation pulse was applied. A total of 60 images were acquired with a temporal resolution of 1min1sec. Before long-term infusion a total of five precontrast images were taken for baseline signal averaging. Anatomical fiducial markers were used to retrieve the imaging slice between imaging sessions. All experiments were performed on a human 3Tesla platform (Siemens Magnetom Prisma) using a 15Ch TxRx knee coil.

Data analysis:

Inner and outer vessel wall boundaries of DCE images were manually segmented using ITK-SNAP. To uncover possible NO mediated wall relaxation effects boundaries were used to calculate lumen areas over time. Average vessel wall signal intensities (SI_{wall}) were calculated for each DCE time point. In addition, the normalized wall index (NWI=wall area/total vessel area) was calculated as a measure of wall thickening. The relative signal enhancement c(t) was calculated by subtracting the signal intensity SI(t) at a given time point from the baseline tissue signal intensity SI(0) according to equation [189]: c(t)=(SI(0)-SI(t))/SI(0).

Results:

To get an idea about the plasma concentrations for albumin (HSA), NO and the blood pool agent (BPA, B22956/1) a one-compartment model was simulated (Figure 28) [190]. For that a volume distribution (V_d) of 250ml was assumed which corresponds to a blood volume of a rabbit with a body weight of 4kg. Elimination half-life ($t_{1/2}$) for albumin was selected to be 14h based on recommendations by Liumbruno et al and corresponds to the noted elimination rate constant (k_e) of 0.8e-3min^{-1} [191]. Together with the resorption constant R_0 the plasma concentrations using the formula $c_p(t) = \dfrac{R_0}{k_e V_d}[1 - e^{-k_e t}]$ can be calculated for HSA, NO and BPA.

k_e= 0.8e-3min^{-1}; V_d=2.5dL
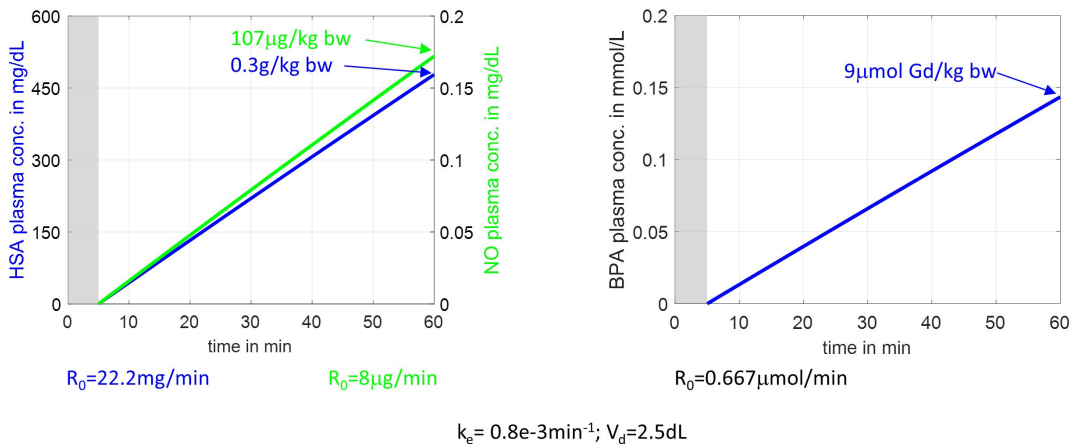
Figure 28: One-compartment model of plasma concentrations for the intravenous (i.v.) continuous infusion of albumin (HSA), nitric oxide (NO) and the blood pool agent (BPA, B22956/1). **Left** curve shows plasma HSA (blue) and NO (green) **Right** curve shows plasma BPA (B22956/1) concentrations over one hour infusion time. V_d, volume distribution in dl; $t_{1/2}$, elimination half-life; k_e, elimination rate constant in min^{-1}; $k_e = ln(2)/t_{1/2}$; R_0, resorption constant in mg/min; 1mM HSA corresponds to 67mg/ml; 1mM NO corresponds to 30μg/ml; 2mM BPA; infusion rate=20ml/h.

It can be seen for all three plasma concentration curves that due to the long elimination half-life no plateau (steady-state condition) is reached within the one our infusion time rather a linear increase can be expected and normalized to the body weight final plasma concentrations are 9μmol Gd/kg for BPA, 107μg NO/kg and 0.3g HSA/kg. Figure 29C shows the relative vessel wall signal enhancement c(t) during the long-term infusion of

S-NO-HSA-B22956/1 (green line) and B22956/1 (blue line), respectively. The relative change in lumen area is outlined in Figure 29B and representative T1w images together with the NWI are illustrated in Figure 29A. The control NZW (CTRL-NZW) and one balloon treated NZW on western diet (BTWD-NZW I) show a normalized wall index (NWI) of 0.5 and the second BTWD-NZW II a NWI of 0.56. To uncover possible endothelial-independent *smooth-muscle cell dependent* NO mediated wall relaxation effects the relative change in lumen area was calculated over time (Figure 29B).
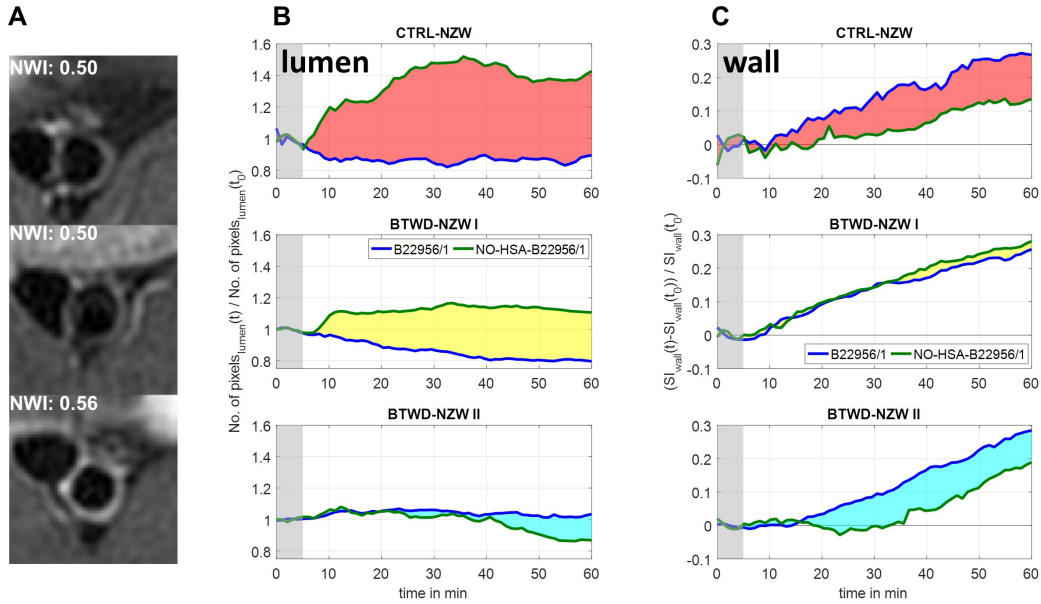
Figure 29: Endothelium-independent NO induced vasomotor response and endothelial barrier function of a control NZW (CTRL-NZW) and two balloon treated NZW on western diet (BTWD-NZW I & II) Top to Bottom. **A** Representative T1w MR images together with the normalized wall index (NWI) for CTRL-NZW, NWI=0.5 and BTWD-NZW I & II; NWI=0.5 & 0.56 respectively. **B** Endothelium-independent NO induced vasomotor response to BPA alone (blue curve, B22956/1) and NO donor BPA compound (green curve, B22956/1-S-NO-HSA). Plotted is the relative change in lumen area as a function of infusion time. Specific vasodilation/vasoconstriction can be observed dependent on the integrity of the arterial wall. **C** Endothelial barrier function to BPA alone (blue curve, B22956/1) and NO donor BPA compound (green curve, B22956/1-S-NO-HSA). Plotted is the relative vessel wall signal enhancement c(t) as a function of infusion time. Specific c(t) can be observed dependent on the interendothelial junction (IEJ) integrity.

For the imaging sessions with the BPA alone (corresponds to the blue curves, B22956/1), the CTRL-NZW and BTWD-NZW I (NWI=0.5) show a final vasoconstriction of about

20%. This process is delayed (plateau at 40minutes) for the AS induced rabbit (BTWD-NZW I). For the rabbit with the NWI of 0.56 (BTWD-NZW II) no change in lumen area could be detected. For the imaging sessions with the NO donor BPA compound (corresponds to the green curves, S-NO-HSA-B22956/1), the CTRL-NZW shows the highest vasodilation of about 40% and approaches a plateau after 30 minutes infusion time. For the balloon treated animal (BTWD-NZW I) an impaired vasodilation can be observed with a plateau of about 20% relaxation (at 10 minutes). For BTWD-NZW II a delayed paradoxical vasoconstriction effect (about 20%) can be observed at rather high NO concentrations (starting at 40minutes). To uncover possible changes of the endothelial barrier function (endothelial permeability) the relative vessel wall signal enhancement c(t) was calculated over time (Figure 29C). For the CTRL-NZW it can be seen that there is a delayed as well as lower final wall enhancement for the NO donor BPA compound (green curve) compared to the BPA alone (blue curve). Compared to the control rabbit, the BTWD-NZW I shows no response to the NO donor (green curve) and the signal enhancement do not differ between the applications (blue vs green curve). For the BTWD-NZW II with the prominent wall thickening the signal behaviour is comparable to the CTRL-NZW with the exception that the whole enhancement process is delayed for both the NO donor BPA compound (green) and BPA alone (blue curve). All discussed investigations were performed under general anesthesia by i.m. injection of medetomidine, butorphanol, ketamine (MBK). This cocktail, in particular medetomidine causes a vasoconstriction as observed from the BPA experiments. Figure 30 shows the effect of the used cocktail compared to a also frequently used one (XAK: xylazine, acepromazine, ketamine) in a control NZW.
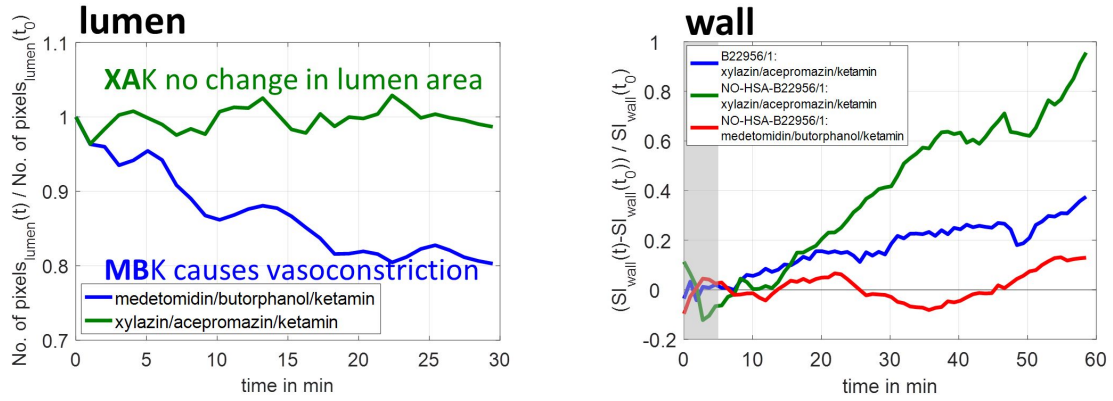
Figure 30: Influence of anesthesia cocktail (MBK vs XAK) on vasoconstriction and endothelial barrier function. **Leftmost** Vasomotor response to MBK vs XAK. Plotted is the relative change in lumen area as a function of measurement time (30minutes). Vasoconstriction is caused by medetomidine (blue curve, about 20% change in lumen area) while vasoconstriction of xylazine is compensated by acepromazine (green curve, no change in lumen area). **Rightmost** Modulated regulation of endothelial barrier function by MVK vs XAK. Plotted is the relative vessel wall signal enhancement c(t) as a function of infusion time. XAK cocktail in combination with the NO donor BPA compound (green curve) causes an increase in signal enhancement whereas the MBK cocktail in combination with the NO donor BPA compound (red curve) causes a decrease in signal enhancement compared to the control condition (BPA without NO donor, blue curve). Results indicate a modulation of the NO control effect on IEJ integrity by anesthesia.

From the leftmost Figure 30 it can be seen that the vasoconstriction effect mediated by xylazine is compensated by acepromazine which acts as a vasodilator and hence no change in lumen area can be expected (green curve) compared to the vasoconstriction effect mediated by medetomidine (blue curve, about 20% change in lumen area). Another interesting effect is that the NO control on IEJ integrity is modulated by the used anesthesia cocktail as can be seen from the rightmost Figure 30. The XAK cocktail in combination with the NO donor BPA compound causes an increase in the signal enhancement (green curve) whereas the MBK cocktail in combination with the NO donor BPA compound causes a decrease in the signal enhancement (red curve) compared to the control condition (BPA without NO donor, blue curve).

Discussion:

In this work, we demonstrated for the first time the feasibility to investigate vascular

permeability (endothelial barrier function) and NO induced endothelium-independent (smooth-muscle cell dependent) vasomotor response of the abdominal aorta in control and balloon denuded rabbits simultaneously. The role of NO in controlling the interendothelial junctions and therefore to regulate the endothelial barrier is discussed quite controversial in literature [9]. NWI is a measure of wall thickening and a promising marker of plaque burden and values above 0.56 have been associated with fibrous cap rupture and intraplaque hemorrhage [192]. As a result, a difference in plaque development between the two AS induced rabbits can be assumed. Given that a delayed wall enhancement (decreased vascular permeability) and vasodilation of the NO donor carrying compound can be observed, a regulation of the endothelial barrier function as well as an NO induced endothelium-independent vasomotor response of the control rabbits' vessel is assumable. In detail, this lets assume a decrease in vascular endothelial permeability mediated by the NO carrying compound possible triggering a strengthening of the interendothelial junction (IEJ) integrity. Vasoconstriction is expected for the BPA sessions as this is an effect of the administered anesthesia cocktail (medetomidine, butorphanol, ketamine). For the balloon treated NZW I (BTWD-NZW I) no differences in wall enhancement (loss of IEJ integrity) but an NO triggered impaired relaxation of the artery can be observed, indicating a vascular damage with endothelial dysfunction but existing vasorelaxation of smooth muscle cells. BTWD-NZW II with a prominent thickening of the wall (NWI=0.56) shows a reconstituted delayed endothelial function and contraction of the artery, assuming advanced plaque burden with possible endothelial regrowth and paradoxical NO induced vasoconstriction. In detail, it seems that the possible reconstituted but delayed endothelial barrier function regulates a decrease in vascular endothelial permeability in response to NO. Recent results also indicate a modulation of the NO control effect on IEJ integrity by the applied anesthesia cocktail (XAK vs MBK). XAK in combination with the NO donor causes an increase in vascular endothelial permeability corresponding to a weakening of the IEJ integrity whereas MBK in combination with the NO donor causes a decrease in vascular endothelial permeability corresponding to a strengthening of the IEJ integrity. To conclude, our work indicate that the extend of impaired vasodilation (vasoconstriction) as well as IEJ integrity control by NO is associated with the degree of plaque burden. Future work will investigate the influence of plaque progression on endothelial barrier regulation and vasomotion which may help to predict the formation of atherosclerotic plaques. The found influence of the anesthesia on IEJ integrity has also to be addressed and investigated in more detail.

5.3 Atherosclerotic plaque MR imaging using (super)paramagnetic blood pool agents

Introduction

As already outlined, atherosclerosis (AS) is a chronic inflammatory disease of the large arteries, ending in clinical manifestations. Gadolinium chelates and iron oxide probes represent the two major families of MR contrast agents, both successfully applied in atherosclerotic plaque MRI. Whereas the latter one is recognized as safe, a possible association between nephrogenic systemic fibrosis and gadolinium based agents is supposed [193]. To reveal information on the molecular level (e.g. binding affinity of a contrast agent to certain plaque features), gadolinium based blood pool agents were successfully applied in the past for fibrous plaque detection via the altered vascular permeability and albumin as vehicle into the lesion [194]. Meding and co-workers showed that Gadofluorine (Schering AG, Germany), a gadolinium based blood pool agent, exploits the injured regions to penetrate the vessel wall and binds to several extracellular matrix constituents within the extracellular space of the fibrous plaque. Gadofluorine is a Gd-DO3A derivative that forms micelles (5nm) in an aqueous solution whereas in plasma binding to albumin (ratio 1:1) imparts blood pool properties with a long circulation half-life ($\sim$ 10h in rabbits). Beside fibrous plaque imaging it was also successfully applied for early plaque detection, tracking plaque progression/regression and its accumulation is associated with inflammation and neovascularization [195, 30, 196, 197]. Moreover, B22956/1 (Gadocoletic acid trisodium salt, Bracco Imaging S.p.A.) another intravascular high affinity serum albumin binding blood pool agent (see *Chapter 5.2*) was also applied to image neovessel and macrophage density in atherosclerotic rabbits [186, 187]. Cornily and colleagues could show that a signal enhancement at an early time point (8min post injection) correlates with neovessel density whereas the signal accumulation at a later time point (2h post injection) highly correlates with macrophage density. A graphical representation of the found signal enhancement values (temporal resolution 8minutes) from the Cornily paper (Figure 31A) between an unspecific agent (Gd-DTPA) and the B22956/1 clearly depicts the stronger plaque enhancement as well as prolonged imaging time window for the proposed blood pool agent. Moreover, our experiments (Figure 31B) also confirm the behaviour of the agent in plaque tissue (LCC, left common carotid artery) and additionally provide information of the accumulation in a healthy vessel wall tissue (RCC, left common carotid artery). Wash-in and wash-out effects from both healthy and plaque tissue are accelerated for the unspecific agent compared to the blood

pool agent.
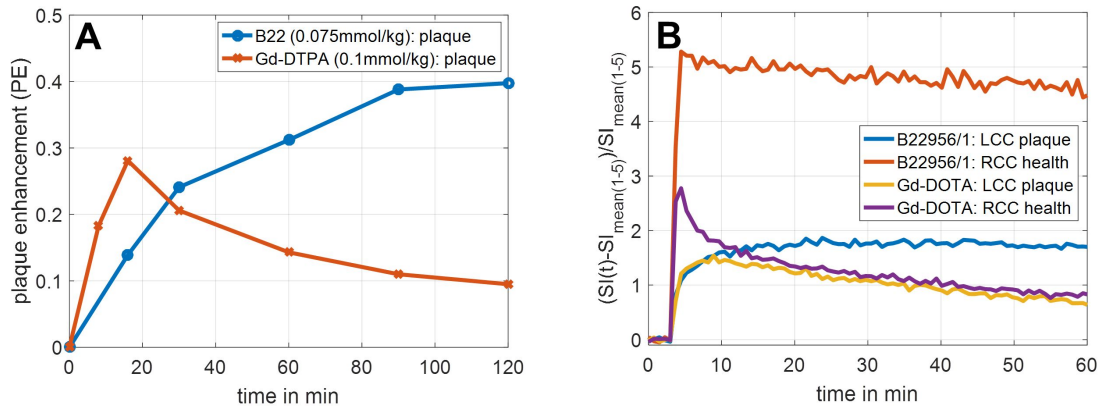
Figure 31: Plaque signal enhancement of B22956/1 vs an unspecific agent. **A** Plaque enhancement (PE) as a function of time. MRI parameter: 2D DB-T1w-TSE, TR/TE=800/5.3ms; temporal resolution=8minutes; Data of Ref. [186]. **B** Relative vessel wall signal enhancement as a function of time. MRI parameter: 2D DB-T1w-TSE, TR/TE=250/9.7ms; bolus:0.5ml/s; 0.1mmol Gd/kg; temporal resolution=45sec; The data clearly depict the stronger plaque enhancement as well as prolonged imaging time window for the proposed blood pool agent when compared to an unspecific one.

However, because of a possible association between nephrogenic systemic fibrosis and gadolinium based agents, iron oxide nanoparticles represent a valuable alternative for contrast enhanced MRI [193]. Among the diversity of these nanoconstructs, ultrasmall superparamagnetic iron oxides (USPIOs) had been successfully applied in passively tracing of atherosclerotic inflammation and as functionalized probes to uncover early markers of inflammation (VCAM-1, P-selectin, E-selectin) in models of atherosclerosis as discussed in *Chapter 5.1*. A fairly high concentration of USPIOs was used (up to 1mmol Fe/kg body weight) in the past to allow for passive targeting of inflammation in animal models of atherosclerosis. In contrast, targeted particles at rather low concentrations (in the range of 100μmol Fe/kg body weight) allow imaging of endothelial markers and also reduce effects of unwanted unspecific targeting. As outlined in *Chapter 5.1* the coating material (dextran, carboxy-dextran etc.) of the iron oxide core directly effects the behaviour of the particle like blood half-life or distribution pattern in atherosclerotic lesions. An interesting approach proposed by Xie et al and Quan et al was the use of albumin coated iron oxide nanoparticles for efficient cell labeling or as drug delivery vehicle for cancer therapy, respectively [198, 199]. The purpose of the investigation was to explore whether plaque imaging by Gadofluorine P can be translated to BSA coated

ultrasmall superparamagnetic iron oxide nanoparticles (USPIOs) in a mouse and rabbit model of AS. The findings presented in the following section were performed in collaboration with the Clinical Institute of Medical and Chemical Laboratory Diagnostics (Gunter Almer, Harald Mangge), Medical University of Graz, the Institute of Medical Engineering (Rudolf Stollberger), Graz University of Technology, Austria, the Institute of Biophysics (Ruth Prassl, Daniela Frascione, Caroline Vonach), Medical University of Graz, Austria. These results were also presented at the 28-30th Annual Meetings at the European Society for Magnetic Resonance in Medicine and Biology (ESMRMB, clinical review poster presentations) [200, 201, 202].

Methods:

Contrast agents:

Two agents were used for imaging aortic atherosclerosis. Gadofluorine P (invivoContrast) a daughter product of Gadofluorine M (Schering AG, Germany) with improved tolerability is a macrocyclic, amphiphilic, low molecular weight (1322.17g/mol) blood pool agent with a blood half-life of about 10 hours in rabbits. BSA coated USPIOs (nanomag-D-spio BSA, micromod Partikeltechnologie GmbH) with a hydrodynamic diameter of 20nm and a protein binding capacity of 1.5μg albumin/mg particle ($\sim$ 1:1 ratio).

Animal model:

A total of five rabbits (age at MR experiment:20 ± 7months; body weight:4.5 ± 1kg) were used for Gadofluorine P imaging. In detail, two New Zealand White (NZW) rabbits, two Watanabe heritable hyperlipidemic (WHHL) rabbits and one wild type (WT) rabbit were used. One NZW and WHHL were fed a high cholesterol diet (1% cholesterol, western diet, WD) for six months to induce aortic atherosclerosis or to augment plaque progression, respectively. The remaining three rabbits were fed a normal chow diet. A total of two rabbits were used for BSA-USPIO imaging. In detail, one NZW on normal chow diet (age at MR experiment: 15month; body weight:5.8kg) and one NZW on WD (1% cholesterol; age at MR experiment: 40month; body weight: 4.5kg) for eight months. In addition, two ApoE-/- mice were also used for BSA-USPIO imaging (advanced age+WD). Before starting the imaging procedure rabbits were sedated and anesthetized by an i.m. injection of ketamine (10mg/kg), butorphanol (0.1mg/kg) and medetomidine (0.2mg/kg). ApoE-/- mice were anesthetized using isoflurane inhalation

1-2%. All animal procedures were approved by the Ministry of Science and Research, Austria.

MR imaging:

All rabbits underwent a baseline and 24h post contrast measurement. Equivalent doses of 50μmol/kg body weight Gadofluorine P (n=5) or 40-50μmol Fe/kg body weight (n=2) were administered intravenously prior to the 24h post scan. Axial images of the thoracic aorta were acquired in the supine position using a multislice 2D dark blood T1-weighted turbo spin echo (T1w DB-TSE) sequence (n=5) or a 2D multiecho gradient echo (me-GRE) sequence (n=2). For mouse MRI (n=2) 50 and 350μmol Fe/kg body weight of BSA-USPIOs were administered i.v. prior to post contrast measurement time points (up to 12days). To improve wall-lumen delineation, spatial saturation bands inferior and superior to the imaging plane ensured suppression of signal from flowing blood. To avoid chemical shift artifacts caused by periadventitial fat, a spectral fat saturation pulse was applied. Sequence parameter were in detail: T1w DB-TSE: TR/TE= 600/9.7ms; NEX= 2; TA= 8min; matrix= 312x384; FOV= 98x120mm^2; resolution= 0.31x0.31mm^2; THK= 3mm. meGRE: TR= 1400ms; TE= 4.92, 12.3, 19.7,27.1, 34.4ms; FA= 25°; NEX= 2; TA= 28min; matrix= 384x384; FOV= 120x120mm^2; resolution= 0.31x0.31^2; THK= 3mm. 2D-FLASH for mouse: TR/TE= 700/7.59ms; FA=50°; NEX= 5; TA= 23min; matrix= 384x384; FOV= 60x60mm^2; resolution= 0.156x0.156^2;THK= 1mm. All experiments were performed on a human 3Tesla platform (Siemens TimTrio Magnetom) using an eight channel multifunctional coil (NORAS MRI products GmbH) for rabbits and a dedicated volume coil (quadrature detector 35mm inner-diameter, Rapid Biomedical) for mice measurements.

Data analysis:

The inner and outer boundaries of the vessel wall in the T1w and meGRE images (pre and post contrast) were manually segmented using an in-house built Matlab script (The MathWorks). For the T1w sequence, beside the calculation of the wall signal intensities (SI$_{wall}$), region-of-interests (ROIs) in the paraspinal muscle adjacent to the aorta (SI$_{muscle}$) were delineated. The relative signal intensity rSI (SI$_{wall}$/SI$_{muscle}$) as well as the change in relative signal intensity (rSI$_{change}$=rSI$_{post}$-rSI$_{pre}$) was calculated. For the meGRE measurements, a Levenberg-Marquardt nonlinear least squares fitting algorithm was applied to $SI(T_E) = S_0 e^{T_E/T_2^*}$ for calculating T_2^* relaxation times voxel-wise (two-parameter fitting routine) and to generate quantitative maps. The change in T_2^*

relaxation times ($T^*_{2\,change} = 1 - T^*_{2\,post}/T^*_{2\,pre}$) was also determined.

Results:

Figure 32 shows the Gadofluorine P enhanced MRI results for rabbits of different strains (NZW, WHHL, wild-type WT) and diets (normal chow diet, 1% cholesterol diet). The experiments revealed for the WT/NZW/WHHL a change in rSI of 2/4/30% in the normal chow diet group and a change in rSI for NZW/WHHL of 30/75% in the WD group.
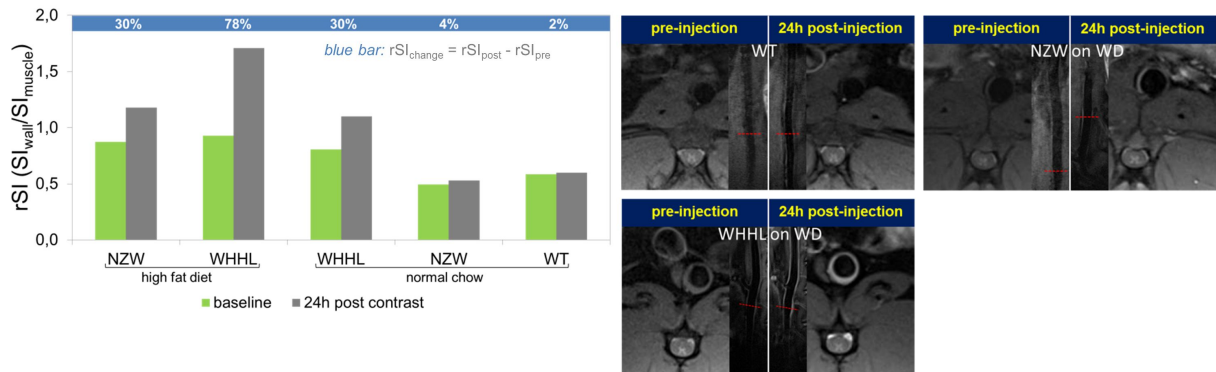
Figure 32: Gadofluorine P enhanced MRI of the descending thoracic aorta for rabbits of different strains (WHHL, NZW, WT) and diets (normal chow vs high fat diet). **Left** Bar plot displays semi-quantitative rSI of rabbit vessel walls at baseline and 24h post contrast agent injection time point; relative signal intensity, rSI= SI_{wall}/SI_{muscle}; blue bar: change in rSI, rSI_{change}= rSI_{post}-rSI_{pre}; rSI_{change} of WT, NZW, WHHL on normal chow diet: 2, 4, 30%; rSI_{change} of NZW, WHHL on high fat diet: 30, 75%. **Right** Representative 2D T1w-DB-TSE images of a WT on normal chow diet, NZW and WHHL on WD for the baseline and post injection time point. The degree of signal enhancement clearly differs dependent on the strain/diet condition.

Figure 33 shows the results of the BSA-USPIO experiments for two NZW rabbits on normal chow and high fat diet, respectively. The data revealed for the NZW on normal chow no change in relaxation time (4%) whereas the NZW on WD showed a 16% shortening of the T^*_2 relaxation time.
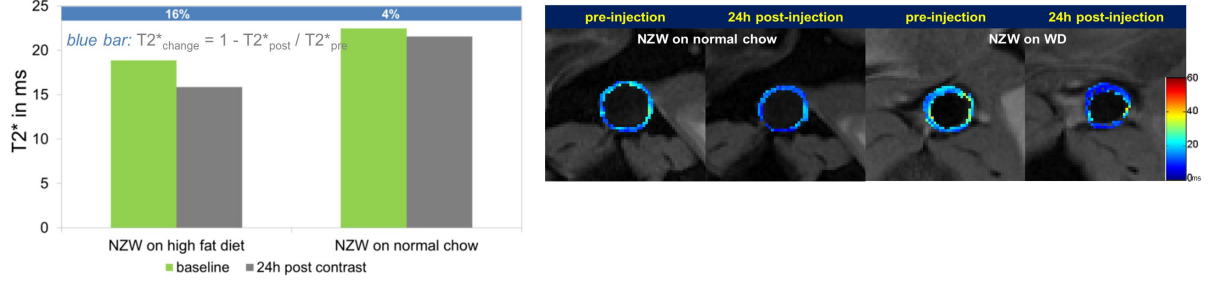
Figure 33: BSA-USPIO enhanced MRI of the descending thoracic aorta for NZWs on a normal chow diet and high fat diet, respectively. **Left** Bar plot displays T_2^* relaxation time values of the rabbit vessel walls at baseline and 24h post contrast agent injection time point; blue bar: change in T_2^*, $T_{2\,change}^* = 1 - T_{2\,post}^*/T_{2\,pre}^*$; $T_{2\,change}^*$ of NZW on normal chow diet 4% and NZW on high fat diet 16%. **Right** Representative meGRE images (shortest echo time) of both animals for the baseline and post injection time point with superimposed T_2^* maps. The degree of T_2^* shortening clearly differs between the two diet condition.

In addition to the rabbit experiments BSA-USPIO enhanced MRI of two ApoE-/- mice was performed and imaging was repeated up to twelve days after contrast agent administration (Figure 34). Gross qualitative visual inspections of both experiments clearly showed a strong signal drop of the pathological transformed vessel wall for the high dose case with full cancellation of the whole wall for the total examination period. In comparison to that, no accumulation of BSA-USPIOs in the thickened arterial wall was found for the low dose case.
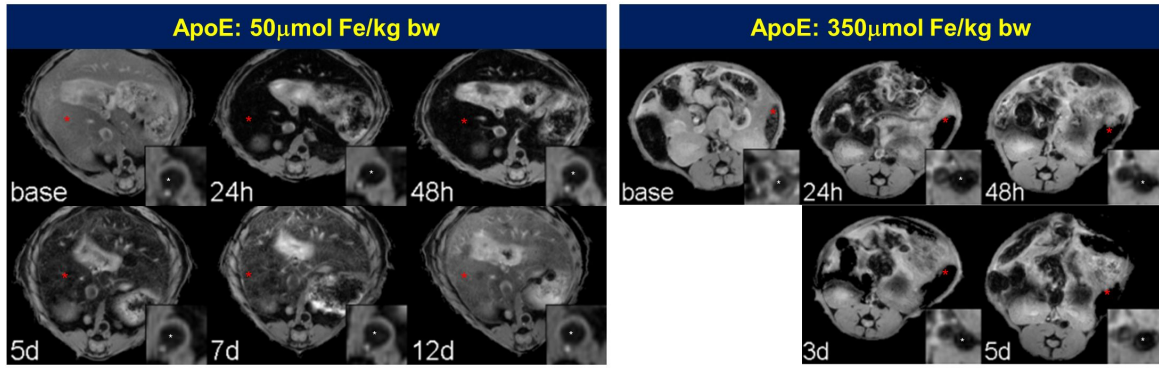
Figure 34: BSA-USPIO enhanced MRI of the descending thoracic aorta for two ApoE-/- mice fed a high fat diet (advanced age + WD). MR imaging was repeated up to twelve days after contrast agent administration. Gross qualitative visual inspections of both experiments clearly indicate a strong signal drop of the pathological transformed vessel wall for the high dose case (350μmol Fe/kg body weight) with full cancellation of the whole wall for the total examination period (5days). In comparison to that, no accumulation of BSA-USPIOs in the thickened arterial wall can be seen for the low dose 50μmol Fe/kg body weight case.

Discussion:

Gadofluorine P enhanced MRI clearly reveals an accumulation of the blood pool agent in all cases of pathological transformed vessel walls. Furthermore, the accumulation of the contrast agent in injured walls is animal model and diet dependent. WHHL without dietary triggering exhibit similar enhancement behaviour as do NZW on WD. The strongest enhancement was found for the WHHL on WD. As already outlined in *Chapter 2.1*, NZWs require a stimulus (dietary or dietary plus mechanical trigger) to develop atherosclerotic lesions compared to the WHHL strain which spontaneously generates lesions and in case of an additional dietary trigger plaque progression is accelerated. That implies more advanced lesions for the WHHL on WD and a similar plaque formation for WHHL on normal chow and NZW on WD. Intact healthy vessel walls can be expected for the control animals as there was no visible accumulation of the agent on the 24h post contrast images. BSA-USPIO enhanced plaque MRI as a proposed surrogate marker for Gadofluorine P imaging seems feasible but lack detailed evaluation because of the small animal size. The uptake of the agent in the wall may be mediated by the particles albumin surface indicating an active lesion with increased vascular permeability. To test a higher agent concentration additional experiments were performed on ApoE-/- mice with advanced age and fed a high fat diet. The low dose injection (clinical range) failed to reveal any accumulation in the descending aortic wall while the high dose injection

(seven fold) showed a full cancellation of the wall on the MR images for the total examination period. That implies stabilized advanced plaques with an altered endothelial barrier function but still vulnerable for passive targeting of inflammation by using a fairly high iron oxide dosage.

6 Outlook

Cardiovascular magnetic resonance vessel wall diffusion anisotropy in carotid arteries:
The major finding of the presented data was the significant linear relationship between fractional anisotropy (FA) and volunteers age. To get a more complete picture of ongoing processes in the vessel wall with advancing age postmortem carotid arteries (all age groups healthy and diseased) provided by the Institute of Pathology (Prof. Johannes Haybaeck, Medical University of Graz) will be imaged at high resolution. In addition, in vivo measurements of healthy volunteers will be continued to increase the control cohort and patients from the Stroke Unit (Prof. Kurt Niederkorn, Division of General Neurology, Medical University of Graz) will be recruited to establish a cohort of participants suffering from atherosclerotic lesions. These tasks are already approved by the institutional review board (IRB; Medical University of Graz). In addition to MRI, histopathology, immunohistochemistry as well as microscopy (second harmonic generation (SHG) for collagen and two-photon-excited fluorescence (2PEF) for elastin) is planned for the postmortem tissue samples but has to be discussed with the corresponding experts. Taken all these information together (in vivo & postmortem) questions will be answered whether lesion formation lead to specific diffusion anisotropy patterns within the vessel wall and whether the found relationship of age and FA will survive. The overall aim is to find a parameter that allows a prediction of the cardiovascular fitness and risk stratification of possible future cardiovascular events.

Nanoparticle enhanced plaque MR imaging / molecular imaging:
The simultaneous measurement of the endothelial barrier function (interendothelial junction integrity) and nitric oxide induced endothelium-independent (smooth-muscle cell dependent) vasomotor response of the abdominal aorta in rabbits was shown by the use of a nitric oxide donor blood pool agent compound. In another study bovine serum albumin coated iron oxides were used to to gain insight into the leakiness of the endothelial layer via the altered vascular permeability and albumin as vehicle into the lesion. Findings are promising but lack detailed evaluation so far because of the small animal sample size. Again, these investigations aimed at identifying alterations of vascular permeability and function as endothelial dysfunction is a marker of plaque progression, destabilization and precedes the development of atherosclerosis. In both cases more animals and experiments are required to confirm the exciting findings and

allow statistical analysis. The identification of a nanoparticle that is able to uncover early wall remodeling processes is of valuable interest as can be noticed by the bunch of publications in the field of molecular imaging. Challenges in the design and development of an appropriate nanoparticle include its property to be biodegradable, biocompatible, nontoxic, nonimmunogenic and the ability to load it with imaging agents and/or therapeutic drugs.

Balloon catheter device for use in an aorta of a rabbit or a human being:

The pressure controlled balloon injury device clearly showed its superiority to the manual technique keeping a prescribed balloon inflation pressure during the passage of the catheter. Current steps include the preclinical evaluation of the prototype device in rabbits within the prolonged work package of the EU project NanoAthero as well as a patent cooperation treaty (PCT) application (date: 25th of August, 2017). The evaluation procedure is a two step process and consists of the analysis of balloon denuded aorta samples which are drawn I) immediately after the mechanical intervention (days) and II) after the generation of atherosclerotic lesions (months). Experiments to assess functional parameters like endothelium / smooth muscle cell dependent vasomotion (response to norepinephrine, acetylcholine) by myography as well as tissue morphology by histology will be performed to compare the pressure controlled balloon injury device with the conventional technique. Final expectations are to find immediate effects of pressure variations on the wall integrity as well as long-term effects on homogeneity and reproducibility of lesion development. In parallel to that tasks and with the support of the *BioNanoNet Forschungsgesellschaft mbH (Andreas Falk)* national funding opportunities are explored and a partner company has already been found for the realization and implementation of a product device. Moreover, a translational application of a possible pressure controlled balloon thromboembolectomy is agreed and in a first step will be implemented to monitor balloon pressure behavior during surgery between professionals and doctors-in-training. For that, a wireless communication between the pressure sensor balloon catheter unit and a receiver unit (computer) will be installed to satisfy (hygiene) health care standards and regulations.

7 List of Publications

P. Opriessnig, M. Mangge, R. Stollberger, H. Deutschmann, G Reishofer; In vivo cardiovascular magnetic resonance of 2D vessel wall diffusion anisotropy in carotid arteries. J Cardiovasc Magn Reson 2017, 18:81.

P. Opriessnig, G. Almer, H. Froehlich, C. Cabella, R. Stollberger, S. Hallstroem, G. Hoerl, H. Mangge; Evaluation of endothelial barrier function in atherosclerosis induced rabbits using S-nitroso human serum albumin (S-NO-HSA) - blood pool agent compound and dynamic contrast-enhanced (DCE)-MRI, ISMRM Proceedings, 2016, Oral Communication (ISMRM Merit Award: summa cum laude)

P. Opriessnig, R. Stollberger, H. Mangge, R. Prassl, Liposome nanoparticles for diagnostic applications In: Samad, A; Beg, S; Nazish, I; editors(s). Liposomal Delivery Systems: Advances and Challenges. Panacea Biotec Ltd., India: Future Science Ltd; p. 188-203. 2016 (ISBN: 978-1-910419-08-3)

P. Opriessnig, H. Mangge, R. Stollberger, D.A. Porter, H. Deutschmann, G. Reishofer; In vivo measurement of vessel wall diffusion anisotropy in carotid arteries, ISMRM Proceedings, 2015, Oral Communication

G. Almer, P. Opriessnig, R. Prassl, and H. Mangge, Anti-inammatory mediators for molecular imaging of atherosclerosis, European Journal of Nanomedicine, vol. 6, no. 2, 2014

P. Opriessnig, G. Almer, R. Prassl, R. Stollberger, H. Mangge; BSA-USPIO enhanced vessel wall MRI in a rabbit and mouse model of atherosclerosis AAS Proceedings, 2014

P. Opriessnig, G. Almer, C. Vonach, R. Prassl, H. Mangge, R. Stollberger; USPIO- vs. stealh magnetic liposomes sML- enhanced atherosclerotic plaque MRI, ESMRMB Proceedings, 2013, Traditional Poster

P. Opriessnig, G. Almer, D. Frascione, R. Prassl, H. Mangge, R. Stollberger; BSA-USPIO enhanced atherosclerotic plaque MRI: A surrogate complex to mimic Gadofluorine enhanced fibrous plaque detection?, ESMRMB Proceedings, 2012, Traditional Poster

D. Frascione, C. Diwoky, G. Almer, P. Opriessnig, C. Vonach, K. Gradauer, G. Leitinger, H. Mangge, R. Stollberger, and R. Prassl, Ultrasmall superparamagnetic iron oxide

(USPIO)-based liposomes as magnetic resonance imaging probes, Int J Nanomedicine, vol. 7, pp. 2349-2359, 2012

M. Kraiger, P. Martirosian, P. Opriessnig, F. Eibofner, H. Rempp, M. Hofer, F. Schick, and R. Stollberger, A fully automated trabecular bone structural analysis tool based on T2* -weighted magnetic resonance imaging, Comput Med Imaging Graph, vol. 36, pp. 85-94, 2012

P. Opriessnig, G. Almer, D. Frascione, R. Prassl, H. Mangge, R. Stollberger; Cytokine functionalized USPIOs: suitable targeting sequences for molecular MR imaging of atherosclerotic vessel walls? ESMRMB Proceedings, 2011, Oral Communication

M. Karbiener, C. Neuhold, P. Opriessnig, A. Prokesch, J. G. Bogner-Strauss, and M. Scheideler, Microrna-30c promotes human adipocyte differentiation and corepresses pai-1 and alk2, RNA Biol, vol. 8, no. 5, pp. 850-860, 2011

M. Karbiener, C. Fischer, S. Nowitsch, P. Opriessnig, C. Papak, G. Ailhaud, C. Dani, E.-Z. Amri, and M. Scheideler, microrna mir-27b impairs human adipocyte differentiation and targets ppargamma, Biochem Biophys Res Commun, vol. 390, pp. 247-251, 2009

Patent
Title: Balloon catheter device for use in an aorta of a rabbit or a human being.
PCT application number: PCT/EP2017/071300
Date of receipt: 24th of August, 2017
Receiving Office: European Patent Office, The Hague

8 Bibliography

[1] H. O. World and W. H. Organization, *Global Status Report on Noncommunicable Diseases 2014*. WORLD HEALTH ORGN, 2015.

[2] A. J. Lusis, "Atherosclerosis.," *Nature*, vol. 407, pp. 233–241, Sept. 2000.

[3] F. Wiesmann, S. E. Petersen, P. M. Leeson, J. M. Francis, M. D. Robson, Q. Wang, R. Choudhury, K. M. Channon, and S. Neubauer, "Global impairment of brachial, carotid, and aortic vascular function in young smokers: direct quantification by high-resolution magnetic resonance imaging.," *Journal of the American College of Cardiology*, vol. 44, pp. 2056–2064, Nov. 2004.

[4] Y. Xu, H. Arai, T. Murayama, T. Kita, and M. Yokode, "Hypercholesterolemia contributes to the development of atherosclerosis and vascular remodeling by recruiting bone marrow-derived cells in cuff-induced vascular injury.," *Biochemical and biophysical research communications*, vol. 363, pp. 782–787, Nov. 2007.

[5] M. J. Jaervisalo, M. Raitakari, J. O. Toikka, A. Putto-Laurila, R. Rontu, S. Laine, T. Lehtimaeki, T. Roennemaa, J. Viikari, and O. T. Raitakari, "Endothelial dysfunction and increased arterial intima-media thickness in children with type 1 diabetes.," *Circulation*, vol. 109, pp. 1750–1755, Apr. 2004.

[6] B. Lavin, A. Phinikaridou, S. Lorrio, C. Zaragoza, and R. M. Botnar, "Monitoring vascular permeability and remodeling after endothelial injury in a murine model using a magnetic resonance albumin-binding contrast agent.," *Circulation. Cardiovascular imaging*, vol. 8, Apr. 2015.

[7] J. Davignon and P. Ganz, "Role of endothelial dysfunction in atherosclerosis.," *Circulation*, vol. 109, pp. III27–III32, June 2004.

[8] S. Thibeault, Y. Rautureau, M. Oubaha, D. Faubert, B. C. Wilkes, C. Delisle, and J.-P. Gratton, "S-nitrosylation of beta-catenin by enos-derived no promotes vegf-induced endothelial cell permeability.," *Molecular cell*, vol. 39, pp. 468–476, Aug. 2010.

[9] D. Predescu, S. Predescu, J. Shimizu, K. Miyawaki-Shimizu, and A. B. Malik, "Constitutive enos-derived nitric oxide is a determinant of endothelial junctional integrity.," *American journal of physiology. Lung cellular and molecular physiology*, vol. 289, pp. L371–L381, Sept. 2005.

[10] D. N. Atochin and P. L. Huang, "Role of endothelial nitric oxide in cerebrovascular regulation.," *Current pharmaceutical biotechnology*, vol. 12, pp. 1334–1342, Sept. 2011.

[11] Z. M. Dong, S. M. Chapman, A. A. Brown, P. S. Frenette, R. O. Hynes, and D. D. Wagner, "The combined role of p- and e-selectins in atherosclerosis.," *The Journal of clinical investigation*, vol. 102, pp. 145–152, July 1998.

[12] A. Ala, A. Dhillon, and H. Hodgson, "Role of cell adhesion molecules in leukocyte recruitment in the liver and gut," *International Journal of Experimental Pathology*, vol. 84, pp. 1–16, apr 2003.

[13] R. Kleemann, S. Zadelaar, and T. Kooistra, "Cytokines and atherosclerosis: A comprehensive review of studies in mice," *Cardiovascular Research*, vol. 79, no. 3, pp. 360–376, 2008.

[14] Z. Mallat, C. Heymes, J. Ohan, E. Faggin, G. Lesèche, G. Lese, and A. Tedgui, "Expression of Interleukin-10 in Advanced Human," pp. 611–616, 1999.

[15] K. Nishihira, T. Imamura, A. Yamashita, K. Hatakeyama, Y. Shibata, Y. Nagatomo, H. Date, T. Kita, T. Eto, and Y. Asada, "Increased expression of interleukin-10 in unstable plaque obtained by directional coronary atherectomy," *European Heart Journal*, vol. 27, no. 14, pp. 1685–1689, 2006.

[16] R. Virmani, F. D. Kolodgie, A. P. Burke, A. Farb, and S. M. Schwartz, "Lessons from sudden coronary death: a comprehensive morphological classification scheme for atherosclerotic lesions.," *Arteriosclerosis, thrombosis, and vascular biology*, vol. 20, pp. 1262–1275, May 2000.

[17] T. Leiner, S. Gerretsen, R. Botnar, E. Lutgens, V. Cappendijk, E. Kooi, and J. van Engelshoven, "Magnetic resonance imaging of atherosclerosis," *European Radiology*, vol. 15, no. 6, pp. 1087–1099, 2005.

[18] A. Trion and A. van der Laarse, "Vascular smooth muscle cells and calcification in atherosclerosis.," *American heart journal*, vol. 147, pp. 808–814, May 2004.

[19] R. Ross, "Atherosclerosis–an inflammatory disease.," *The New England journal of medicine*, vol. 340, pp. 115–126, Jan. 1999.

[20] P. R. Moreno, K.-R. Purushothaman, M. Sirol, A. P. Levy, and V. Fuster, "Neovascularization in human atherosclerosis.," *Circulation*, vol. 113, pp. 2245–2252, May 2006.

[21] E. Groszek and S. M. Grundy, "The possible role of the arterial microcirculation in the pathogenesis of atherosclerosis.," *Journal of chronic diseases*, vol. 33, pp. 679–684, 1980.

[22] H. M. Kwon, G. Sangiorgi, E. L. Ritman, C. McKenna, D. R. Holmes, R. S. Schwartz, and A. Lerman, "Enhanced coronary vasa vasorum neovascularization in experimental hypercholesterolemia.," *The Journal of clinical investigation*, vol. 101, pp. 1551–1556, Apr. 1998.

[23] W. S. Kerwin, M. Oikawa, C. Yuan, G. P. Jarvik, and T. S. Hatsukami, "Mr imaging of adventitial vasa vasorum in carotid atherosclerosis.," *Magnetic resonance in medicine*, vol. 59, pp. 507–514, Mar. 2008.

[24] M. Kumamoto, Y. Nakashima, and K. Sueishi, "Intimal neovascularization in human coronary atherosclerosis: its origin and pathophysiological significance.," *Human pathology*, vol. 26, pp. 450–456, Apr. 1995.

[25] G. Pasterkamp, Z. S. Galis, and D. P. V. de Kleijn, "Expansive arterial remodeling: location, location, location.," *Arteriosclerosis, thrombosis, and vascular biology*, vol. 24, pp. 650–657, Apr. 2004.

[26] P. Libby, M. DiCarli, and R. Weissleder, "The vascular biology of atherosclerosis and imaging targets.," *Journal of nuclear medicine : official publication, Society of Nuclear Medicine*, vol. 51 Suppl 1, pp. 33S–37S, May 2010.

[27] T. Saam, H. R. Underhill, B. Chu, N. Takaya, J. Cai, N. L. Polissar, C. Yuan, and T. S. Hatsukami, "Prevalence of american heart association type vi carotid atherosclerotic lesions identified by magnetic resonance imaging for different levels of stenosis as measured by duplex ultrasound.," *J Am Coll Cardiol*, vol. 51, pp. 1014–1021, Mar 2008.

[28] A. F. Drew, *Atherosclerosis*. Springer Nature, nov 2000.

[29] G. S. Getz and C. A. Reardon, "Animal models of atherosclerosis.," *Arteriosclerosis, thrombosis, and vascular biology*, vol. 32, pp. 1104–1115, May 2012.

[30] J. Zheng, D. R. Abendschein, R. J. Okamoto, D. Yang, K. S. McCommis, B. Misselwitz, R. J. Gropler, and D. Tang, "Mri-based biomechanical imaging: initial study on early plaque progression and vessel remodeling.," *Magnetic resonance imaging*, vol. 27, pp. 1309–1318, Dec. 2009.

[31] M. E. Lobatto, Z. A. Fayad, S. Silvera, E. Vucic, C. Calcagno, V. Mani, S. D. Dickson, K. Nicolay, M. Banciu, R. M. Schiffelers, J. M. Metselaar, L. van Bloois, H.-S. Wu, J. T. Fallon, J. H. Rudd, V. Fuster, E. A. Fisher, G. Storm, and W. J. M. Mulder, "Multimodal clinical imaging to longitudinally assess a nanomedical anti-inflammatory treatment in experimental atherosclerosis.," *Molecular pharmaceutics*, vol. 7, pp. 2020–2029, Dec. 2010.

[32] A. Phinikaridou, M. E. Andia, A. Protti, A. Indermuehle, A. Shah, A. Smith, A. Warley, and R. M. Botnar, "Noninvasive magnetic resonance imaging evaluation of endothelial permeability in murine atherosclerosis using an albumin-binding contrast agent.," *Circulation*, vol. 126, pp. 707–719, Aug. 2012.

[33] W. Y, "Studies on characteristics of spontaneously hyperlipemic rabbits and development of the strain with such property.," *Bull Azabu Vet Coll.*, no. 2, p. 99â124, 1977.

[34] Y. Watanabe, "Serial inbreeding of rabbits with hereditary hyperlipidemia (whhl-rabbit).," *Atherosclerosis*, vol. 36, pp. 261–268, June 1980.

[35] M. Shiomi and T. Ito, "The watanabe heritable hyperlipidemic (WHHL) rabbit, its characteristics and history of development: A tribute to the late dr. yoshio watanabe," *Atherosclerosis*, vol. 207, pp. 1–7, nov 2009.

[36] A. S. Plump, J. D. Smith, T. Hayek, K. Aalto-Setaelae, A. Walsh, J. G. Verstuyft, E. M. Rubin, and J. L. Breslow, "Severe hypercholesterolemia and atherosclerosis in apolipoprotein e-deficient mice created by homologous recombination in es cells.," *Cell*, vol. 71, pp. 343–353, Oct. 1992.

[37] S. H. Zhang, R. L. Reddick, J. A. Piedrahita, and N. Maeda, "Spontaneous hypercholesterolemia and arterial lesions in mice lacking apolipoprotein e.," *Science (New York, N.Y.)*, vol. 258, pp. 468–471, Oct. 1992.

[38] Y. Nakashima, A. S. Plump, E. W. Raines, J. L. Breslow, and R. Ross, "Apoe-deficient mice develop lesions of all phases of atherosclerosis throughout the arterial tree.," *Arteriosclerosis and thrombosis : a journal of vascular biology*, vol. 14, pp. 133–140, Jan. 1994.

[39] P. CONSTANTINIDES, N. GUTMANN-AUERSPERG, and D. HOSPES, "Acceleration of intimal atherogenesis through prior medial injury.," *A.M.A. archives of pathology*, vol. 66, pp. 247–254, Sept. 1958.

[40] P. CONSTANTINIDES, J. BOOTH, and G. CARLSON, "Production of advanced cholesterol atherosclerosis in the rabbit.," *Archives of pathology*, vol. 70, pp. 712–724, Dec. 1960.

[41] P. CONSTANTINIDES and R. N. CHAKRAVARTI, "Rabbit arterial thrombosis production by systemic procedures.," *Archives of pathology*, vol. 72, pp. 197–208, Aug. 1961.

[42] H. R. Baumgartner and A. Studer, "[effects of vascular catheterization in normo- and hypercholesteremic rabbits].," *Pathologia et microbiologia*, vol. 29, pp. 393–405, 1966.

[43] F. F. Weidinger, J. M. McLenachan, M. I. Cybulsky, J. T. Fallon, N. K. Hollenberg, J. P. Cooke, and P. Ganz, "Hypercholesterolemia enhances macrophage recruitment and dysfunction of regenerated endothelium after balloon injury of the rabbit iliac artery.," *Circulation*, vol. 84, pp. 755–767, Aug. 1991.

[44] G. S. Abela, P. D. Picon, S. E. Friedl, O. C. Gebara, A. Miyamoto, M. Federman, G. H. Tofler, and J. E. Muller, "Triggering of plaque disruption and arterial thrombosis in an atherosclerotic rabbit model.," *Circulation*, vol. 91, pp. 776–784, Feb. 1995.

[45] A. Phinikaridou, K. J. Hallock, Y. Qiao, and J. A. Hamilton, "A robust rabbit model of human atherosclerosis and atherothrombosis.," *Journal of lipid research*, vol. 50, pp. 787–797, May 2009.

[46] Y. Asada, A. Kisanuki, A. Tsuneyoshi, K. Marutsuka, K. Hatakeyama, and A. Sumiyoshi, "Effects of inflation pressure of balloon catheter on vascular injuries and subsequent development of intimal hyperplasia in rabbit aorta.," *Atherosclerosis*, vol. 121, pp. 45–53, Mar. 1996.

[47] S. P. Rao, M. Riederer, M. Lechleitner, M. Hermansson, G. Desoye, S. Hallstroem, W. F. Graier, and S. Frank, "Acyl chain-dependent effect of lysophosphatidylcholine on endothelium-dependent vasorelaxation.," *PloS one*, vol. 8, p. e65155, 2013.

[48] J. E. F. Fitzgerald and B. C. Caesar, "The european working time directive: a practical review for surgical trainees.," *International journal of surgery (London, England)*, vol. 10, pp. 399–403, 2012.

[49] S. Gopakumar, B. Kumar, J. Ahmed, N. Siddiqi, S. Mehmood, and P. J. Moore, "Day case surgery training for surgical trainees: a disappearing act?," *International journal of surgery (London, England)*, vol. 8, pp. 135–139, 2010.

[50] T. H. Schwarcz, P. B. Dobrin, R. Mrkvicka, L. Skowron, and M. B. Cole, "Balloon embolectomy catheter-induced arterial injury: a comparison of four catheters.," *Journal of vascular surgery*, vol. 11, pp. 382–388, Mar. 1990.

[51] A. Kuehnl, H. Soellner, and H.-H. Eckstein, "Epidemiology and inpatient treatment of vascular diseases in germany: English version.," *Gefasschirurgie : Zeitschrift fur vaskulare und endovaskulare Chirurgie : Organ der Deutschen und der Osterreichischen Gesellschaft fur Gefasschirurgie unter Mitarbeit der Schweizerischen Gesellschaft fur Gefasschirurgie*, vol. 21, pp. 14–23, 2016.

[52] B. A. Wasserman, W. I. Smith, H. H. Trout, 3rd, R. O. Cannon, 3rd, R. S. Balaban, and A. E. Arai, "Carotid artery atherosclerosis: in vivo morphologic characterization with gadolinium-enhanced double-oblique mr imaging initial results.," *Radiology*, vol. 223, pp. 566–573, May 2002.

[53] M. A. Bernstein, K. F. King, and X. J. Zhou, *Handbook of MRI Pulse Sequences*. ACADEMIC PR INC, 2004.

[54] J. P. Felmlee and R. L. Ehman, "Spatial presaturation: a method for suppressing flow artifacts and improving depiction of vascular anatomy in mr imaging.," *Radiology*, vol. 164, pp. 559–564, Aug 1987.

[55] M. Doyle, T. Matsuda, and G. M. Pohost, "Slip, a lipid suppression technique to improve image contrast in inflow angiography.," *Magnetic resonance in medicine*, vol. 21, pp. 71–81, Sept. 1991.

[56] R. R. Edelman, D. Chien, and D. Kim, "Fast selective black blood mr imaging.," *Radiology*, vol. 181, pp. 655–660, Dec 1991.

[57] V. L. Yarnykh and C. Yuan, "T1-insensitive flow suppression using quadruple inversion-recovery.," *Magn Reson Med*, vol. 48, pp. 899–905, Nov 2002.

[58] G. J. Stanisz, E. E. Odrobina, J. Pun, M. Escaravage, S. J. Graham, M. J. Bronskill, and R. M. Henkelman, "T1, t2 relaxation and magnetization transfer in tissue at 3t.," *Magnetic resonance in medicine*, vol. 54, pp. 507–512, Sept. 2005.

[59] H. K. Song, A. C. Wright, R. L. Wolf, and F. W. Wehrli, "Multislice double inversion pulse sequence for efficient black-blood mri.," *Magn Reson Med*, vol. 47, pp. 616–620, Mar 2002.

[60] D. L. Parker, K. C. Goodrich, M. Masiker, J. S. Tsuruda, and G. L. Katzman, "Improved efficiency in double-inversion fast spin-echo imaging.," *Magn Reson Med*, vol. 47, pp. 1017–1021, May 2002.

[61] V. L. Yarnykh and C. Yuan, "Multislice double inversion-recovery black-blood imaging with simultaneous slice reinversion.," *J Magn Reson Imaging*, vol. 17, pp. 478–483, Apr 2003.

[62] Z. A. Fayad, V. Fuster, J. T. Fallon, T. Jayasundera, S. G. Worthley, G. Helft, J. G. Aguinaldo, J. J. Badimon, and S. K. Sharma, "Noninvasive in vivo human coronary artery lumen and wall imaging using black-blood magnetic resonance imaging.," *Circulation*, vol. 102, pp. 506–510, Aug 2000.

[63] L. A. Crowe, P. Gatehouse, G. Z. Yang, R. H. Mohiaddin, A. Varghese, C. Charrier, J. Keegan, and D. N. Firmin, "Volume-selective 3d turbo spin echo imaging for vascular wall imaging and distensibility measurement.," *J Magn Reson Imaging*, vol. 17, pp. 572–580, May 2003.

[64] J. Frahm, A. Haase, and D. Matthaei, "Rapid nmr imaging of dynamic processes using the flash technique.," *Magnetic resonance in medicine*, vol. 3, pp. 321–327, Apr. 1986.

[65] D. A. Feinberg, J. C. Hoenninger, L. E. Crooks, L. Kaufman, J. C. Watts, and M. Arakawa, "Inner volume mr imaging: technical concepts and their application.," *Radiology*, vol. 156, pp. 743–747, Sep 1985.

[66] T. J. Masaryk, M. T. Modic, J. S. Ross, P. M. Ruggieri, G. A. Laub, G. W. Lenz, E. M. Haacke, W. R. Selman, M. Wiznitzer, and S. I. Harik, "Intracranial circulation: preliminary clinical results with three-dimensional (volume) mr angiography.," *Radiology*, vol. 171, pp. 793–799, June 1989.

[67] D. L. Parker, C. Yuan, and D. D. Blatter, "Mr angiography by multiple thin slab 3d acquisition.," *Magnetic resonance in medicine*, vol. 17, pp. 434–451, Feb. 1991.

[68] A. Priatna and C. B. Paschal, "Variable-angle uniform signal excitation (vuse) for three-dimensional time-of-flight mr angiography.," *Journal of magnetic resonance imaging : JMRI*, vol. 5, pp. 421–427, 1995.

[69] T. S. Hatsukami, R. Ross, N. L. Polissar, and C. Yuan, "Visualization of fibrous cap thickness and rupture in human atherosclerotic carotid plaque in vivo with high-resolution magnetic resonance imaging.," *Circulation*, vol. 102, pp. 959–964, Aug. 2000.

[70] C. Yuan, S.-x. Zhang, N. L. Polissar, D. Echelard, G. Ortiz, J. W. Davis, E. Ellington, M. S. Ferguson, and T. S. Hatsukami, "Identification of fibrous cap rupture with magnetic resonance imaging is highly associated with recent transient ischemic attack or stroke.," *Circulation*, vol. 105, pp. 181–185, Jan. 2002.

[71] L. M. Mitsumori, T. S. Hatsukami, M. S. Ferguson, W. S. Kerwin, J. Cai, and C. Yuan, "In vivo accuracy of multisequence mr imaging for identifying unstable fibrous caps in advanced human carotid plaques.," *Journal of magnetic resonance imaging : JMRI*, vol. 17, pp. 410–420, Apr. 2003.

[72] J. F. Toussaint, G. M. LaMuraglia, J. F. Southern, V. Fuster, and H. L. Kantor, "Magnetic resonance images lipid, fibrous, calcified, hemorrhagic, and thrombotic components of human atherosclerosis in vivo.," *Circulation*, vol. 94, pp. 932–938, Sept. 1996.

[73] W. G. Bradley, "Mr appearance of hemorrhage in the brain.," *Radiology*, vol. 189, pp. 15–26, Oct. 1993.

[74] V. C. Cappendijk, K. B. J. M. Cleutjens, S. Heeneman, G. W. H. Schurink, R. J. T. J. Welten, A. G. H. Kessels, R. J. van Suylen, M. J. A. P. Daemen, J. M. A. van Engelshoven, and M. E. Kooi, "In vivo detection of hemorrhage in human

atherosclerotic plaques with magnetic resonance imaging.," *Journal of magnetic resonance imaging : JMRI*, vol. 20, pp. 105–110, July 2004.

[75] Z. A. Fayad, T. Nahar, J. T. Fallon, M. Goldman, J. G. Aguinaldo, J. J. Badimon, M. Shinnar, J. H. Chesebro, and V. Fuster, "In vivo magnetic resonance evaluation of atherosclerotic plaques in the human thoracic aorta: a comparison with transesophageal echocardiography.," *Circulation*, vol. 101, pp. 2503–2509, May 2000.

[76] C. Yuan, L. M. Mitsumori, M. S. Ferguson, N. L. Polissar, D. Echelard, G. Ortiz, R. Small, J. W. Davies, W. S. Kerwin, and T. S. Hatsukami, "In vivo accuracy of multispectral magnetic resonance imaging for identifying lipid-rich necrotic cores and intraplaque hemorrhage in advanced human carotid plaques.," *Circulation*, vol. 104, pp. 2051–2056, Oct. 2001.

[77] M. Shinnar, J. T. Fallon, S. Wehrli, M. Levin, D. Dalmacy, Z. a. Fayad, J. J. Badimon, M. Harrington, E. Harrington, and V. Fuster, "The diagnostic accuracy of ex vivo MRI for human atherosclerotic plaque characterization," *Arterioscler Thromb Vasc Biol*, vol. 19, no. 11, pp. 2756–2761, 1999.

[78] S. E. Clarke, R. R. Hammond, J. R. Mitchell, and B. K. Rutt, "Quantitative assessment of carotid plaque composition using multicontrast mri and registered histology.," *Magnetic resonance in medicine*, vol. 50, pp. 1199–1208, Dec. 2003.

[79] J.-M. Cai, T. S. Hatsukami, M. S. Ferguson, R. Small, N. L. Polissar, and C. Yuan, "Classification of human carotid atherosclerotic lesions with in vivo multicontrast magnetic resonance imaging.," *Circulation*, vol. 106, pp. 1368–1373, sep 2002.

[80] T. Saam, M. S. Ferguson, V. L. Yarnykh, N. Takaya, D. Xu, N. L. Polissar, T. S. Hatsukami, and C. Yuan, "Quantitative evaluation of carotid plaque composition by in vivo MRI," *Arteriosclerosis, Thrombosis, and Vascular Biology*, vol. 25, no. 1, pp. 234–239, 2005.

[81] S. Zhang, T. S. Hatsukami, N. L. Polissar, C. Han, and C. Yuan, "Comparison of carotid vessel wall area measurements using three different contrast-weighted black blood mr imaging techniques.," *Magnetic resonance imaging*, vol. 19, pp. 795–802, July 2001.

[82] B. D. Coombs, J. H. Rapp, P. C. Ursell, L. M. Reilly, and D. Saloner, "Structure of plaque at carotid bifurcation: high-resolution MRI with histological correlation.," *Stroke; a journal of cerebral circulation*, vol. 32, no. 114, pp. 2516–2521, 2001.

[83] Y. Luo, N. Polissar, C. Han, V. Yarnykh, W. S. Kerwin, T. S. Hatsukami, and C. Yuan, "Accuracy and uniqueness of three in vivo measurements of atherosclerotic carotid plaque morphology with black blood mri.," *Magnetic resonance in medicine*, vol. 50, pp. 75–82, July 2003.

[84] C. M. Kramer, L. A. Cerilli, K. Hagspiel, J. M. DiMaria, F. H. Epstein, and J. A. Kern, "Magnetic Resonance Imaging Identifies the Fibrous Cap in Atherosclerotic Abdominal Aortic Aneurysm," *Circulation*, vol. 109, no. 8, pp. 1016–1021, 2004.

[85] Z. A. Fayad and V. Fuster, "Characterization of atherosclerotic plaques by magnetic resonance imaging.," *Annals of the New York Academy of Sciences*, vol. 902, pp. 173–186, May 2000.

[86] C. Yuan, L. M. Mitsumori, K. W. Beach, and K. R. Maravilla, "Carotid atherosclerotic plaque: noninvasive mr characterization and identification of vulnerable lesions.," *Radiology*, vol. 221, pp. 285–299, Nov. 2001.

[87] H. H. Quick, J. F. Debatin, and M. E. Ladd, "MR imaging of the vessel wall," *European Radiology*, vol. 12, no. 4, pp. 889–900, 2002.

[88] T. Saam, S. Schoenberg, T. Hatsukami, M. Reiser, C. Yuan, and K. Nikolaou, "Hochauflösende Bildgebung atherosklerotischer Gefäßwandläsionen der Karotiden durch dieÂ Magnetresonanztomografie," *RöFo - Fortschritte auf dem Gebiet der Röntgenstrahlen und der bildgebenden Verfahren*, vol. 180, no. 2, pp. 100–111, 2008.

[89] J. Wang, M. S. Ferguson, N. Balu, C. Yuan, T. S. Hatsukami, and P. Bornert, "Improved carotid intraplaque hemorrhage imaging using a slab-selective phase-sensitive inversion-recovery (SPI) sequence," *Magnetic Resonance in Medicine*, vol. 64, no. 5, pp. 1332–1340, 2010.

[90] J. Wang, V. L. Yarnykh, T. Hatsukami, B. Chu, N. Balu, and C. Yuan, "Improved suppression of plaque-mimicking artifacts in black-blood carotid atherosclerosis imaging using a multislice motion-sensitized driven-equilibrium (MSDE)

turbo spin-echo (TSE) sequence," *Magnetic Resonance in Medicine*, vol. 58, no. 5, pp. 973–981, 2007.

[91] J. Wang, V. L. Yarnykh, and C. Yuan, "Enhanced image quality in black-blood MRI using the improved motion-sensitized driven-equilibrium (iMSDE) sequence," *Journal of Magnetic Resonance Imaging*, vol. 31, no. 5, pp. 1256–1263, 2010.

[92] N. Balu, V. L. Yarnykh, B. Chu, J. Wang, T. Hatsukami, and C. Yuan, "Carotid plaque assessment using fast 3D isotropic resolution black-blood MRI," *Magnetic Resonance in Medicine*, vol. 65, no. 3, pp. 627–637, 2011.

[93] N. Balu, V. Yarnykh, W. Kerwin, J. Wang, and C. Yuan, "Interpretation of tissue contrast in a rapid black-blood gradient echo sequence with motion-sensitized driven-equilibrium (msde) preparation (3d merge) for 3d isotropic high-resolution imaging of the vessel wall and its application for hemorrhage detection.," *Proceedings of the ISMRM 19th Annual Meeting*, 2011.

[94] X. Zhao, N. Balu, W. Liu, J. Wang, H. Zhao, J. Xu, and C. Yuan, "Characterization of carotid atherosclerotic plaque composition by single magnetic resonance sequence: A comparison study with multicontrast plaque imaging at 3t.," *Proceedings of the ISMRM 19th Annual Meeting*, 2011.

[95] J. Wang, P. Boernert, H. Zhao, D. S. Hippe, X. Zhao, N. Balu, M. S. Ferguson, T. S. Hatsukami, J. Xu, C. Yuan, and W. S. Kerwin, "Simultaneous noncontrast angiography and intraplaque hemorrhage (snap) imaging for carotid atherosclerotic disease evaluation.," *Magnetic resonance in medicine*, vol. 69, pp. 337–345, Feb. 2013.

[96] G. Xie, N. Zhang, Y. Xie, C. Nguyen, Z. Deng, X. Bi, Z. Fan, X. Liu, D. Li, and Z. Fan, "DANTE-prepared three-dimensional FLASH: A fast isotropic-resolution MR approach to morphological evaluation of the peripheral arterial wall at 3 tesla," *Journal of Magnetic Resonance Imaging*, vol. 43, pp. 343–351, jul 2015.

[97] Z. Fan, W. Yu, Y. Xie, L. Dong, L. Yang, Z. Wang, A. H. Conte, X. Bi, J. An, T. Zhang, G. Laub, P. K. Shah, Z. Zhang, and D. Li, "Multi-contrast atherosclerosis characterization (MATCH) of carotid plaque with a single 5-min scan: technical development and clinical feasibility," *Journal of Cardiovascular Magnetic Resonance*, vol. 16, jul 2014.

[98] Z. Fan, Z. Zhang, Y.-C. Chung, P. Weale, S. Zuehlsdorff, J. Carr, and D. Li, "Carotid arterial wall mri at 3t using 3d variable-flip-angle turbo spin-echo (tse) with flow-sensitive dephasing (fsd).," *Journal of magnetic resonance imaging : JMRI*, vol. 31, pp. 645–654, Mar. 2010.

[99] Q. Yang, J. Liu, S. R. S. Barnes, Z. Wu, K. Li, J. Neelavalli, J. Hu, and E. M. Haacke, "Imaging the vessel wall in major peripheral arteries using susceptibility-weighted imaging," *Journal of Magnetic Resonance Imaging*, vol. 30, no. 2, pp. 357–365, 2009.

[100] Y. Qiao, K. J. Hallock, and J. A. Hamilton, "Magnetization transfer magnetic resonance of human atherosclerotic plaques ex vivo detects areas of high protein density," *Journal of Cardiovascular Magnetic Resonance*, vol. 13, no. 1, p. 73, 2011.

[101] Z. Zhou, R. Li, X. Zhao, L. He, X. Wang, J. Wang, N. Balu, and C. Yuan, "Evaluation of 3d multi-contrast joint intra- and extracranial vessel wall cardiovascular magnetic resonance," *Journal of Cardiovascular Magnetic Resonance*, vol. 17, may 2015.

[102] A. Jackson, "Quantitative MRI of the brain: measuring changes caused by disease . by p tofts, pp. xvi633, 2003 (john wiley & sons ltd, chichester, UK) £175.00 ISBN 0-470-84721-2," *The British Journal of Radiology*, vol. 78, pp. 87–87, jan 2005.

[103] E. O. Stejskal and J. E. Tanner, "Spin diffusion measurements: Spin echoes in the presence of a time-dependent field gradient," *The Journal of Chemical Physics*, vol. 42, pp. 288–292, jan 1965.

[104] C. Beaulieu, "The basis of anisotropic water diffusion in the nervous system - a technical review.," *NMR in biomedicine*, vol. 15, pp. 435–455, 2002.

[105] D. A. Lansdown, Z. Ding, M. Wadington, J. L. Hornberger, and B. M. Damon, "Quantitative diffusion tensor mri-based fiber tracking of human skeletal muscle.," *Journal of applied physiology (Bethesda, Md. : 1985)*, vol. 103, pp. 673–681, Aug. 2007.

[106] P. B. Kingsley, "Introduction to diffusion tensor imaging mathematics: Part i. tensors, rotations, and eigenvectors," *Concepts in Magnetic Resonance Part A*, vol. 28A, no. 2, pp. 101–122, 2006.

[107] P. B. Kingsley, "Introduction to diffusion tensor imaging mathematics: Part II. anisotropy, diffusion-weighting factors, and gradient encoding schemes," *Concepts in Magnetic Resonance Part A*, vol. 28A, no. 2, pp. 123–154, 2006.

[108] P. B. Kingsley, "Introduction to diffusion tensor imaging mathematics: Part III. tensor calculation, noise, simulations, and optimization," *Concepts in Magnetic Resonance Part A*, vol. 28A, no. 2, pp. 155–179, 2006.

[109] S. Shahid, C. Kerskens, R. Gaul, V. Flamini, and C. Lally, "Ex-vivo arterial collagen fibre tractography using micro-diffusion tensor imaging (μ-dti).," *Proceedings of the ESMRMB 33rd Annual Meeting*, 2016.

[110] S. Mori and J. Zhang, "Principles of diffusion tensor imaging and its applications to basic neuroscience research.," *Neuron*, vol. 51, pp. 527–539, Sept. 2006.

[111] S.-E. Kim, E.-K. Jeong, X.-F. Shi, G. Morrell, G. S. Treiman, and D. L. Parker, "Diffusion-weighted imaging of human carotid artery using 2d single-shot interleaved multislice inner volume diffusion-weighted echo planar imaging (2d ss-imivdwepi) at 3t: diffusion measurement in atherosclerotic plaque.," *J Magn Reson Imaging*, vol. 30, pp. 1068–1077, Nov 2009.

[112] V. E. Young, A. J. Patterson, U. Sadat, D. J. Bowden, M. J. Graves, T. Y. Tang, A. N. Priest, J. N. Skepper, P. J. Kirkpatrick, and J. H. Gillard, "Diffusion-weighted magnetic resonance imaging for the detection of lipid-rich necrotic core in carotid atheroma in vivo.," *Neuroradiology*, vol. 52, pp. 929–936, Oct. 2010.

[113] S.-E. Kim, G. S. Treiman, J. A. Roberts, E.-K. Jeong, X. Shi, J. R. Hadley, and D. L. Parker, "In vivo and ex vivo measurements of the mean adc values of lipid necrotic core and hemorrhage obtained from diffusion weighted imaging in human atherosclerotic plaques.," *J Magn Reson Imaging*, vol. 34, pp. 1167–1175, Nov 2011.

[114] Y. Xie, W. Yu, Z. Fan, C. Nguyen, X. Bi, J. An, T. Zhang, Z. Zhang, and D. Li, "High resolution 3d diffusion cardiovascular magnetic resonance of carotid vessel wall to detect lipid core without contrast media.," *J Cardiovasc Magn Reson*, vol. 16, p. 67, 2014.

[115] S. Chen, H. Guo, W. Wu, X. Zhao, C. Yuan, and H. Chen, "High resolution diffusion-weighted imaging with variable density spiral acquisition of carotid vessel wall.," *Proceedings of the ISMRM 21st Annual Meeting*, 2013.

[116] P. Opriessnig, H. Mangge, R. Stollberger, H. Deutschmann, and G. Reishofer, "In vivo cardiovascular magnetic resonance of 2d vessel wall diffusion anisotropy in carotid arteries," *Journal of Cardiovascular Magnetic Resonance*, vol. 18, nov 2016.

[117] S. Ghazanfari, A. Driessen-Mol, G. J. Strijkers, F. M. W. Kanters, F. P. T. Baaijens, and C. V. C. Bouten, "A comparative analysis of the collagen architecture in the carotid artery: second harmonic generation versus diffusion tensor imaging.," *Biochem Biophys Res Commun*, vol. 426, pp. 54–58, Sep 2012.

[118] V. Flamini, C. Kerskens, C. Simms, and C. Lally, "Fibre orientation of fresh and frozen porcine aorta determined non-invasively using diffusion tensor imaging.," *Med Eng Phys*, vol. 35, pp. 765–776, Jun 2013.

[119] T. H. Schiebler and H.-W. Korf, *Anatomie.* Steinkopff Dr. Dietrich V, 2007.

[120] D. A. Porter and R. M. Heidemann, "High resolution diffusion-weighted imaging using readout-segmented echo-planar imaging, parallel imaging and a two-dimensional navigator-based reacquisition.," *Magn Reson Med*, vol. 62, pp. 468–475, Aug 2009.

[121] R. M. Berquist, K. M. Gledhill, M. W. Peterson, A. H. Doan, G. T. Baxter, K. E. Yopak, N. Kang, H. J. Walker, P. A. Hastings, and L. R. Frank, "The digital fish library: using mri to digitize, database, and document the morphological diversity of fish.," *PloS one*, vol. 7, p. e34499, 2012.

[122] S. Klein, M. Staring, K. Murphy, M. A. Viergever, and J. P. W. Pluim, "elastix: a toolbox for intensity-based medical image registration.," *IEEE Trans Med Imaging*, vol. 29, no. 1, pp. 196–205, 2010.

[123] D. P. Shamonin, E. E. Bron, B. P. F. Lelieveldt, M. Smits, S. Klein, M. Staring, and A. D. N. Initiative, "Fast parallel image registration on CPU and GPU for diagnostic classification of Alzheimer's disease.," *Front Neuroinform*, vol. 7, p. 50, 2013.

[124] J. M. Soares, P. Marques, V. Alves, and N. Sousa, "A hitchhiker ' s guide to diffusion tensor imaging," vol. 7, no. March, pp. 1–14, 2013.

[125] R. V. Klooster, M. Staring, S. Klein, R. M. Kwee, M. E. Kooi, J. H. C. Reiber, and B. P. F. Lelieveldt, "Automated registration of multispectral MR vessel wall images of the carotid artery Automated registration of multispectral MR vessel wall images," vol. 121904, no. 2013, 2015.

[126] R. C. Team, "R: A language and environment for statistical computing. R Foundation for Statistical Computing, Vienna, Austria. 2013," 2014.

[127] Z. Fan, S. Zuehlsdorff, X. Liu, and D. Li, "Prospective self-gating for swallowing motion: a feasibility study in carotid artery wall mri using three-dimensional variable-flip-angle turbo spin-echo.," *Magnetic resonance in medicine*, vol. 67, pp. 490–498, Feb. 2012.

[128] Y. Xie, Z. Fan, and D. Li, "weighted vessel wall imaging at 3T," vol. 15, no. Suppl 1, pp. 2–4, 2013.

[129] M. A. Griswold, P. M. Jakob, R. M. Heidemann, M. Nittka, V. Jellus, J. Wang, B. Kiefer, and A. Haase, "Generalized Autocalibrating Partially Parallel Acquisitions (GRAPPA)," *Magnetic Resonance in Medicine*, vol. 47, no. 6, pp. 1202–1210, 2002.

[130] K. L. Miller and J. M. Pauly, "Nonlinear phase correction for navigated diffusion imaging.," *Magnetic resonance in medicine*, vol. 50, pp. 343–353, Aug. 2003.

[131] J. Cohen-adad, "High-Resolution DWI in Brain and Spinal Cord with syngo RE-SOLVE 1," *Siemens Magnetom - Clinical Neurology*, vol. 510, pp. 16–23, 2012.

[132] L. L. Hayes, D. a. Porter, R. a. Jones, S. Palasis, and J. D. Grattan-smith, "RE-SOLVE : A Powerful Tool for Imaging the Pediatric Spine," *MAGNETOM Flash*, vol. 2, pp. 38–45, 2014.

[133] O. Tehlivets, "Homocysteine as a risk factor for atherosclerosis: is its conversion to s-adenosyl-l-homocysteine the key to deregulated lipid metabolism?," *Journal of lipids*, vol. 2011, p. 702853, 2011.

[134] H. Wolinski and S. D. Kohlwein, "Microscopic and spectroscopic techniques to investigate lipid droplet formation and turnover in yeast.," *Methods in molecular biology (Clifton, N.J.)*, vol. 1270, pp. 289–305, 2015.

[135] S. G. Ruehm, C. Corot, P. Vogt, S. Kolb, and J. F. Debatin, "Magnetic resonance imaging of atherosclerotic plaque with ultrasmall superparamagnetic particles of iron oxide in hyperlipidemic rabbits.," *Circulation*, vol. 103, pp. 415–422, Jan. 2001.

[136] S. Litovsky, M. Madjid, A. Zarrabi, S. W. Casscells, J. T. Willerson, and M. Naghavi, "Superparamagnetic iron oxide-based method for quantifying recruitment of monocytes to mouse atherosclerotic lesions in vivo: enhancement by tissue necrosis factor-alpha, interleukin-1beta, and interferon-gamma.," *Circulation*, vol. 107, pp. 1545–1549, Mar. 2003.

[137] M. Sigovan, A. Bessaad, H. Alsaid, E. Lancelot, C. Corot, B. Neyran, N. Provost, Z. Majd, M. Breisse, and E. Canet-Soulas, "Assessment of age modulated vascular inflammation in apoe-/- mice by uspio-enhanced magnetic resonance imaging.," *Investigative radiology*, vol. 45, pp. 702–707, Nov. 2010.

[138] K. A. Kelly, J. R. Allport, A. Tsourkas, V. R. Shinde-Patil, L. Josephson, and R. Weissleder, "Detection of vascular adhesion molecule-1 expression using a novel multimodal nanoparticle.," *Circulation research*, vol. 96, pp. 327–336, Feb. 2005.

[139] H. W. Kang, D. Torres, L. Wald, R. Weissleder, and A. A. Bogdanov, "Targeted imaging of human endothelial-specific marker in a model of adoptive cell transfer.," *Laboratory investigation; a journal of technical methods and pathology*, vol. 86, pp. 599–609, June 2006.

[140] M.-J. Jacobin-Valat, K. Deramchia, S. Mornet, C. E. Hagemeyer, S. Bonetto, R. Robert, M. Biran, P. Massot, S. Miraux, S. Sanchez, A.-K. Bouzier-Sore, J.-M. Franconi, E. Duguet, and G. Clofent-Sanchez, "Mri of inducible p-selectin expression in human activated platelets involved in the early stages of atherosclerosis.," *NMR in biomedicine*, vol. 24, pp. 413–424, May 2011.

[141] R. Uppal and P. Caravan, "Targeted probes for cardiovascular MRI," *Future Medicinal Chemistry*, vol. 2, pp. 451–470, mar 2010.

[142] *Handbook of Nanophysics.* Taylor & Francis, 2010.

[143] Y. Anzai, M. R. Prince, T. L. Chenevert, J. H. Maki, F. Londy, M. London, and S. J. McLachlan, "Mr angiography with an ultrasmall superparamagnetic iron oxide blood pool agent.," *Journal of magnetic resonance imaging : JMRI*, vol. 7, pp. 209–214, 1997.

[144] P. Reimer, C. Bremer, T. Allkemper, M. Engelhardt, M. Mahler, W. Ebert, and B. Tombach, "Myocardial perfusion and mr angiography of chest with sh u 555 c: results of placebo-controlled clinical phase i study.," *Radiology*, vol. 231, pp. 474–481, May 2004.

[145] J. Bremerich, D. Bilecen, and P. Reimer, "Mr angiography with blood pool contrast agents.," *European radiology*, vol. 17, pp. 3017–3024, Dec. 2007.

[146] M. D. Hope, T. A. Hope, C. Zhu, F. Faraji, H. Haraldsson, K. G. Ordovas, and D. Saloner, "Vascular imaging with ferumoxytol as a contrast agent.," *AJR. American journal of roentgenology*, vol. 205, pp. W366–W373, Sept. 2015.

[147] M. Rohrer, H. Bauer, J. Mintorovitch, M. Requardt, and H.-J. Weinmann, "Comparison of magnetic properties of mri contrast media solutions at different magnetic field strengths.," *Investigative radiology*, vol. 40, pp. 715–724, Nov. 2005.

[148] M. R. Prince, H. L. Zhang, S. G. Chabra, P. Jacobs, and Y. Wang, "A pilot investigation of new superparamagnetic iron oxide (ferumoxytol) as a contrast agent for cardiovascular mri.," *Journal of X-ray science and technology*, vol. 11, pp. 231–240, Jan. 2003.

[149] B. S. Spinowitz, A. T. Kausz, J. Baptista, S. D. Noble, R. Sothinathan, M. V. Bernardo, L. Brenner, and B. J. G. Pereira, "Ferumoxytol for treating iron deficiency anemia in ckd.," *Journal of the American Society of Nephrology : JASN*, vol. 19, pp. 1599–1605, Aug. 2008.

[150] M. Lu, M. H. Cohen, D. Rieves, and R. Pazdur, "Fda report: Ferumoxytol for intravenous iron therapy in adult patients with chronic kidney disease.," *American journal of hematology*, vol. 85, pp. 315–319, May 2010.

[151] S. a. Schmitz, M. Taupitz, S. Wagner, K. J. Wolf, D. Beyersdorff, and B. Hamm, "Magnetic resonance imaging of atherosclerotic plaques using superparamagnetic iron oxide particles.," *Journal of magnetic resonance imaging : JMRI*, vol. 14, pp. 355–361, 2001.

[152] M. E. Kool, V. C. Cappendijk, K. B. J. M. Cleutjens, A. G. H. Kessels, P. J. E. H. M. Kitslaar, M. Borgers, P. M. Frederik, M. J. A. P. Daemen, and J. M. A. Van Engelshoven, "Accumulation of ultrasmall superparamagnetic particles of iron oxide in human atherosclerotic plaques can be detected by in vivo magnetic resonance imaging," *Circulation*, vol. 107, no. 19, pp. 2453–2458, 2003.

[153] G. H. Simon, J. von Vopelius-Feldt, Y. Fu, J. Schlegel, G. Pinotek, M. F. Wendland, M.-H. Chen, and H. E. Daldrup-Link, "Ultrasmall supraparamagnetic iron oxide-enhanced magnetic resonance imaging of antigen-induced arthritis: a comparative study between shu 555 c, ferumoxtran-10, and ferumoxytol.," *Investigative radiology*, vol. 41, pp. 45–51, Jan. 2006.

[154] R. A. Trivedi, J.-M. U-King-Im, M. J. Graves, J. J. Cross, J. Horsley, M. J. Goddard, J. N. Skepper, G. Quartey, E. Warburton, I. Joubert, L. Wang, P. J. Kirkpatrick, J. Brown, and J. H. Gillard, "In vivo detection of macrophages in human carotid atheroma: temporal dependence of ultrasmall superparamagnetic particles of iron oxide-enhanced mri.," *Stroke*, vol. 35, pp. 1631–1635, July 2004.

[155] T. Y. Tang, S. P. S. Howarth, S. R. Miller, M. J. Graves, J. M. U-King-Im, Z. Y. Li, S. R. Walsh, P. D. Hayes, K. Varty, and J. H. Gillard, "Comparison of the inflammatory burden of truly asymptomatic carotid atheroma with atherosclerotic plaques in patients with asymptomatic carotid stenosis undergoing coronary artery bypass grafting: an ultrasmall superparamagnetic iron oxide enhanced magnetic resonance study.," *European journal of vascular and endovascular surgery : the official journal of the European Society for Vascular Surgery*, vol. 35, pp. 392–398, Apr. 2008.

[156] T. Y. Tang, S. P. S. Howarth, S. R. Miller, M. J. Graves, J.-M. U-King-Im, Z.-Y. Li, S. R. Walsh, A. J. Patterson, P. J. Kirkpatrick, E. A. Warburton, K. Varty, M. E. Gaunt, and J. H. Gillard, "Correlation of carotid atheromatous plaque inflammation using uspio-enhanced mr imaging with degree of luminal stenosis.," *Stroke*, vol. 39, pp. 2144–2147, July 2008.

[157] A. J. Patterson, T. Y. Tang, M. J. Graves, K. H. Mueller, and J. H. Gillard, "In vivo carotid plaque mri using quantitative t2* measurements with ultrasmall superparamagnetic iron oxide particles: a dose-response study to statin therapy.," *NMR in biomedicine*, vol. 24, pp. 89–95, Jan. 2011.

113

[158] M. Sigovan, L. Boussel, A. Sulaiman, D. Sappey-Marinier, H. Alsaid, C. Desbleds-Mansard, D. Ibarrola, D. Gamondès, C. Corot, E. Lancelot, J.-S. Raynaud, V. Vives, C. Laclédère, X. Violas, P. C. Douek, and E. Canet-Soulas, "Rapid-clearance iron nanoparticles for inflammation imaging of atherosclerotic plaque: initial experience in animal model.," *Radiology*, vol. 252, no. 2, pp. 401–409, 2009.

[159] C. U. Herborn, F. M. Vogt, T. C. Lauenstein, O. Dirsch, C. Corot, P. Robert, and S. G. Ruehm, "Magnetic resonance imaging of experimental atherosclerotic plaque: Comparison of two ultrasmall superparamagnetic particles of iron oxide," *Journal of Magnetic Resonance Imaging*, vol. 24, no. 2, pp. 388–393, 2006.

[160] E. A. Schellenberger, A. Bogdanov, D. Hoegemann, J. Tait, R. Weissleder, and L. Josephson, "Annexin v-clio: a nanoparticle for detecting apoptosis by mri.," *Molecular imaging*, vol. 1, pp. 102–107, 2002.

[161] C. Burtea, S. Ballet, S. Laurent, O. Rousseaux, A. Dencausse, W. Gonzalez, M. Port, C. Corot, L. V. Elst, and R. N. Muller, "Development of a magnetic resonance imaging protocol for the characterization of atherosclerotic plaque by using vascular cell adhesion molecule-1 and apoptosis-targeted ultrasmall superparamagnetic iron oxide derivatives," *Arteriosclerosis, Thrombosis, and Vascular Biology*, vol. 32, no. 6, 2012.

[162] Z. A. Fayad, L. Razzouk, K. C. Briley-Saebo, and V. Mani, "Iron oxide magnetic resonance imaging for atherosclerosis therapeutic evaluation: still "rusty?".," *Journal of the American College of Cardiology*, vol. 53, pp. 2051–2052, June 2009.

[163] K. Briley-Saebo, A. Bjoernerud, D. Grant, H. Ahlstrom, T. Berg, and G. M. Kindberg, "Hepatic cellular distribution and degradation of iron oxide nanoparticles following single intravenous injection in rats: implications for magnetic resonance imaging.," *Cell and tissue research*, vol. 316, pp. 315–323, June 2004.

[164] N. Stadler, R. A. Lindner, and M. J. Davies, "Direct detection and quantification of transition metal ions in human atherosclerotic plaques: evidence for the presence of elevated levels of iron and copper.," *Arteriosclerosis, thrombosis, and vascular biology*, vol. 24, pp. 949–954, May 2004.

[165] S. J. H. Soenen, M. Hodenius, and M. De Cuyper, "Magnetoliposomes: versatile innovative nanocolloids for use in biotechnology and biomedicine.," *Nanomedicine (London, England)*, vol. 4, pp. 177–191, Feb. 2009.

[166] S. A. Wickline, A. M. Neubauer, P. M. Winter, S. D. Caruthers, and G. M. Lanza, "Molecular imaging and therapy of atherosclerosis with targeted nanoparticles.," *Journal of magnetic resonance imaging : JMRI*, vol. 25, pp. 667–680, Apr. 2007.

[167] P. M. Winter, A. M. Morawski, S. D. Caruthers, R. W. Fuhrhop, H. Zhang, T. A. Williams, J. S. Allen, E. K. Lacy, J. D. Robertson, G. M. Lanza, and S. A. Wickline, "Molecular Imaging of Angiogenesis in Early-Stage Atherosclerosis With alpha(v)beta3-Integrin-Targeted Nanoparticles," *Circulation*, vol. 108, no. 18, pp. 2270–2274, 2003.

[168] A. Maiseyeu, G. Mihai, T. Kampfrath, O. P. Simonetti, C. K. Sen, S. Roy, S. Rajagopalan, and S. Parthasarathy, "Gadolinium-containing phosphatidylserine liposomes for molecular imaging of atherosclerosis.," *Journal of lipid research*, vol. 50, no. 11, pp. 2157–2163, 2009.

[169] W. J. M. Mulder, K. Douma, G. A. Koning, M. A. Van Zandvoort, E. Lutgens, M. J. Daemen, K. Nicolay, and G. J. Strijkers, "Liposome-enhanced MRI of neointimal lesions in the ApoE-KO mouse," *Magnetic Resonance in Medicine*, vol. 55, no. 5, pp. 1170–1174, 2006.

[170] G. S. Van Bochove, L. E. M. Paulis, D. Segers, W. J. M. Mulder, R. Krams, K. Nicolay, and G. J. Strijkers, "Contrast enhancement by differently sized paramagnetic MRI contrast agents in mice with two phenotypes of atherosclerotic plaque," *Contrast Media and Molecular Imaging*, vol. 6, no. 1, pp. 35–45, 2011.

[171] A. Samad, S. Beg, and I. Nazish, *Liposomal Delivery Systems: Advances and Challenges*. Future Science Ltd, January 2016.

[172] T. M. Allen and P. R. Cullis, "Liposomal drug delivery systems: from concept to clinical applications.," *Advanced drug delivery reviews*, vol. 65, pp. 36–48, Jan. 2013.

[173] A. L. Petersen, A. E. Hansen, A. Gabizon, and T. L. Andresen, "Liposome imaging agents in personalized medicine.," *Advanced drug delivery reviews*, vol. 64, pp. 1417–1435, Oct. 2012.

[174] V. P. Torchilin, "Recent advances with liposomes as pharmaceutical carriers.," *Nature reviews. Drug discovery*, vol. 4, pp. 145–160, Feb. 2005.

[175] A. Maiseyeu, G. Mihai, S. Roy, N. Kherada, O. P. Simonetti, C. K. Sen, Q. Sun, S. Parthasarathy, and S. Rajagopalan, "Detection of macrophages via paramagnetic vesicles incorporating oxidatively tailored cholesterol ester: an approach for atherosclerosis imaging.," *Nanomedicine (Lond)*, vol. 5, pp. 1341–1356, Nov 2010.

[176] K. Kono, S. Nakashima, D. Kokuryo, I. Aoki, H. Shimomoto, S. Aoshima, K. Maruyama, E. Yuba, C. Kojima, A. Harada, and Y. Ishizaka, "Multi-functional liposomes having temperature-triggered release and magnetic resonance imaging for tumor-specific chemotherapy.," *Biomaterials*, vol. 32, pp. 1387–1395, Feb 2011.

[177] A. H. Negussie, P. S. Yarmolenko, A. Partanen, A. Ranjan, G. Jacobs, D. Woods, H. Bryant, D. Thomasson, M. W. Dewhirst, B. J. Wood, and M. R. Dreher, "Formulation and characterisation of magnetic resonance imageable thermally sensitive liposomes for use with magnetic resonance-guided high intensity focused ultrasound.," *Int J Hyperthermia*, vol. 27, no. 2, pp. 140–155, 2011.

[178] M. de Smet, E. Heijman, S. Langereis, N. M. Hijnen, and H. Grüll, "Magnetic resonance imaging of high intensity focused ultrasound mediated drug delivery from temperature-sensitive liposomes: an in vivo proof-of-concept study.," *J Control Release*, vol. 150, pp. 102–110, Feb 2011.

[179] E. Cittadino, M. Ferraretto, E. Torres, A. Maiocchi, B. J. Crielaard, T. Lammers, G. Storm, S. Aime, and E. Terreno, "Mri evaluation of the antitumor activity of paramagnetic liposomes loaded with prednisolone phosphate.," *Eur J Pharm Sci*, vol. 45, pp. 436–441, Mar 2012.

[180] C. Grange, S. Geninatti-Crich, G. Esposito, D. Alberti, L. Tei, B. Bussolati, S. Aime, and G. Camussi, "Combined delivery and magnetic resonance imaging of neural cell adhesion molecule-targeted doxorubicin-containing liposomes in experimentally induced kaposi's sarcoma.," *Cancer Res*, vol. 70, pp. 2180–2190, Mar 2010.

[181] J. H. Maeng, D.-H. Lee, K. H. Jung, Y.-H. Bae, I.-S. Park, S. Jeong, Y.-S. Jeon, C.-K. Shim, W. Kim, J. Kim, J. Lee, Y.-M. Lee, J.-H. Kim, W.-H. Kim, and S.-S. Hong, "Multifunctional doxorubicin loaded superparamagnetic iron oxide nanoparticles for chemotherapy and magnetic resonance imaging in liver cancer.," *Biomaterials*, vol. 31, pp. 4995–5006, Jun 2010.

[182] P. Nguyen, C. Meyer, J. Engvall, P. Yang, and M. McConnell, "Noninvasive assessment of coronary vasodilation using cardiovascular magnetic resonance in patients at high risk for coronary artery disease," *Journal of Cardiovascular Magnetic Resonance*, vol. 10, no. 1, p. 28, 2008.

[183] M. Terashima, P. K. Nguyen, G. D. Rubin, C. Iribarren, B. K. Courtney, A. S. Go, S. P. Fortmann, and M. V. McConnell, "Impaired Coronary Vasodilation by Magnetic Resonance Angiography Is Associated With Advanced Coronary Artery Calcification," *JACC: Cardiovascular Imaging*, vol. 1, no. 2, pp. 167–173, 2008.

[184] A. G. Hays, G. A. Hirsch, S. Kelle, G. Gerstenblith, R. G. Weiss, and M. Stuber, "Noninvasive visualization of coronary artery endothelial function in healthy subjects and in patients with coronary artery disease," *Journal of the American College of Cardiology*, vol. 56, no. 20, pp. 1657–1665, 2010.

[185] P. Opriessnig, G. Almer, H. Froehlich, C. Cabella, R. Stollberger, S. Hallstroem, G. Hoerl, and H. Mannge, "Evaluation of endothelial barrier function in atherosclerosis induced rabbits using s-nitroso human serum albumin (s-no-hsa) - blood pool agent compound and dynamic contrast-enhanced (dce)-mri.," *Proceedings of the ISMRM 24th Annual Meeting*, 2016.

[186] J.-C. Cornily, F. Hyafil, C. Calcagno, K. C. Briley-Saebo, J. Tunstead, J.-G. S. Aguinaldo, V. Mani, V. Lorusso, F. M. Cavagna, and Z. A. Fayad, "Evaluation of neovessels in atherosclerotic plaques of rabbits using an albumin-binding intravascular contrast agent and mri.," *Journal of magnetic resonance imaging : JMRI*, vol. 27, pp. 1406–1411, June 2008.

[187] C. de Haen, P. L. Anelli, V. Lorusso, A. Morisetti, F. Maggioni, J. Zheng, F. Uggeri, and F. M. Cavagna, "Gadocoletic acid trisodium salt (b22956/1): a new blood pool magnetic resonance contrast agent with application in coronary angiography.," *Investigative radiology*, vol. 41, pp. 279–291, Mar. 2006.

[188] S. Hallstroem, H. Gasser, C. Neumayer, A. Fuegl, J. Nanobashvili, A. Jakubowski, I. Huk, G. Schlag, and T. Malinski, "S-nitroso human serum albumin treatment reduces ischemia/reperfusion injury in skeletal muscle via nitric oxide release.," *Circulation*, vol. 105, pp. 3032–3038, June 2002.

117

[189] S. Sourbron, M. Ingrisch, A. Siefert, M. Reiser, and K. Herrmann, "Quantification of cerebral blood flow, cerebral blood volume, and blood-brain-barrier leakage with dce-mri.," *Magnetic resonance in medicine*, vol. 62, pp. 205–217, July 2009.

[190] R. Karch, "Computersimulation in der medizin. pharmakokinetische modelle," 2003.

[191] G. M. Liumbruno, F. Bennardello, A. Lattanzio, P. Piccoli, G. Rossettias, I. S. of Transfusion Medicine, and I. (SIMTI), "Recommendations for the use of albumin and immunoglobulins.," *Blood transfusion = Trasfusione del sangue*, vol. 7, pp. 216–234, July 2009.

[192] L. Saba, J. Sanches, L. Pedro, and J. Suri, *Multi-Modality Atherosclerosis Imaging and Diagnosis.* Springer, 2014.

[193] P. L. Kei and L. P. Chan, "Gadolinium chelate-associated nephrogenic systemic fibrosis.," *Singapore medical journal*, vol. 49, pp. 181–185, Mar. 2008.

[194] J. Meding, M. Urich, K. Licha, M. Reinhardt, B. Misselwitz, Z. A. Fayad, and H.-J. Weinmann, "Magnetic resonance imaging of atherosclerosis by targeting extracellular matrix deposition with gadofluorine m.," *Contrast media & molecular imaging*, vol. 2, pp. 120–129, 2007.

[195] J. Barkhausen, W. Ebert, C. Heyer, J. F. Debatin, and H. J. Weinmann, "Detection of atherosclerotic plaque with gadofluorine-enhanced magnetic resonance imaging," *Circulation*, vol. 108, no. 5, pp. 605–609, 2003.

[196] M. Sirol, P. R. Moreno, K.-R. Purushothaman, E. Vucic, V. Amirbekian, H.-J. Weinmann, P. Muntner, V. Fuster, and Z. A. Fayad, "Increased neovascularization in advanced lipid-rich atherosclerotic lesions detected by gadofluorine-m-enhanced mri: implications for plaque vulnerability.," *Circulation. Cardiovascular imaging*, vol. 2, pp. 391–396, Sept. 2009.

[197] J. A. Ronald, Y. Chen, A. J.-L. Belisle, A. M. Hamilton, K. A. Rogers, R. A. Hegele, B. Misselwitz, and B. K. Rutt, "Comparison of gadofluorine-m and gd-DTPA for noninvasive staging of atherosclerotic plaque stability using MRI," *Circulation: Cardiovascular Imaging*, vol. 2, pp. 226–234, mar 2009.

[198] J. Xie, J. Wang, G. Niu, J. Huang, K. Chen, X. Li, and X. Chen, "Human serum albumin coated iron oxide nanoparticles for efficient cell labeling.," *Chemical communications (Cambridge, England)*, vol. 46, pp. 433–435, Jan. 2010.

[199] Q. Quan, J. Xie, H. Gao, M. Yang, F. Zhang, G. Liu, X. Lin, A. Wang, H. S. Eden, S. Lee, G. Zhang, and X. Chen, "Hsa coated iron oxide nanoparticles as drug delivery vehicles for cancer therapy.," *Molecular pharmaceutics*, vol. 8, pp. 1669–1676, Oct. 2011.

[200] P. Opriessnig, G. Almer, D. Frascione, R. Prassl, H. Mangge, and R. Stollberger, "Cytokine functionalized uspios: suitable targeting sequences for molecular mr imaging of atherosclerotic vessel walls?," *Proceedings of the ESMRMB 28th Annual Scientific Meeting*, 2011.

[201] P. Opriessnig, G. Almer, D. Frascione, R. Prassl, H. Mangge, and R. Stollberger, "Bsa-uspio enhanced atherosclerotic plaque mri: A surrogate complex to mimic gadofluorine enhanced fibrous plaque detection?," *Proceedings of the ESMRMB 29th Annual Scientific Meeting*, 2012.

[202] P. Opriessnig, G. Almer, C. Vonach, R. Prassl, H. Mangge, and R. Stollberger, "Uspio vs. stealh magnetic liposomes (sml) enhanced atherosclerotic plaque mri.," *Proceedings of the ESMRMB 30th Annual Scientific Meeting*, 2013.

9 Appendix

9.1 Patent Application

This section includes the application text and drawings for the patent application.

Patent attorney's office:
Maiwald Patentanwaltsgesellschaft mgH (Munich, German, www.maiwald.eu)

Patent application title:
Balloon catheter device for use in an aorta of a rabbit or a human being.

Patent application number:
GB 1614500.5 (Intellectual Property Office, Great Britain (www.ipo.gov.uk))

Patent application date:
25th of August, 2016

Combined search and examination report (Intellectual Property Office, GB):
14th of February, 2017; Documents of category A were found (document indicating technological background and/or state of the art).

PCT application number:
PCT/EP2017/071300

Date of receipt:
24th of August, 2017

Receiving Office:
European Patent Office, The Hague

MEDIZINISCHE UNIVERSITÄT GRAZ   München, 25. August 2016

Unser Zeichen: M11111GB / LE.CSC

Medizinische Universität Graz

Technologieverwertung

Auenbruggerplatz 2./4. Stock, 8036 Graz, Österreich

BALLOON CATHETER DEVICE FOR USE IN AN AORTA OF A RABBIT OR A HUMAN BEING

FIELD OF THE INVENTION

The invention relates to a balloon catheter device for use in an aorta of a rabbit or a human being. In particular, the present invention deals with the development of a standardized balloon injury device for the generation of reproducible minimal invasive-lesions in rabbits (pressure controlled balloon injury). At the same time the device should also be adapted for being used safely in balloon thrombectomy.

BACKGROUND OF THE INVENTION

In the field of pre-clinical atherosclerosis (AS) research, New Zealand white (NZW) rabbits are the standard model to investigate plaque development and therapy. Importantly, atherosclerotic vascular lesions of these animals are closer to human pathology then example given lesions of ApoE deficient mice. Typically, abdominal aortic AS is induced by a combination of a balloon catheter denudation and a high-fat diet. As the abdominal aorta is markedly narrowing from proximal to distal (5 to

3 mm in diameter) a constant balloon volume (manual balloon injury) introduces significant pressure differences (1 to 3 bar) when retracted. Consequently, a heterogeneous plaque development is observed.

5   By now, manual balloon injury is performed from the iliac bifurcation to the renal artery (or take arch) or vice versa introducing a balloon catheter through the carotid artery or femoral artery, respectively. Respective methods are described e.g. in the article "detection of new vessels in atherosclerotic plaques of rabbits using dynamic contrast enhanced MRI and 18 F – FDG PET" by Calcagno et al, published in the

10   journal "arteriosclerosis, thrombosis, and vascular biology – Journal of the American Heart Association" on 8 May 2008, or in the article "Reproducibility of black blood dynamic contrast enhanced magnetic resonance imaging in aortic plaques of atherosclerotic rabbits" by Calcagno et al, published in the "Journal of magnetic resonance imaging 32; 191 – 198 (2010)" in 2010.

15

It is known to inflate the balloon manually using a liquid or gas filled syringe. During the passage of the catheter, inflation pressure variations are introduced. Effects of inflation pressure on plaque development are the topic of the article "effects of inflation pressure of balloon catheter on vascular injuries and subsequent

20   development of intimai hyperplasia in rabbit aorta" by Asada et al, published in Atherosclerosis 121 (1996) 45 – 53 in 1996.

Regarding balloon thromboembolectomy in acute arterial occlusion, there is a need for an improved technique which especially helps junior doctors to manage such a

25   surgery in less training time and, more important, improves patient safety and potentially lower catheter induced material injuries. This is very important as the procedure is the most frequently required emergency procedure in vascular surgery, for example with more than 20,000 operations per year in Germany.

SUMMARY OF THE INVENTION

It is an object of the present invention to provide a balloon catheter device for use in an aorta of a rabbit or a human being which enables inducing homogeneous and reproducible injuries in the aorta of the rabbit and to avoid injuries in the aorta of the human being.

The problem is solved by the subject matter according to the independent claims. The dependent claims, the following description and the drawings show preferred embodiments of the invention.

One core of the invention lies in that the balloon catheter device according to the present invention comprises means which are adapted for automatically adapting a volume within a balloon of a balloon catheter to changing diameters of an aorta of a rabbit or a human being into which the balloon has been inserted. By this, an inflation pressure of the balloon and a pressure respectively force which the balloon exerts on the aorta of the rabbit of the human being can be controlled, in particular in such a way that said pressure respectively force is kept stable at a predefined value. Furthermore, the balloon catheter device comprises means which are adapted for pulling out or retracting the balloon out of the aorta of the rabbit or the human being at a constant speed. The balloon catheter device further comprises a control circuit for controlling aforementioned means for adapting the balloon volume and for retracting the balloon out the aorta.

The combination of both effects, namely the stable pressure of the balloon and the constant retracting speed of the balloon out of the aorta, enables inducing homogeneous, standardized and reproducible injuries in the aorta of the rabbit respectively to avoid injuries in the aorta of the human being.

According to an aspect of the invention, a balloon catheter device for use in an aorta of a rabbit or a human being is provided. The balloon catheter device comprises a balloon catheter, a syringe, an actuator, a pressure sensor, a balloon retracting unit, a first control unit and a second control unit.

5

The balloon catheter comprises a flexible tube and a balloon at a distal end of the tube, and the syringe comprises a chamber containing a fluid, wherein the chamber is connected to a proximal end of the tube. The fluid within the chamber of the syringe can be liquid, e.g. NaCl, or gaseous. The whole system, i.e. the chamber of the

10   syringe, the flexible tube and the balloon can be filled with the fluid.

The syringe can further comprise a housing and a rod with a plunger, wherein the plunger is disposed at a distal end of the rod. The chamber can be variable in its volume and can be defined by an inner wall of the housing of the syringe and the

15   plunger. In a known manner, the rod can be slid into the housing of the syringe and pulled out of the housing of the syringe, thereby increasing the volume of the chamber (when being pulled out of the housing) or decreasing the volume of the chamber (when being slid into the housing).

20   The actuator is adapted for injecting the fluid contained in the chamber of the syringe into the flexible tube, thereby increasing a volume of the fluid contained within the balloon, and for sucking in fluid contained in the flexible tube into the chamber of the syringe, thereby decreasing the volume of the fluid contained within the balloon.

25   In particular, the actuator can be a linear actuator which can be adapted for linearly moving the rod of the syringe in a distal direction of the syringe for injecting the fluid contained in the chamber of the syringe into the flexible tube, thereby increasing a volume of the fluid contained within the balloon.

The linear actuator can further be adapted for linearly moving the rod of the syringe in a proximal direction of the syringe for sucking in fluid contained in the flexible tube into the chamber of the syringe, thereby decreasing the volume of the fluid contained within the balloon.

5

The pressure sensor is adapted for sensing an inflation pressure of the balloon. The pressure sensor can e.g. be situated or disposed within the flexible tube, where the pressure sensor can sense the pressure within the flexible tube and determine the pressure within the balloon. Alternatively, the pressure sensor can be disposed

10   between the syringe and the flexible tube and can be in a fluid connection with both the syringe (i.e. its chamber) and the flexible tube.

The balloon retracting unit is adapted for retracting the balloon out of the aorta. For example, the balloon retracting unit can comprise means by which the flexible tube

15   can be pulled in a direction such that the balloon at the end of the flexible tube is pulled out of the aorta.

The first control unit is communicatively connected to the pressure sensor and the actuator, in particular the linear actuator. Such a connection can be made by wires or

20   wireless in a known manner. In particular, the first control unit can receive pressure data generated by the pressure sensor, wherein the pressure data represent measured balloon inflation pressures. Also, the first control unit can send command signals to the actuator, in particular the linear actuator.

25   The second control unit is communicatively connected to the balloon retracting unit. Such a connection can be made by wires or wireless in a known manner. In particular, the second control unit can send command signals to the balloon retracting unit.

The first control unit is adapted to receive pressure data representing the inflation pressure of the balloon measured by the pressure sensor and to control the actuator, in particular the linear actuator, depending on the received pressure data, such that the inflation pressure of the balloon is kept stable at a predefined inflation pressure value. In this context, the term "stable" can in an ideal case mean that the inflation pressure of the balloon is kept constant at a predefined inflation pressure value. In reality, the inflation pressure of the balloon may deviate around the predefined balloon inflation pressure in a certain range.

In particular, the first control unit can receive pressure data from the pressure sensor according to which the pressure within the balloon is rising. This can be due to a decrease in the diameter of the aorta of the rabbit or the human being into which the balloon has been inserted. The first control unit can control the actuator, such that the volume of the chamber of the syringe is increased. In particular, the first control unit can control the linear actuator, such that the linear actuator pulls the rod out of the housing of the syringe, thereby increasing the volume of the chamber. As a result, a vacuum is built within the chamber which forces fluid contained within the flexible tube to move into the chamber. However, the volume of fluid contained within the flexible tube remains constant. As the total volume of fluid contained within the chamber, the flexible tube and the balloon is always constant, fluid contained within the balloon, which is flexible, is forced to move out of the balloon and into the flexible tube. Thereby, the volume of the flexible balloon is decreased. By this, the volume of the balloon is being adapted to a decreased diameter of the aorta in order to stabilize the inflation pressure of the balloon respectively the pressure within the balloon, wherein a pressure respectively force which the balloon exerts on the aorta is also being adapted in a way that it is kept stable at an intended value.

In an opposite case, the first control unit can receive pressure data from the pressure sensor according to which the pressure within the balloon is falling. This can be due to an increase in the diameter of the aorta of the rabbit of the human being into which

the balloon has been inserted. The first control unit can control the actuator, such that the volume of the chamber of the syringe is decreased. In particular, the first control unit can control the linear actuator, such that the linear actuator pushes the rod deeper into the housing of the syringe, thereby decreasing the volume of the chamber. As a result, fluid contained within the chamber is forced to leave the chamber and to flow into the flexible tube. As a consequence, less fluid is contained within the chamber, wherein the volume of fluid contained within the flexible tube is constant. As the total volume of fluid contained within the chamber, the flexible tube and the balloon is constant, the volume of the flexible balloon is increased. By this, the volume of the balloon is being adapted to an increased diameter of the aorta in order to stabilize the inflation pressure of the balloon respectively the pressure within the balloon, wherein a pressure respectively force which the balloon exerts on the aorta is also being adapted in a way that it is kept stable at an intended value.

Furthermore, the second control unit is adapted to control the balloon retracting unit, such that the balloon is retracted out of the aorta at a constant speed. As an overall result, the balloon can be pulled out of the aorta of the rabbit of the human being at a constant speed and at a stable predetermined inflation pressure. By this, the aorta of the rabbit can be damaged in such a way that homogenous plaques can be induced on the one hand, and on the other hand, the aorta of the human being can be saved from damages when pulling out the balloon.

According to an embodiment, the balloon catheter is a balloon catheter for generating reproducible minimal-invasive lesions in the aorta of the rabbit, wherein the predefined inflation pressure value is high enough to cause the balloon to generate intended lesions in the aorta of the rabbit, if the balloon has an inflation pressure as high as the predefined inflation pressure value.

According to another embodiment, the balloon catheter is a balloon catheter for use in pressure controlled balloon thrombectomy on the human being, wherein the

predefined inflation pressure value is not high enough to cause the balloon to generate lesions in the aorta of the human being, if the balloon has an inflation pressure as high as the predefined inflation pressure value.

5   The pressure sensor can be a Luer lock pressure sensor. The Luer lock pressure sensor can be connected to a Luer lock fitting of the syringe on the one side and to the flexible tube on the other side. The Luer lock pressure sensor is comfortable to and can be combined with lots of different types of syringes because the Luer lock fitting is standardized.

10

The balloon catheter device can further comprise an encoder and recording unit and a quadrature encoder, wherein the encoder and recording unit is adapted for receiving, encoding and storing pressure data representing measured pressures from the pressure sensor and step data representing a number of steps performed by the linear

15   actuator from the quadrature encoder.

The encoder and recording unit can be adapted for calculating a volume of the balloon depending on the received pressure data and step data.

20   The balloon catheter device can further comprise a computer unit, wherein the encoder and recording unit is adapted for transmitting the received pressure data and step data to the computer unit, and wherein the computer unit is adapted for storing the transmitted pressure data and step data and for creating real time plots of both the transmitted pressure data and step data.

25

According to another embodiment, the first control unit and the second control unit are integrated into a single control unit. Furthermore, the encoder and recording unit can also be integrated into the single control unit.

According to another embodiment, the balloon retracting unit comprises a rack, a sled, and driving means, wherein the sled is slideably mounted on the rack, and wherein the syringe and the linear actuator are fixedly mounted on the sled. The driving means are adapted for driving the sled such that the sled is sliding along the rack at a sliding speed, and the second control unit can control the driving means, such that the sliding speed of the sled is constant.

The rack can comprise two guiding rods, wherein the driving means can comprise a rotating stepper and a spindle drive. The sled can be guided in a linear direction by means of the two guiding rods, wherein the spindle drive can drive the sled such that the sled is sliding along the two guiding rods at the sliding speed, and wherein the second control unit can control the spindle drive, such that the sliding speed of the sled is constant.

According to another embodiment, the balloon retracting unit comprises a retracting roll assembly, and an electric motor, in particular a DC gear motor. The electric motor is adapted for driving the retraction roll assembly such that the retracting roll assembly is rotating at a rotating speed, wherein the retracting roll assembly is configured for advancing the flexible tube of the balloon catheter such that the flexible tube is retracted out of the aorta when driven by the electric motor, and wherein the second control unit is configured for controlling the electric motor, such that the rotating speed of the retracting roll assembly is constant.

According to another embodiment, the first control unit comprises a memory unit, wherein a predefined upper limit value of the balloon inflation pressure is stored in the memory unit, wherein a predefined lower limit value of the balloon inflation pressure is stored in the memory unit, and wherein a predefined actuating speed of the linear actuator is stored in the memory unit.

The first control unit is adapted for deflating the balloon by driving the linear actuator at the predefined actuating speed, such that the rod of the syringe is moved in a proximal direction of the syringe at a speed proportional to the predefined actuating speed and sucks in fluid contained in the flexible tube into the chamber of

5   the syringe, thereby decreasing the volume of the fluid contained within the balloon, if a value of a measured inflation pressure is higher than the predefined lower limit value of the balloon inflation pressure.

The first control unit is also adapted for inflating the balloon by driving the linear

10   actuator at the predefined actuating speed, such that the rod of the syringe is moved in a distal direction of the syringe at a speed proportional to the predefined actuating speed and injects the fluid contained in the chamber of the syringe into the flexible tube, thereby increasing a volume of the fluid contained within the balloon, if the value of the measured inflation pressure is lower than the predefined upper limit

15   value of the balloon inflation pressure.

Furthermore, the first control unit is adapted for inflating the balloon, if the value of the measured inflation pressure is higher than the predefined lower limit value of the balloon inflation pressure and if the value of the measured inflation pressure is lower

20   than the predefined upper limit value of the balloon inflation pressure.

These and other aspects of the invention will be apparent from and elucidated with reference to the embodiments described hereinafter.

25   BRIEF DESCRIPTION OF THE DRAWINGS

In the following description, exemplary embodiments of the invention are explained with reference to the accompanying schematic drawing in which

Fig. 1   shows a top view of a device in accordance with a first embodiment of
                the invention,

Fig. 2   shows a top view of a device in accordance with a second embodiment
  5   of the invention and

Fig. 3   shows a diagram illustrating a chronological sequence of a balloon
                inflation pressure being controlled by the device according to Fig. 1 or
                2.

10

Fig. 1 shows a balloon catheter device 1 for use in an aorta of a rabbit (not shown) or
a human being (not shown) in accordance with an embodiment of the present
invention. As described in the following, the balloon catheter device 1 can be
adapted for generating reproducible minimal invasive lesions in the aorta of the
15   rabbit or for being used in pressure controlled balloon thrombectomy on the human
being.

The balloon catheter device 1 comprises a balloon catheter 2, a syringe 3, a linear
actuator 4, a pressure sensor 5, a balloon retracting unit 6, a first control unit 7, a
20   second control unit 8 and an encoder and recording unit 9.

The balloon catheter 2 comprises a flexible tube 10 and a balloon 11 at a distal end
12 of the flexible tube 10. The balloon 11 is also flexible, meaning that it can be
inflated by filling it with a fluid and deflated by sucking the fluid out of it. The
25   flexible tube 10 is in a fluid connection with the balloon 11. In particular, a fluid
contained in the flexible tube 10 can be pushed into the balloon 11 and vice versa in
order to inflate or deflate the balloon 11. The flexible tube 10 and the balloon 11 are
adapted to be inserted into the aorta of the rabbit and the human being. The balloon
catheter 2 can be positioned within the aorta, wherein the balloon 11 is in a deflated
30   state. When brought into position in the aorta of the rabbit, the balloon 11 can be

inflated with sufficient pressure and be retracted by retracting the flexible tube 10, thereby causing a minimal-invasive lesion in the aorta of the rabbit, as will be described further below. Furthermore, when brought into position in the aorta of the human being, the balloon 11 can be inflated with sufficient but not too high pressure

5   and be retracted by retracting the flexible tube 10, such that an occlusion respectively a thrombus within the aorta of the human being can be removed without causing an invasive lesion in the aorta of the human being, as will be described further below.

The syringe 3 comprises a housing 13 in which a rod 14 having a plunger 15 can

10   slide in opposite directions, namely in a proximal direction x_p and in a distal direction x_d of the syringe 3, thereby increasing or decreasing a volume of a chamber 16 within the housing 13. The chamber 16 is filled with a fluid and is connected to a Luer cone region 17 of the syringe 3. The flexible tube 10 and the balloon 11 are filled with the same fluid as the chamber 16, also. The fluid within the chamber 16,

15   the flexible tube 10 and the balloon 11 can be liquid, e.g. NaCl, or gaseous. The Luer cone region 17 comprises an injection port 18 which is in a fluid communication with the chamber 16. A proximal end of the flexible tube 10 is fixedly connected to the Luer cone region 17 of the syringe 3, such that the chamber 16 is in a fluid connection with the flexible tube 10 via the injection port 18.

20

The pressure sensor 5 which is a Luer lock pressure sensor is mounted on the syringe 3 in the Luer cone region 17. The pressure sensor 5 is in a fluid connection with the flexible tube 10 on the site shown right in Fig. 1, and the injection port 18 on the site shown left in Fig. 1, such that the pressure sensor 5 senses a pressure within the

25   flexible tube 10 which indicates the pressure in the balloon 11 of the balloon catheter 2. The pressure sensor 5 generates according pressure data which represents the inflation pressure of the balloon 11. The pressure sensor 5 continuously senses the pressure as described above and generates respective a number of pressure data.

The first control unit 7 and the second control unit 8 can be integrated into a single control unit 19 which fulfills all the functions of the first control unit 7 and the second control unit 8. Although not shown in Fig. 1, the encoder and recording unit 9 can also be integrated into the single control unit 19, wherein the single control unit 19 fulfils all the functions of the encoder and recording unit 9. The first control unit 7 can comprise a first memory unit 20, the second control unit 8 can comprise a second memory unit 21 and the encoder and recording unit 9 can comprise a third memory unit 22.

The first control unit 7 can example given be mounted on an Arduino UNO board. The first control unit 7 can comprise a stepper driver 45 (e.g. a DRV8825) to operate the linear actuator 4 respectively its driving unit 37 as described below. Furthermore, the first control unit 7 can comprise an external power supply (not shown) for the stepper driver and an "on/standby" button (not shown). If the "on/standby" button is pressed, the stepper driver 45 of the first control unit 7 controls the driving unit 37 in such a way that the balloon 11 is filled to a predefined balloon inflation pressure, wherein the predefined balloon inflation pressure is hold stable by a threshold technique as described in conjunction with Fig. 3 further below. By pressing a "go-home" button (not shown) of the first control unit 7 the stepper driver 45 of the first control unit 7 controls the driving unit 37 in such a way that stamp 36 of the linear actuator 4 is moved into a starting position, thereby emptying the balloon 11 up to a starting volume. Data representing said starting position can be predetermined and stored in the first memory unit 20. Additionally, the first control unit 7 can comprise an interface (not shown) for a connection with the pressure sensor 5 and an interface (not shown) for a connection with the linear actuator 4.

Retracting of the flexible tube

The balloon retracting unit 6 according to the exemplary embodiment shown by Fig. 1 comprises a rack 23, a sled 24, a holder 25 and driving means 26. The rack 23

comprises two guiding rods 27 and 28. The driving means 26 comprise a rotating stepper 29 and a spindle drive 30.

The holder 25 is a part of and fixedly mounted on the sled 24 on an upper surface thereof. The sled 24 comprises parallel through-holes 31 and 32 (indicated by dashed lines) of such size and length that the two guiding rods 27, 28 can be pushed through the through-holes 31 and 32 and the sled 24 together with the holder 25 can linearly slide along the guiding rods 27, 28 in the proximal direction x_p and in the distal direction x_d. By this, the sled 24 together with its holder 25 is slid ably mounted on the rack 23, wherein the sled 24 is guided in a linear direction, namely in the proximal direction x_p and in the distal direction x_d, by means of the two guiding rods 27, 28.

The sled 24 together with its holder 25 can be driven, in particular can be slid along the two guiding rods 27, 29 of the rack 23 in the proximal direction x_p and in the distal direction x_d as described above by the spindle drive 30 which, in turn, can be driven by the rotating stepper 29 of the driving means 26. In particular, the sled 24 can be driven by the spindle drive 30 at a constant speed. The second control unit 8 is communicatively connected to the rotating stepper 29 of the retracting unit 6. The second control unit 8 is adapted to control the balloon retracting unit 6, such that the balloon 11 of the balloon catheter to is retracted out of the aorta of the rabbit or the human being at a constant speed.

In particular, the second control unit 8 controls the rotating stepper 29 such that it is moved an intended number of steps in an intended turning direction, thereby causing the spindle drive 30 also to rotate an intended number of steps in an intended turning direction. The second control unit 8 controls the rotating stepper 29 such that it is moved the intended number of steps at a constant frequency, thus enabling a constant rotating speed of the spindle drive 30 as well as a constant sliding speed of the sled 24 together with its holder 25. As it will be described further below, the flexible tube

10 is fixed to the holder 25 of the sled 24. Therefore, if the sled 24 is driven by the spindle drive 30 in the proximal direction x_p at a constant speed, the flexible tube 10 is also moved in the proximal direction x_p at a constant speed. By this movement of the flexible tube 10 in the proximal direction x_p, the flexible tube 10 and especially

5   the balloon 11 of the balloon catheter 11 can be retracted out of the aorta of the rabbit or the human being by use of the balloon retracting unit 6, if the flexible tube 10 and the balloon 11 have been inserted into the aorta before.

The spindle drive 30 comprises an external thread (not shown) and is guided through

10   a third through-hole (not shown) within the sled 24. The third through-hole runs parallel to the first through-hole 31 and to the second through-hole 32. The third through-hole comprises an internal thread (not shown) corresponding to the external thread of the spindle drive 30. The third through-hole is of such length and size that the spindle drive 30 can be pushed through the third through-hole. If the spindle

15   drive 30 is rotating as described above, it drives the sled 24 together with its holder 25, such that the sled 24 slides along the rack 23 in the distal direction x_d (if the spindle drive is turning in a first rotating direction) or in the proximal direction x_p (if the spindle drive is turning in a second direction, wherein the second rotating direction is opposite to the first rotating direction).

20

A respective algorithm to control the rotating stepper 29 is stored on the second memory unit 21 of the second control unit 8. For example, the sled can be driven at a constant speed of 5 mm/s. The inventor found out that such a speed is ideal because it enables a relatively fast retraction of the balloon 11 and the flexible tube 10 out of

25   the aorta of the rabbit of the human being on the one hand, and on the other hand such a speed is not too high (which could negatively influence the first control unit 7 in that the first control unit 7 cannot adapt the volume respectively the inflation pressure of the balloon 11 fast enough, which could lead to an explosion of the balloon 11 or in the worst case of the aorta of the rabbit or the human being).

30

Inflating (Filling)/Deflating (Emptying) of the Balloon

The linear actuator 4 is fixed to the holder 25 at a traverse 33 of the holder 25. The housing 13 of the syringe 3 is also fixed to the holder 25. By this, the syringe 3 and the linear actuator 4 are fixed to the sled 24. The housing 13 can e.g. be fixed on a second sled 34 which can be fixed on holder 25 in different positions with regards to the distal direction x_d respectively the proximal direction x_p of the syringe 3.

The linear actuator 4 comprises a cylindrical housing 35, a stamp 36, a driving unit 37 and a quadrature (rotary) encoder 38. The stamp 36 can slide into the cylindrical housing 35 in the proximal direction x_p and out of the cylindrical housing 35 in the distal direction x_d. A distal end of the stamp 36 of the linear actuator 4 is fixed to a proximal end of the rod 14 of the syringe 3. The cylindrical housing 35 of the linear actuator 4 is fixed to the traverse 33 of the holder 25.

If the stamp 36 is moved in the distal direction x_d, the rod 14 of the syringe 3 is also moved in the distal direction x_d, and the volume of the chamber 16 within the housing 13 of the syringe 3 is decreased. As a result, fluid contained in the chamber 16 of the syringe 3 is pushed through the injection port 18 of the syringe 3 into the flexible tube 10 of the balloon catheter 2 where it displaces fluid into the balloon 11 and the balloon 11 of the balloon catheter 2 is inflated. By this, the linear actuator 5 is adapted for linearly moving the rod 14 of the syringe 3 in a distal direction x_d of the syringe 3 for injecting the fluid contained in the chamber 16 of the syringe 3 into the flexible tube 10, thereby increasing a volume of the fluid contained within the balloon 11.

If the stamp 36 is moved in the proximal direction x_p, the rod 14 of the syringe 3 is also moved in the proximal direction x_p, and the volume of the chamber 16 within the housing 13 of the syringe 3 is increased, thereby inducing a vacuum within the chamber 16. As a result, fluid contained in the flexible tube 10 of the balloon catheter

2 is sucked through the injection port 18 of the syringe 3 into the chamber 16 of the housing 13 of the syringe 3 and the flexible balloon 11 of the balloon catheter to is deflated. By this, the linear actuator 5 is adapted for linearly moving the rod 14 of the syringe 3 in a proximal direction x_p of the syringe 3 for sucking in fluid contained in the flexible tube 10 into the chamber 16 of the syringe 3, thereby decreasing the volume of the fluid contained within the balloon 11.

The driving unit 37 in the form of a stepper motor drives the stamp 36 in small steps into the cylindrical housing 35 in the proximal direction x_p and also in small steps out of the cylindrical housing 35 in the distal direction x_d. The stepper driver 45 of the first control unit 7 is communicatively connected to the pressure sensor 5 and the driving unit 37 of the linear actuator 4. A microprocessor P of the first control unit 7 receives the pressure data generated by the pressure sensor 5 and controls the stepper driver 45 which in turn controls the driving unit 37 of the linear actuator 4 depending on the received pressure data. In particular, the stepper driver 45 controls the number of steps by which the driving unit 37 drives the stamp 36 and the direction into which the stamp 36 is moved into the cylindrical housing 35 or out of the cylindrical housing 35.

As the balloon 11 and the flexible tube 10 of the balloon catheter 2 are retracted out of the aorta of the rabbit or the human being by use of the retracting unit 6 as described above, the pressure within the balloon 11 may vary, if a volume of the balloon 11 remains constant and the diameter of the aorta is changing. For example, an abdominal aorta can narrow from proximal to distal from about 5 mm to about 3 mm in diameter. At a constant balloon volume this can introduce significant pressure differences from about 1 bar to 3 bar when retracting the balloon 11 out of the aorta. As the balloon 11 is in contact with the aorta and is exerting a force on the aorta, wherein the force corresponds to the pressure within the balloon 11 respectively the balloon inflation pressure, a change of the inflation pressure of the balloon 11 results in a respective variation of the force exerted on the aorta by the balloon 11. When

being inserted into the aorta of the rabbit, this leads to heterogeneous invasions and plaque development in the art of the rabbit. When being inserted into the aorta of the human being, this can lead to unintended lesions of the aorta of the human being.

5   To solve these problems, the microprocessor P of the first control unit 7 controls the stepper driver 45 which in turn controls the number of steps by which the driving unit 37 drives the stamp 36 and the direction into which the stamp 36 is moved into the cylindrical housing 35 or out of the cylindrical housing 35 in such a way, that the inflation pressure of the balloon 11 is kept stable at a pre-defined inflation pressure

10   value. This is done by adapting the volume of the fluid contained within the balloon 11 to the changing diameter of the aorta. For example, an intended predefined inflation pressure value may be stored in the memory unit 20 of the first control unit 7. This pressure value can be in a range high enough to cause the balloon 11 to generate intended lesions in the aorta of the rabbit, if the balloon 11 has an inflation

15   pressure as high as the predefined inflation pressure value and if the balloon catheter 2 is inserted into the aorta of the rabbit. The intended predefined pressure value alternatively can be in a range not high enough to cause the balloon 11 to generate lesions in the aorta of the human being, if the balloon 11 has an inflation pressure as high as the predefined inflation pressure value and if the balloon catheter 2 is

20   inserted into the aorta of the human being.

The first control unit 7 may receive first pressure data representing a first inflation pressure of the balloon 11 and second pressure data representing a second inflation pressure of the balloon 11 from the pressure sensor 5. The second inflation pressure

25   of the balloon 11 may be higher than the first inflation pressure of the balloon 11. This pressure difference may be due to a decrease in the diameter of the aorta of the rabbit or the human being. The microprocessor P of the first control unit 7 controls the stepper driver 45 and is adapted for determining and controlling a direction as well as a number of steps by which the linear actuator 4 has to move the rod 14 of the

30   syringe 3 in order to decrease the volume within the balloon 11, such that the second

inflation pressure is decreasing towards the first inflation pressure. In this case, the microprocessor P of the first control unit 7 controls the stepper driver 45 and will determine and control the driving unit 37 in such a way that the stamp 36 of the linear actuator 4 is moved into the proximal direction, thereby forcing the rod 14 also to move in the proximal direction x_d. By this, the volume of the fluid contained within the balloon 11 can be decreased as well as the pressure of the balloon 11 as described above.

The second inflation pressure of the balloon 11 also may be lower than the first inflation pressure of the balloon 11. This pressure difference may be due to an increase in the diameter of the aorta of the rabbit or the human being. The microprocessor P of the first control unit 7 controls the stepper driver 45 and is adapted for determining and controlling a direction as well as a number of steps by which the linear actuator 4 has to move the rod 14 of the syringe 3 in order to increase the volume within the balloon 11, such that the second inflation pressure is increasing towards the first inflation pressure. In this case, the microprocessor P of the first control unit 7 controls the stepper driver 45 and will determine and control the driving unit 37 in such a way that the stamp 36 of the linear actuator 4 is moved into the distal direction x_d, thereby forcing the rod 14 also to move in the distal direction x_d. By this, the volume of the fluid contained within the balloon 11 can be increased as well as the pressure of the balloon 11 as described above.

A respective algorithm for controlling the driving unit 37 may be stored in the memory unit 20 of the first control unit 7. For example, the algorithm can be uploaded on and stored in the Arduino UNO board on which the first control unit 7 is mounted.

Storing (Recording)/Plotting of Pressure Data and Step Data

The quadrature (rotary) encoder 38 is communicatively connected to the driving unit 37 of the linear actuator 4. In particular, the encoder 38 is adapted for receiving data from the driving unit 37 with regards to the number of steps the driving unit 37 has moved the stamp 36 and an according direction into which the stamp 36 has been moved by the driving unit 37. The encoder 38 is also communicatively connected to the encoder and recording unit 9. In particular, the encoder 38 can transmit data which it has received from the driving unit 37 to the encoder and recording unit 9 as described above. The encoder and recording unit 9 can encode and store the data received from the encoder 37 in the memory unit 22 of the encoder and recording unit 9. Additionally, the encoder and recording unit 9 can also be communicatively connected to the pressure sensor 5 (not shown). In particular, the encoder and recording unit 9 can receive and encode pressure data which have been generated by the pressure sensor 5 (e.g. the same pressure data which the pressure sensor 5 is transmitted to the first control unit 7).

If the encoder and recording unit 9 has received data from the encoder 38, wherein the data represents a number of steps and a respective direction into which the stamp 36 has been moved by the driving unit 37, the encoder and recording unit 9 can calculate a volume of the balloon 11 or a change of volume of the balloon 11. In other words, the number of steps and the direction can be calculated into a volume of the balloon 11 respectively a change of volume of the balloon 11. For example, the driving unit 37 can drive the stamp 36 with 0.0121 mm/step. An inner diameter of the chamber 13 of the syringe 3 can be for example 4.7 mm. If the driving unit 37 drives the stamp 36 for example 800 steps, the encoder and recording unit 9 can calculate the volume of the balloon 11 of the balloon catheter 2 as follows: 0.0121 mm/step * 800 steps * $(4.7 \text{ mm})^2$ pi/4 = 168 µL. The flexible tube 10 can have for example a maximum capacity for fluid of 750 µL.

The encoder and recording unit 9 can also be communicatively connected to a computer unit 39 which comprises a fourth storing unit 40. In particular, the encoder and recording unit 9 can transmit the step data received by the encoder 38 and the pressure data received by the pressure sensor 5 to the computer unit 39. Similar to the encoder and recording unit 9 the computer unit 39 can store the pressure step data and pressure data in the fourth memory unit 40. Especially, the computer unit 39 can create real time plots of the step data and the pressure data stored in the fourth memory unit 40. Aforementioned functions of the computer unit 39 can also be fulfilled by the single control unit 19 into which the computer unit 39 can be integrated, too.

Fig. 2 shows a balloon computer device 1 according to another embodiment of the present invention. The device 1 is similar to that shown by Fig. 1. The difference mainly lies in the configuration of the balloon retracting unit 6. In the following, only differences between the devices 1 as per Fig. 1 and Fig. 2 are described in order to avoid repetitions.

The balloon retracting unit 6 as per Fig. 2 comprises a retracting roll assembly 41 and an electric DC gear motor 42. The retracting roll assembly 41 comprises a first roller wheel 43 and a second roller wheel 44 and advances the flexible tube 10 of the balloon catheter 2 such that the flexible tube 10 is retracted out of the aorta when driven by the motor 42. In detail, the flexible tube 10 is guided and quenched smoothly in-between the roller wheels 43 and 44, such that a rotational movement of the roller wheels 43 and 44 – by friction between the wheels 43 and 44 and the flexible tube 10 – leads to a movement of the flexible tube 10 in the distal direction x_d or in the proximal direction x_p, depending on the turning direction of the roller wheels 43 and 44. For example, if the second roller wheel 44 is turning in a clockwise direction with regards to the view as per Fig. 2, the flexible tube 10 is moved by the roller wheels 43 and 44 in the distal direction x_d. If, on the other hand, the second roller wheel 44 is turning in an anti-clockwise direction with regards to

the view as per Fig. 2, the flexible tube 10 is moved by the roller wheels 43 and 44 in the proximal direction x_p. By this, the retracting roll assembly 41 can advance the flexible tube 10 of the balloon catheter 2.

5　The DC gear motor 42 is coupled to the second roller wheel 44, such that the motor 42 can drive the second roller wheel 44 into opposite turning directions (clockwise and anticlockwise according to the view as per Fig. 2) at a rotating speed. As the flexible tube 10 is moved in the proximal direction x_p or in the distal direction x_d, the first roller wheel 43, which is in frictional contact with the flexible tube 10 is rotating

10　in a turning direction, which is opposite to the turning direction of the second roller wheel 44. The DC gear motor 42 is communicatively connected to the second control unit 8. In particular, the second control unit 8 controls the motor 42, such that the motor 42 drives the second roller wheel 44 at a constant speed. As a result, the rotating speed of the retracting roll assembly is constant. By this, the flexible tube 10

15　especially can be advanced in the proximal direction x_p such that the balloon 11 and the flexible tube 10 of the catheter 2 are retracted out of the aorta of the rabbit or the human being at a constant speed.

Threshold Technique

20

Fig. 1 and Fig. 2 each show a device 1 comprising a first control unit 7 being capable to hold a stable predefined balloon inflation pressure over the whole retraction distance of the balloon catheter 2 out of the aorta of the rabbit or the human being. The balloon inflation pressure is measured by the pressure sensor 5. The linear

25　actuator 4 is coupled to the syringe 3 and adjusts the volume of the balloon 11 (filling/emptying) depending on the actual balloon inflation pressure. The chamber 16, the flexible tube 10 and the balloon 11 are filled with the fluid, for example NaCl. The predefined balloon inflation pressure may be hold stable by a threshold technique, which is described in the following.

30

Fig. 3 shows a first diagram in the upper part of Fig. 3 and a second diagram in the lower part of Fig. 3. The first diagram comprises a horizontal axis (time in seconds) and a vertical axis (balloon inflation pressure in bar measured by the pressure sensor 5 and transmitted to the first control unit 7). The pressure sensor 5 continuously

5 determines the pressure within the balloon 11 (balloon inflation pressure p), generates respective pressure data, and transmits the pressure data to the first control unit 7 as described above in conjunction with Fig. 1 and 2. The chronological sequence of the balloon inflation pressure p is shown by the first diagram.The second diagram comprises a horizontal axis (time in seconds) and a vertical axis with 2

10 different values (value "1 " representing a "state 1" in which the balloon 11 is inflated as described above in conjunction with Fig. 1 and 2 by filling the balloon 11 with the fluid contained within the chamber 16 of the syringe and the flexible tube 10; value"0" representing a "state 0" in which the balloon 11 is deflated as described above in conjunction with Fig. 1 and 2 by sucking out fluid contained within the

15 balloon 11 into the flexible tube 10 and into the chamber 16 of the syringe 3). The chronological sequence of state 1 and state 0 is shown by the second diagram.

The horizontal axis of the first diagram and the second diagram run parallel to each other, wherein a certain time on the horizontal axis of the first diagram corresponds

20 to the same time on the horizontal axis of the second diagram, meaning that for example a value of 2 seconds on the horizontal axis of the first diagram is situated vertical above a value of 2 seconds on the horizontal axis of the second diagram.

In the memory unit 20 of the first control unit 7 especially three values are stored: a

25 predefined upper limit value of the balloon inflation pressure p_u (e.g. 1.2 bar), a predefined lower limit value of the balloon inflation pressure P_l (e.g. 1.0 bar) and a predefined actuating speed v [steps of the driving unit 37/per second] (e.g. 150 steps/sec) of the linear actuator 4.

The main principle of the threshold technique as depicted by Fig. 3 is that the microprocessor P of the first control unit 7 controls the stepper driver 45 and therefore the microprocessor P compares the pressure data which are generated by the pressure sensor 5 with the upper limit value of the balloon inflation pressure p_u

5   and with the lower limit value of the balloon inflation pressure p_l. Based on the result of such comparisons the stepper driver 45 controls the driving unit 37 of the linear actuator 4 in such a way that the balloon 11 is either inflated or deflated as described above in conjunction with Fig. 1 and 2.

10   In a first comparison, the pressure data are compared with the lower limit value of the balloon inflation pressure p_l. It is checked, whether a balloon inflation pressure value generated by the pressure sensor 5 exceeds the lower limit value of the balloon inflation pressure p_l (requirement 1). If requirement 1 is fulfilled, the stepper driver 45 controls the driving unit 37 of the linear actuator 4 in such a way that the balloon

15   11 is deflated as described above in conjunction with Fig. 1 and 2. This could be implemented in a computer program e.g. as follows: "If p (e.g. 1.1 bar) > p_l (e.g.=1.0 bar), then "state 0".

     In a second comparison, the pressure data are compared with the upper limit value of

20   the balloon inflation pressure p_u. It is checked, whether the balloon inflation pressure value received by the pressure sensor 5 is below the upper limit value of the balloon inflation pressure p_u (requirement 2). If requirement 2 is fulfilled, the stepper driver 45 controls the driving unit 37 of the linear actuator 4 in such a way that the balloon 11 is inflated as described above in conjunction with Fig. 1 and 2. This could be

25   implemented in a computer program e.g. as follows: "If p (e.g. 1.1 bar) < p_u (e.g.=1.2 bar), then "state 1".

     If requirement 1 is fulfilled but not requirement 2, the stepper driver 45 controls the driving unit 37 of the linear actuator 4 in such a way that the balloon 11 is deflated

30   (state 0). If requirement 2 is fulfilled but not requirement 1, the stepper driver 45

controls the driving unit 37 of the linear actuator 4 in such a way that the balloon 11 is inflated (state 1). If both requirements 1 and 2 are fulfilled, the stepper driver 45 controls the driving unit 37 of the linear actuator 4 in such a way that the balloon 11 is inflated (state 1).

5

Referring now to Fig 3, at the beginning (i.e. starting from 0 s) the balloon inflation pressure p is rising but still below the lower limit value of the balloon inflation pressure p_l. Requirement 1 is not fulfilled but requirement 2. Therefore, the stepper driver 45 controls the driving unit 37 of the linear actuator 4 in such a way that the balloon 11 is inflated (state 1).

10

In its further course, at a first point in time t_1 the graph of the balloon inflation pressure p crosses a first auxiliary horizontal dashed line representing the lower limit value of the balloon inflation pressure p_l. At this point of time t_1 , the balloon inflation pressure p equals the lower limit value of the balloon inflation pressure p_l. Requirement 1 is not fulfilled but requirement 2. Therefore, the stepper driver 45 controls the driving unit 37 of the linear actuator 4 in such a way that the balloon 11 is inflated (state 1). In its further course, up to but not including a second point in time t_2 the balloon inflation pressure exceeds the lower limit value of the balloon inflation pressure p_l but still is below the upper limit value of the balloon inflation pressure p_u. Therefore, both requirements 1 and 2 are fulfilled and the balloon 11 is inflated.

15

20

However, at the second point in time t_2, the graph of the balloon inflation pressure p crosses a second auxiliary horizontal dashed line representing the upper limit value of the balloon inflation pressure p_u. At this point of time t_2 , the balloon inflation pressure p equals the upper limit value of the balloon and inflation pressure p_u. Requirement 1 is fulfilled but not requirement 2. Therefore, the stepper driver 45 controls the driving unit 37 of the linear actuator 4 in such a way that the balloon 11 is deflated (state 0).

25

30

In its further course, the graph of the balloon inflation pressure p is still rising up to a third point in time t_3, although the balloon is already being deflated (state 0). This is due to the fact that a change from inflation to deflation influences the inflation pressure of the balloon 11 with some delay because of a delay duration in the system (it takes some time until a movement of the rod 14 of the syringe 3 in the proximal direction x_p leads to a decrease in pressure within the balloon 11) respectively due to a loop time, i.e. a time period until the conditions are queried again.

At the third point of time t_3 the delay duration is over and the balloon inflation pressure p starts to decrease. At a fourth point of time t_4 the balloon inflation pressure p equals the upper limit value of the balloon inflation pressure p_u again. Therefore, at the fourth point of time t_4 the same conditions apply as at the second point of time t_2 (state 0).

As the balloon pressure value further decreases, both conditions 1 and 2 are fulfilled in-between the fourth point of time t_4 and a fifth point of time t_5. Therefore, the balloon 11 is inflated again (state 1). In-between the fourth point of time t_4 and a fifth point of time t_5 the graph of the balloon inflation pressure p is still declining up to the fifth point of time t_5, although the balloon is already being inflated again (state 1). This is due to the fact that a change from deflation to inflation influences the inflation pressure of the balloon 11 with some delay because of a delay duration in the system (it takes some time until a movement of the rod 14 of the syringe 3 in the distal direction x_d leads to an increase in pressure within the balloon 11) respectively due to a loop time, i.e. a time period until the conditions are queried again. At the fifth point of time t_5 the delay duration is over and the balloon inflation pressure p starts to increase again. At a sixth point of time t_6 the balloon inflation pressure p equals the upper limit value of the balloon inflation pressure p_u again. Therefore, at the sixth point of time t_6 the same conditions apply as at the fourth point of time t_4 and at the second point of time t_2 (state 0).

In its further course, the graph of the balloon inflation pressure p describes a zigzag course around the upper limit value of the balloon inflation pressure p_u. A maximum deviation of the balloon inflation pressure p to the upper limit value of the balloon inflation pressure p_u in said zigzag course is a threshold value. The zigzag course is generated by the controlling of the driving unit 37 by the stepper driver 45 of the first control unit using the threshold technique as described above.

Claims

1. A balloon catheter device (1) for use in an aorta of a rabbit or a human being, comprising:

     a balloon catheter (2),

     a syringe (3),

     an actuator (4),

     a pressure sensor (5),

     a balloon retracting unit (6),

     a first control unit (7) and

     a second control unit (8),

     wherein the balloon catheter (2) comprises a flexible tube (10) and a balloon (11) at a distal end (12) of the tube (10),

     wherein the syringe (3) comprises a chamber (16) containing a fluid, wherein the chamber (16) is connected to a proximal end of the tube (10),

     wherein the actuator (4) is adapted

     for injecting the fluid contained in the chamber (16) of the syringe (3) into the flexible tube (10), thereby increasing a volume of the fluid contained within the balloon (11), and

     for sucking in fluid contained in the flexible tube (10) into the chamber (16) of the syringe (3), thereby decreasing the volume of the fluid contained within the balloon (11),

     wherein the pressure sensor (5) is adapted for sensing an inflation pressure of the balloon (11),

     wherein the balloon retracting unit (6) is adapted for retracting the balloon (11) out of the aorta,

     wherein the first control unit (7) is communicatively connected to the pressure sensor (5) and the actuator,

     wherein the second control unit (8) is communicatively connected to the balloon retracting unit (6),

wherein the first control unit (7) is adapted to receive pressure data representing the inflation pressure of the balloon (11) measured by the pressure sensor (5) and to control the actuator (4) depending on the received pressure data, such that the inflation pressure of the balloon (11) is kept stable at a predefined inflation pressure value, and

wherein the second control unit (8) is adapted to control the balloon retracting unit (6), such that the balloon (11) is retracted out of the aorta at a constant speed.

2. The balloon catheter device (1) according to claim 1,

wherein the balloon catheter (2) is a balloon catheter for generating reproducible minimal-invasive lesions in the aorta of the rabbit, and

wherein the predefined inflation pressure value is high enough to cause the balloon (11) to generate intended lesions in the aorta of the rabbit, if the balloon (11) has an inflation pressure as high as the predefined inflation pressure value.

3. The balloon catheter device (1) according to claim 1 or 2,

wherein the balloon catheter (2) is a balloon catheter for use in pressure controlled balloon thrombectomy on the human being, and

wherein the predefined inflation pressure value is not high enough to cause the balloon (11) to generate lesions in the aorta of the human being, if the balloon (11) has an inflation pressure as high as the predefined inflation pressure value.

4. The balloon catheter device (1) according to one of the preceding claims, wherein the pressure sensor (5) is a Luer lock pressure sensor.

5. The balloon catheter device (1) according to one of the preceding claims, further comprising:

an encoder and recording unit (9) and

a quadrature encoder (38),

wherein the encoder and recording unit (9) is adapted for receiving, encoding and storing pressure data representing measured pressures from the pressure sensor (5) and step data representing a number of steps performed by the linear actuator (4) from the quadrature encoder (38).

6. The balloon catheter device (1) according to claim 5,

wherein the encoder and recording unit (9) is adapted for calculating a volume of the balloon (11) depending on the received pressure data and step data.

7. The balloon catheter device (1) according to claim 5, further comprising a computer unit (39),

wherein the encoder and recording unit (9) is adapted for transmitting the received pressure data and step data to the computer unit (39),

wherein the computer unit (39) is adapted for storing the transmitted pressure data and step data and for creating real time plots of both the transmitted pressure data and step data.

8. The balloon catheter device (1) according to one of the preceding claims, wherein the first control unit (7) and the second control unit (8) are integrated into a single control unit (19).

9. The balloon catheter device (1) according to claim 8, wherein the encoder and recording unit (9) is integrated into the single control unit (19).

10. The balloon catheter device (1) according to one of the preceding claims,

wherein the balloon retracting unit (6) comprises

a rack (23),

a sled (24), and

driving means (26),

wherein the sled (24) is slideably mounted on the rack (23),

wherein the syringe (3) and the linear actuator (4) are fixedly mounted on the sled (24),

wherein the driving means (26) are adapted for driving the sled (24) such that the sled (20) is sliding along the rack (23) at a sliding speed, and

5   wherein the second control unit (8) can control the driving means (26), such that the sliding speed of the sled (24) is constant.

11. The balloon catheter device (1) according to claim 10,

wherein the rack (23) comprises two guiding rods (27, 28),

10   wherein the driving means (26) comprise a rotating stepper (29) and a spindle drive (30),

wherein the sled (24) is guided in a linear direction (x_P, x_d) by means of the two guiding rods (27, 28),

wherein the spindle drive (30) can drive the sled (24) such that the sled (24) is

15   sliding along the two guiding rods (27, 28) at the sliding speed, and

wherein the second control unit (8) can control the spindle drive (30), such that the sliding speed of the sled (24) is constant.

12. The balloon catheter device (1) according to one of the preceding claims,

20   wherein the balloon retracting unit (6) comprises

a retracting roll assembly (41) and

an electric motor (42), in particular a DC gear motor,

wherein the electric motor (42) is adapted for driving the retraction roll assembly (41) such that the retracting roll assembly (41) is rotating at a rotating

25   speed,

wherein the retracting roll assembly (41) is configured for advancing the flexible tube (10) of the balloon catheter (2) such that the flexible tube (10) is retracted out of the aorta when driven by the electric motor (42), and

wherein the second control unit (8) is configured for controlling the electric motor (42), such that the rotating speed of the retracting roll assembly (41) is constant.

13. The balloon catheter device (1) according to one of the preceding claims, wherein the first control unit (7) comprises a memory unit (20),

wherein a predefined upper limit value of the balloon inflation pressure is stored in the memory unit (20),

wherein a predefined lower limit value of the balloon inflation pressure is stored in the memory unit (20),

wherein a predefined actuating speed of the linear actuator (4) is stored in the memory unit (20),

wherein the first control unit (7) is adapted for deflating the balloon (11) by driving the linear actuator (4) at the predefined actuating speed, such that the rod (14) of the syringe (13) is moved in a proximal direction (x_P) of the syringe (3) at a speed proportional to the predefined actuating speed and sucks in fluid contained in the flexible tube (10) into the chamber (16) of the syringe (3), thereby decreasing the volume of the fluid contained within the balloon (11), if a value of a measured inflation pressure is higher than the predefined lower limit value of the balloon inflation pressure, and

for inflating the balloon (11) by driving the linear actuator (4) at the predefined actuating speed, such that the rod (14) of the syringe (3) is moved in a distal direction (x_d) of the syringe (3) at a speed proportional to the predefined actuating speed and injects the fluid contained in the chamber (16) of the syringe (3) into the flexible tube (10), thereby increasing a volume of the fluid contained within the balloon (11), if the value of the measured inflation pressure is lower than the predefined upper limit value of the balloon inflation pressure,

wherein the first control unit (7) is adapted for inflating the balloon (11),

if the value of the measured inflation pressure is higher than the predefined lower limit value of the balloon inflation pressure and

if the value of the measured inflation pressure is lower than the predefined upper limit value of the balloon inflation pressure.

ABSRACT

The invention relates to a balloon catheter device (1) for use in an aorta of a rabbit or a human being. The device (1) comprises a balloon catheter (2), a syringe (3), an
5   actuator (4), a pressure sensor (5), a balloon retracting unit (6), a first control unit (7) and a second control unit (8). The balloon catheter (2) comprises a flexible tube (10) and a balloon (11) at a distal end (12) of the tube (10) and the syringe (3) comprises a chamber (16) containing a fluid, wherein the chamber (16) is connected to a proximal end of the tube (10). The actuator (4) is adapted for increasing/decreasing a
10   volume of the fluid contained within the balloon (11). The pressure sensor (5) is adapted for sensing an inflation pressure of the balloon (11) and the balloon retracting unit (6) is adapted for retracting the balloon (11) out of the aorta. The first control unit (7) is adapted to receive pressure data representing the inflation pressure of the balloon (11) measured by the pressure sensor (5) and to control the actuator (4)
15   depending on the received pressure data, such that the inflation pressure of the balloon (11) is kept stable at a predefined inflation pressure value, and the second control unit (8) is adapted to control the balloon retracting unit (6), such that the balloon (11) is retracted out of the aorta at a constant speed.
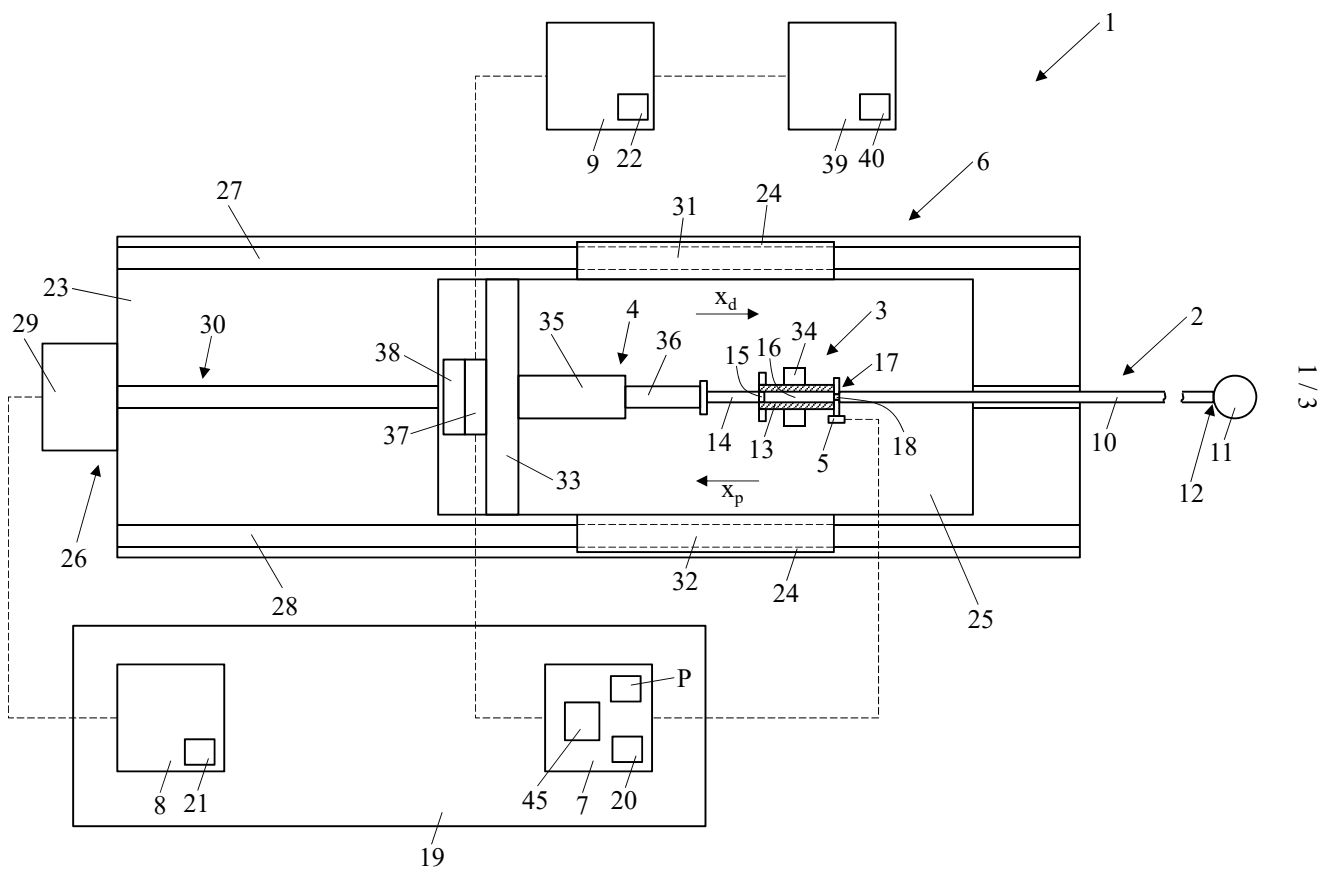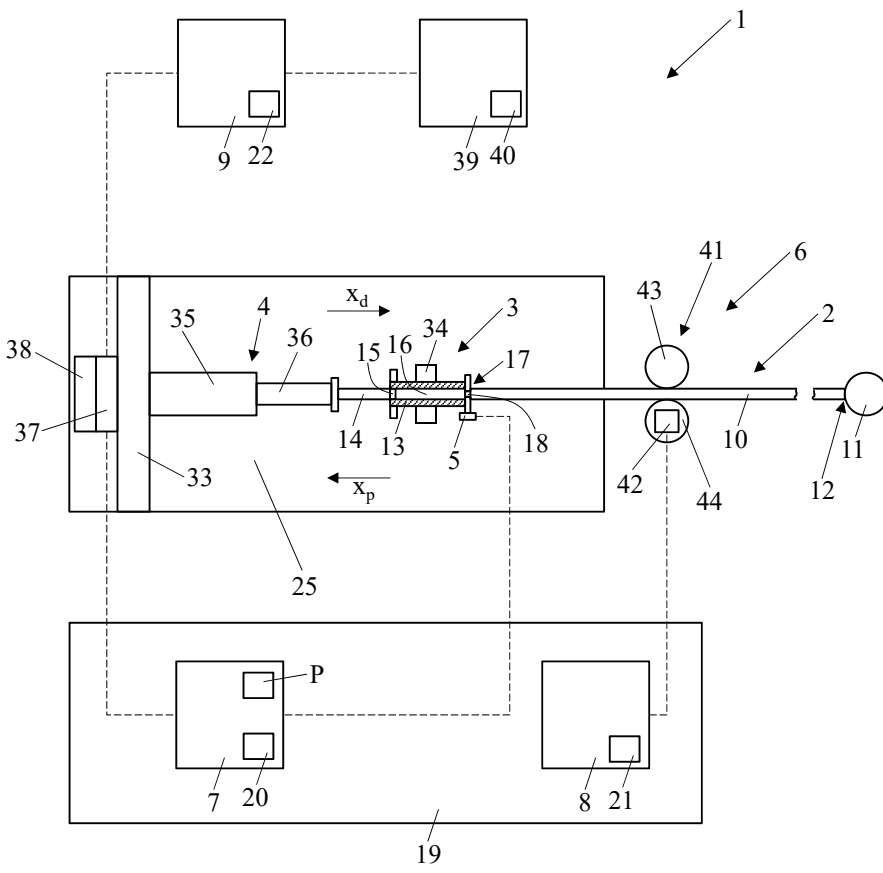
20   Fig. 1

Fig. 1

Fig. 2

2 / 3

Fig. 3